

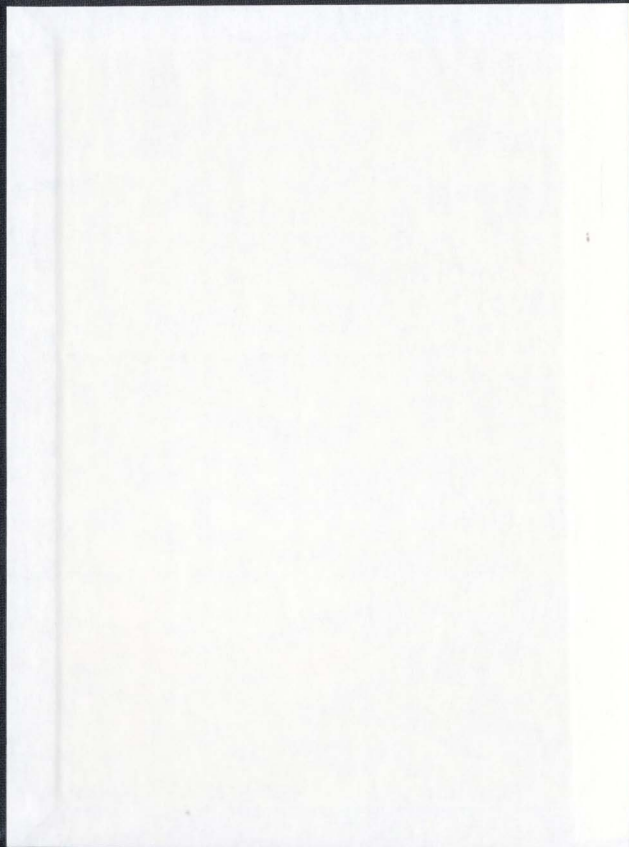
ENHANCED RATES OF ELECTRON TRANSPORT IN
CONJUGATED-REDOX POLYMER HYBRIDS

CENTRE FOR NEWFOUNDLAND STUDIES

TOTAL OF 10 PAGES ONLY
MAY BE XEROXED

(Without Author's Permission)

COLIN CAMERON



INFORMATION TO USERS

This manuscript has been reproduced from the microfilm master. UMI films the text directly from the original or copy submitted. Thus, some thesis and dissertation copies are in typewriter face, while others may be from any type of computer printer.

The quality of this reproduction is dependent upon the quality of the copy submitted. Broken or indistinct print, colored or poor quality illustrations and photographs, print bleedthrough, substandard margins, and improper alignment can adversely affect reproduction.

In the unlikely event that the author did not send UMI a complete manuscript and there are missing pages, these will be noted. Also, if unauthorized copyright material had to be removed, a note will indicate the deletion.

Oversize materials (e.g., maps, drawings, charts) are reproduced by sectioning the original, beginning at the upper left-hand corner and continuing from left to right in equal sections with small overlaps.

Photographs included in the original manuscript have been reproduced xerographically in this copy. Higher quality 6" x 9" black and white photographic prints are available for any photographs or illustrations appearing in this copy for an additional charge. Contact UMI directly to order.

Bell & Howell Information and Learning
300 North Zeeb Road, Ann Arbor, MI 48106-1346 USA
800-521-0600

UMI[®]



National Library
of Canada

Acquisitions and
Bibliographic Services

395 Wellington Street
Ottawa ON K1A 0N4
Canada

Bibliothèque nationale
du Canada

Acquisitions et
services bibliographiques

395, rue Wellington
Ottawa ON K1A 0N4
Canada

Your file Votre référence

Our file Notre référence

The author has granted a non-exclusive licence allowing the National Library of Canada to reproduce, loan, distribute or sell copies of this thesis in microform, paper or electronic formats.

The author retains ownership of the copyright in this thesis. Neither the thesis nor substantial extracts from it may be printed or otherwise reproduced without the author's permission.

L'auteur a accordé une licence non exclusive permettant à la Bibliothèque nationale du Canada de reproduire, prêter, distribuer ou vendre des copies de cette thèse sous la forme de microfiche/film, de reproduction sur papier ou sur format électronique.

L'auteur conserve la propriété du droit d'auteur qui protège cette thèse. Ni la thèse ni des extraits substantiels de celle-ci ne doivent être imprimés ou autrement reproduits sans son autorisation.

0-612-54830-9

Canada

Enhanced Rates of Electron Transport in Conjugated-Redox Polymer Hybrids

by

Colin Cameron

B.Sc.(Honours), University of Ottawa
Ottawa, Ontario, Canada 1992

A thesis submitted to the School of Graduate
Studies in partial fulfillment of the
requirements for the degree of
Doctor of Philosophy

Department of Chemistry
Memorial University of Newfoundland
St. John's, Newfoundland, Canada
April, 2000

Abstract

A series of benzimidazole-based conjugated polymers have been synthesized and their Ru^{2+} and Os^{2+} complexes reported. These novel compounds feature coordination of redox-active metal centres into the quasi-infinite π network of a conjugated polymer to give “conjugated-redox polymer hybrids”. These advanced materials offer technologically useful applications in, for example, electrochromic devices, molecular electronics, and electrocatalysis.

The focus of this work has been to examine whether the interaction of metal sites through the polymer backbone can lead to enhancement of electron transport rates, measured as D_e , the electron diffusion coefficient. This parameter was measured by three different methods: rotating disc current mediation, dual electrode voltammetry, and impedance spectroscopy. Good agreement between the three was found, with impedance being the most reliable and versatile approach.

Conservative estimates of D_e range up to 1×10^{-6} and $2 \times 10^{-8} \text{ cm}^2 \text{ s}^{-1}$ respectively for polymers containing ruthenium and osmium. This represents a tenfold to a one-hundredfold increase in the rate of electron transport over conventional redox polymers. Furthermore it was shown that D_e can be manipulated by controlling the protonation of the polymer, and that backbone degradation also has an influence.

The special arrangement of the hybrid polymers permits strong electronic communication between metal sites. This in turn leads to the higher rates of electron transport. Intervalence transfer bands in the near infrared spectrum confirmed that

the electronic coupling of neighbouring metal sites through the polymer is comparable to that in similar dinuclear model compounds. This coupling is so strong in the pyrazine polymers that it leads to splitting of the redox electrochemistry into a pair of distinct waves, with vanishing conductivity in the 50% oxidized state. This unusual condition provides some insight into the orbital energy relationships in these systems.

The experimental evidence indicates that charge propagation and the corresponding enhancement of D_e in the hybrid polymers occurs via two exclusive superexchange mechanisms, extending the model previously invoked in simpler dinuclear systems.

Acknowledgments

I would like to express gratitude to Dr. G. B. Bodwell and Dr. C. R. Lucas for their input as part of my supervisory committee, and to the Chemistry Department and the School of Graduate Studies for financial support. The efforts of the technical and support staff are also acknowledged, as are those of Mr. D. Miller for N.M.R., and Dr. B. Gregory and Ms. M. Baggs for mass spectroscopy services.

I am grateful to my colleagues in the Pickup research group for their assistance on countless occasions, and to my friends and family for their ongoing support.

Finally I would like to extend my deepest gratitude to my supervisor Dr. Peter G. Pickup.

Contents

Title	i
Abstract	ii
Acknowledgments	iv
Table of Contents	v
List of Figures	ix
List of Schemes	xiv
List of Tables	xv
Glossary of Abbreviations	xvii
Glossary of Symbols	xix
1 Introduction	1
1.1 Conjugated Polymers: General Properties	2
1.2 Conjugated Polymers: Electronic Conductors	5
1.3 Redox Polymers	9
1.4 Conjugated Redox Polymers: Hybrid Materials	13
1.4.1 Conjugated Metallopolymers in the Literature	16

1.5	Objectives	35
2	Experimental	37
2.1	General Procedures and Instrumentation	38
2.2	Starting Materials and Miscellaneous	39
2.3	Electropolymerizable Monomers	42
2.3.1	Thiophene-based Monomers	42
2.3.2	Pyrrole-based Monomers	44
2.4	Non-electropolymerizable Models	45
2.4.1	Pyridine Type Benzimidazoles	45
2.4.2	Phenol-based Benzimidazoles	49
2.4.3	Benzothiazoles	49
2.4.4	Other	51
2.5	Model Complexes	51
2.5.1	Ruthenium Complexes	52
2.5.2	Osmium Complexes	55
2.6	Polymers	55
2.7	Polymer Complexes	60
2.7.1	Ruthenium Complexes	60
2.7.2	Osmium Complexes	62
3	Synthesis and Characterization of Uncomplexed Polymers	64
3.1	Thiophene-based Polymers	65
3.1.1	Attempted Synthesis	65
3.2	Condensation Polymers	68
3.2.1	Synthesis	68
3.2.2	Elemental Analysis	69

3.2.3	IR Spectroscopy	69
3.2.4	NMR Spectroscopy	73
3.2.5	UV-Vis Spectroscopy	76
3.3	Local Defects: Incomplete Ring Closure	79
3.3.1	<i>Ab initio</i> Modeling of the Structural Defect	81
3.4	Electrochemistry	85
3.4.1	Film Preparation	85
3.4.2	Cyclic Voltammetry	87
4	Coordination Compounds and Electrochemistry	96
4.1	Model Compound Electrochemistry	97
4.2	Polymer Complexes	99
4.2.1	Molecular Mass	100
4.2.2	Film Preparation and Solubility Concerns	100
4.2.3	Optical Properties	101
4.2.4	Cyclic Voltammetry	106
4.3	Pyrroles	117
5	Electron Transport in Polymer Complexes	118
5.1	Polymer Thickness	119
5.2	Rotating Disc Voltammetry (RDV)	121
5.2.1	Background	121
5.2.2	Experimental Details	124
5.2.3	Leak Current	124
5.2.4	Backbone Degradation	128
5.2.5	Results	132
5.3	Dual Electrode Voltammetry	135

5.3.1	Background	135
5.3.2	Experimental Details	137
5.3.3	Results	138
5.4	Impedance Methods	147
5.4.1	Background	147
5.4.2	Experimental Details	150
5.4.3	Results	150
5.5	D_e Conclusions	157
6	Intervallence Transfer Bands	162
6.1	Introduction	163
6.2	Experimental	167
6.3	Results	170
7	Conclusions	175
	References	178
A	Spectra	186
A.1	^1H NMR Spectra	187
A.1.1	Models and Monomers	187
A.1.2	Polymers	199
A.2	Infrared Spectra	201
A.2.1	Models and Monomers	201
A.2.2	Polymers	213

List of Figures

1.1	Typical rigid rod polybenzobisazoles	2
1.2	Conjugated polymer structure	6
1.3	Band structure in an electronically conducting polymer	7
1.4	Positively charged defects on poly(p-phenylene)	7
1.5	Cyclic voltammogram of a substituted polypyrrole	8
1.6	Three typical redox polymers	9
1.7	Cyclic voltammogram of poly-[Fe(NH ₂ -phen) ₃] ²⁺	11
1.8	Charge propagation by means of quasi-diffusional charge percolation in a redox polymer	11
1.9	Superexchange mechanisms	15
1.10	Cyclic voltammograms and drain current for poly- 8 and poly-[Ru(8) ₃ ²⁺]	21
1.11	Cyclic voltammetry and conductivity profiles	26
1.12	Cyclic voltammetry of (a) PBpy-Ru, (b) PBPY, and (c) Ru(bpy) ₃ ²⁺	32
3.1	Comparative infrared spectra of two PPyBBIM samples (KBr)	71
3.2	Comparative infrared spectra of two PPyBDIM samples (KBr)	72
3.3	Comparative infrared spectra of PPyBBIM isolated during the water extraction stage (KBr)	73
3.4	¹ H NMR spectra of model compound 33 and PPyBBIM	75
3.5	Normalized UV-vis spectra of (A) PPyBBIM , (B) PPyBDIM , (C) PHyBDIM , and (D) PPzBBIM in methanesulphonic acid	77

3.6	Normalized UV-vis spectra of model compounds (A) 35 , (B) 38 , and (C) 36 in methanesulphonic acid	78
3.7	Normalized UV-vis spectra of model compounds (A) 32 , (B) 33 , (C) 34 and (D) 35 in methanesulphonic acid	79
3.8	Model tautomers (a) imidate and (b) amide	81
3.9	HF/3-21G optimized structures of two models	82
3.10	LUMO-HOMO energy gap of the amide tautomer compared to the imidate, for a variety of chain lengths	83
3.11	Energy difference between the imidate and amide tautomers as a function of chain length, at different levels of theory	84
3.12	The Electrode Sauna	86
3.13	Cyclic voltammetry of a thin film of PPyBBIM on a Pt disc electrode in CH ₃ CN containing 0.1 mol dm ⁻³ Et ₄ NClO ₄ showing oxidation and degradation.	88
3.14	Cyclic voltammetry of a thin film of PPyBBIM in CH ₃ CN containing 0.1 mol dm ⁻³ Et ₄ NClO ₄ over a wider sweep width.	89
3.15	Evidence of PPyBBIM degradation by cyclic voltammetry	90
3.16	Cyclic voltammetry of PPyBBIM before and after addition of HClO ₄	91
3.17	Cyclic voltammetry of PPyBBIM before and after addition of Bu ₄ NOH	93
3.18	Cyclic voltammetry of PHyBDIM	94
3.19	Cyclic voltammetry of PPzBBIM	95
4.1	Normalized UV-Vis spectra of Ru-PPyBBIM and PPyBBIM	101
4.2	Spectral changes in Ru-PPyBBIM	102
4.3	Differential spectroelectrochemical response of Ru-PPyBBIM	104
4.4	Differential spectroelectrochemical response of Ru-PPyBBIM	105

4.5	Cyclic voltammetry of Ru-PPyBBIM	107
4.6	Changes in $E_{1/2}$ of a film of Ru-PPyBBIM exposed to a series of aqueous phosphate buffers	108
4.7	Steady state cyclic voltammetry of Ru-PPyBBIM	109
4.8	Gradual migration of the Ru-PPyBBIM Ru(III/II) wave	110
4.9	Cyclic voltammetry of Os-PPyBBIM	111
4.10	Cyclic voltammetry of Os-PPyBBIM in CH_3CN containing HClO_4 or Bu_4NOH	112
4.11	Cyclic voltammetry of Ru-PPzBBIM	113
4.12	Cyclic voltammetry of fully loaded and half loaded Ru-PPzBBIM	114
4.13	Cyclic voltammetry of Os-PPzBBIM	115
4.14	Three consecutive cyclic voltammograms of Ru-PPzBBIM	116
4.15	Polymerizable azopyrrole compounds pyrrolyl-2-aldazine (31) and 2,2'-azopyrrole (61)	117
5.1	SEM image of the cross section of a Ru-PPyBBIM film	121
5.2	Polymer-mediated electron transfer to/from species X in solution	124
5.3	Typical RDV of a mediating film of Ru-PPyBBIM	125
5.4	Linear relationship between $1/i_{\text{leak}}$ and $\omega^{-1/2}$ for a RDV electrode coated with Ru-PPyBBIM	126
5.5	Effect of subtracting i_{leak}	127
5.6	Annotated Ru-PPyBBIM RDV with a large leak current	128
5.7	RDV current looping in Ru-PPzBBIM	129
5.8	Limiting current degradation in two successive sweeps of a film of Ru-PPyBBIM on a RDV electrode.	130
5.9	$\ln i$ vs. $E - E_{1/2}$ for a typical RDV of Ru-PPyBBIM , with the extrapolation line intersecting with $\ln i_{\text{lim}}$ at $E - E_{1/2} = 0$	131

5.10 Illustrative inverse Levich plotted results for an Os-PPyBBIM mediated RDV	133
5.11 Mediated RDV and cyclic voltammograms of Os-PPzBBIM	134
5.12 Schematic representation of a sandwich electrode assembly.	136
5.13 Electron transport in a sandwich electrode assembly.	137
5.14 Typical $i - E$ response in a Ru-PPyBBIM sandwich electrode . . .	139
5.15 Sandwich electrode and cyclic voltammetry of Ru-PPzBBIM	140
5.16 Sandwich electrode and cyclic voltammetry of Os-PPzBBIM	141
5.17 <i>In situ</i> conductivity of Os-PPzBBIM	143
5.18 Proposed energy level schematic of Os-PPzBBIM	145
5.19 Ideal conducting polymer impedance response	148
5.20 Finite transmission line in series with an uncompensated solution resistance	149
5.21 Complex plane impedance of Ru-PPyBBIM in HClO_4 and Bu_4NOH	151
5.22 Representative Z'' vs. $1/\omega$ plot for the determination of C_F	152
5.23 Impedance response as a function of potential in Ru-PPyBBIM . .	153
5.24 Complex plane impedance for a bare Pt disc electrode and one coated with Ru-PPyBBIM	153
5.25 Complex plane impedance spectrum of Ru-PPyBBIM in the mixed solvent system	154
5.26 Equivalent circuit for C_g effects observed in mixed solvent electrolyte solutions	155
5.27 Degradation in three successive complex plane impedance spectra of Ru-PPyBBIM	156
6.1 Thermal and optical ET processes in a symmetric mixed valence complex	164

6.2	Electron transfer in symmetrical mixed-valence systems	166
6.3	Experimental apparatus for measuring IT bands	168
6.4	Raw UV-vis-NIR spectra of Ru-PPyBBIM on an ITO electrode . .	170
6.5	Difference spectra of half- and fully oxidized forms, and IT spectrum from a film of Ru-PPyBBIM	171
6.6	IT band and gaussian curve fit	172

List of Schemes

1.1	Benzimidazole formation in PPA	4
1.2	Poly[5,5'-(2-thienyl)-2,2'-bithiazole] and its Re(I) complexes	17
1.3	Thiophene-capped bipyridine complexation	20
1.4	Bithiophene-capped bipyridine complexation and polymerization	20
1.5	Rotaxane monomer formation	24
1.6	Poly-Rot(8) formation. Poly-Rot(12) is similar.	25
1.7	Re-aryleneethyne copolymer	28
1.8	Copolymers of vinylstyrene and bipyridine or porphyrins	29
3.1	Target thiophene-benzimidazole monomers and byproducts	66
3.2	Dotrong's method	67
3.3	Proposed structures resulting from polymer splitting and tautomerization	80
3.4	Mechanism of polymer deactivation by nucleophilic attack by water	89
5.1	Mediated electron transfer at a rotated electrode	122

List of Tables

3.1	HF/6-31G*//HF/STO-3G HOMO and LUMO energies of 28 and 30	68
3.2	Relative carbon and nitrogen content in polymers as determined by elemental analysis	69
3.3	Selected IR frequencies in cm^{-1} for polymers and model compounds .	70
3.4	Summary of polymer and model optical properties in dimethyl acetamide and in methane sulphonic acid	76
3.5	LUMO-HOMO energy gap for a series of amide and imidate models, and the difference between them	82
4.1	$E_{1/2}$ and ΔE_p of model complexes	97
4.2	Electrochromism in the polymer complexes	103
4.3	Estimated $E_{1/2}$ for the M(III/II) couple for ruthenium and osmium polymer complexes	113
5.1	Summary of RDV mediated results	134
5.2	HF/6-31G*//HF/3-21G energies of the HOMO and LUMO of the indicated compounds	146
5.3	Summary of sandwich electrode results	147
5.4	Summary of impedance results	157
5.5	Summary of D_e results	158

6.1	Electronic coupling H_{AB} calculated from IT data for Ru-PPyBBIM and Os-PPyBBIM and model complexes	173
-----	---	-----

Glossary of Abbreviations

bpy	2,2'-dipyridine
Bu	butyl
BL	bridging ligand
CV	cyclic voltammetry/voltammogram
DMA	<i>N,N</i> -dimethyl acetamide
DMF	<i>N,N</i> -dimethyl formamide
Et	ethyl
FTIR	Fourier transform infrared
HOMO	highest occupied molecular orbital
IR	infrared
IT	intervalence transfer
ITO	indium tin oxide
LUMO	lowest unoccupied molecular orbital
Me	methyl
MLCT	metal-to-ligand charge transfer
MM	molar mass
MP	melting point
MS	mass spectrum
MSA	methanesulphonic acid
NMR	nuclear magnetic resonance
NIR	near infrared
PhyBDIM	"poly hydroxyphenyl benzenediimidazole" (54)
PPyBBIM	"poly pyridine bibenzimidazole" (51)
PPyBDIM	"poly pyridine benzenediimidazole" (52)
PPyBDT	"poly pyridine benzenedithiazole" (53)
PPzBBIM	"poly pyrazine bibenzimidazole" (55)
PBpy	polybipyridine
PPA	polyphosphoric acid
PPy	polypyridine
Rot	rotaxane
r.t.	room temperature
SSCE	saturated sodium chloride calomel reference electrode

TBAOH	tetrabutyl ammonium hydroxide
TEAP	tetraethyl ammonium perchlorate
TAB-4 HCl	tetraminobenzene tetrahydrochloride
TFA	trifluoroacetic acid
TMS	tetramethylsilane
trpy	2,2',6',2''-terpyridine
UV-vis	ultraviolet-visible
vpy	4-vinylpyridine
vtrpy	4'-vinyl-2,2',6',2''-terpyridine
XPS	x-ray photoelectron spectroscopy

Glossary of Symbols

δ	chemical shift
$\Delta\nu_{1/2}$	bandwidth at half intensity
ΔG_{th}^*	thermal electron transfer free energy barrier
Γ	surface coverage
ϵ_{max}	extinction coefficient maximum
μ	charge carrier mobility
ν	scan speed
ν	kinematic solution viscosity
ν_{max}	absorption maximum wavenumber
σ	conductivity
ω	impedance frequency
ω	rotation rate
A	electrode surface area
C_{low}	low frequency capacitance
C_F	Faradaic capacitance
C_g	geometric capacitance
C_x	concentration of x
D_{CT}	charge transport diffusion coefficient
D_e	electron diffusion coefficient
d	film thickness
$E_{1/2}$	half-wave potential
E_g	bandgap
E_{op}	optical electron transfer barrier
E_p	peak potential
E_{pa}	anodic peak potential
E_{pc}	cathodic peak potential
E_{th}	thermal electron transfer barrier
F	Faraday's constant
H_{AB}	electronic coupling
i	current
j	current density
K_{com}	comproportionation constant

M	mol/L
n	number of charge carriers
n	number of electrons
r	metal site separation
R	gas constant
R_{Σ}	total resistance ($R_i + R_e$)
R_e	electronic resistance
R_{high}	high frequency resistance
R_i	ionic resistance
R_{low}	low frequency resistance
R_s	uncompensated solution resistance
s	standard deviation
Z	impedance
Z'	real impedance
Z''	imaginary impedance

CHAPTER 1

INTRODUCTION

1.1 Conjugated Polymers: General Properties

Interest in π -conjugated polymers has continued for a number of years [1-7]. The extensive delocalization of π electrons is well known to be responsible for the array of remarkable characteristics that these polymers tend to exhibit. These properties include non-linear optical behaviour, electronic conductivity, and exceptional mechanical properties [8-10] such as tensile strength and resistance to harsh environments. Polymers composed of aromatic and heteroaromatic ring structures have been particularly outstanding from a materials perspective [4].

Applications in advanced aerospace technology have provided a powerful impetus for the development of specialized polyheteroaromatics. For instance, the United States Air Force Wright Laboratory has for nearly thirty years been engaged in an intense effort to develop polymers and molecular composites suitable for aircraft structure [1]. Much of their early work was based on fused heteroaromatic polymers ("ladder" polymers). Later investigations were directed to rigid rod polymers based on the polybenzobisazole family, for example the poly-[benzobisazole-phenylene] structures shown in Figure 1.1. These materials are of particular interest due to their unusually

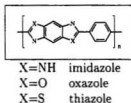


Figure 1.1: Typical rigid rod polybenzobisazoles

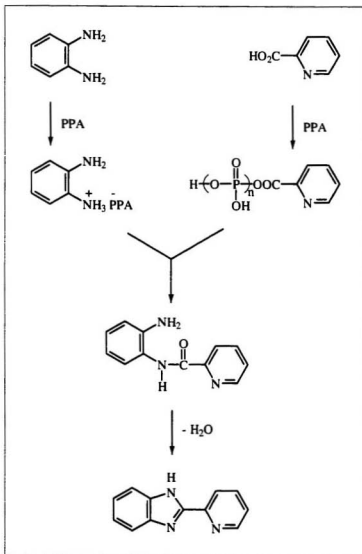
high tensile strength and modulus in addition to their exceptional chemical, thermal, and environmental stability. Owing to these last three properties, polybenzimidazoles have found useful application as fire-resistant materials [11] such as fireman's coats.

In general, polymers based on the benzimidazole fragment in particular have long been recognized for their useful engineering properties and resilience. A 1961 review of polybenzimidazoles [2] confirmed their ability to withstand extended exposure to elevated temperatures, strong acids, and oxidizing agents, even though the less than adequate synthetic methods of the time (primarily melt condensations) produced polymers of relatively poor quality.

The preferred method of synthesizing polymers based on the benzobisazole fragment is the condensation reaction between a carboxylic acid and an appropriate substituted phenyl ring in polyphosphoric acid (PPA) [1, 8, 11]. This is shown in general in Scheme 1.1. This approach is known to be significantly more reliable than older [2] techniques such as high temperature melt reactions between diamines (for benzimidazoles) and acids or esters, and the interfacial polycondensation (or, perhaps more appropriately, oligomerization) of diamines with acid chlorides.

It has been shown [8] for the formation of a benzothiazole polymer that the polyamide intermediate occurs at a relatively low temperature (120 °C) while the cyclization step does not occur until much higher temperatures (180 °C). At the elevated temperatures, monomer stability becomes an issue, so the temperature must be carefully ramped during the course of the polymerization so as not to expose the starting materials to potentially damaging conditions.

A useful variation on the PPA condensation procedure is Wolfe's P_2O_5 adjustment method [12–15]. It compensates for the water of condensation through the addition of extra P_2O_5 during the course of the reaction. In its full implementation, the ratio of water to P_2O_5 content is carefully manipulated in order to control the viscosity of the reaction medium through the various stages with the intent of managing the physical characteristics of the resulting fibre or film.



Scheme 1.1: Benzimidazole formation in PPA

In cases where the physical structural properties of these polyazoles are of concern, it has been shown [15] that the concentrations of the reagents in PPA can be important parameters, influencing the state of the polymer in solution, *i.e.*, whether it exists as an isotropic or liquid crystalline solution, which has some apparent influence on the average chain length.

1.2 Conjugated Polymers: Electronic Conductors

The most important aspect of conjugated polymers from an electrochemical perspective is their ability to act as electronic conductors. Not surprisingly π -electron polymers have been the focus of extensive research [16], ranging from applications of “conventional” polymers (*e.g.*, polythiophene, polyaniline, polypyrrole) in charge storage devices such as batteries and supercapacitors, to new polymers with specialized conductivity properties such as low bandgap and intrinsically conducting polymers. Indeed, many successful commercial applications of these polymers have been available for more than fifteen years, including electrolytic capacitors, “coin” batteries, magnetic storage media, electrostatic loudspeakers, and anti-static bags. It has been estimated [6] that the annual global sales of conducting polymers in the year 2000 will surpass one billion US dollars. Clearly these materials have considerable commercial potential both from the continued development of well established technologies and from the generation of new concepts such as those to be presented in this thesis.

The genesis of the field can be traced back to the mid 1970s when the first polymer capable of conducting electricity — polyacetylene — was reportedly prepared by accident by Shirakawa [17]. The subsequent discovery by Heeger and MacDiarmid [18] that the polymer would undergo an increase in conductivity of 12 orders of magnitude by oxidative doping quickly reverberated around the polymer and electrochemistry communities, and an intensive search for other conducting polymers soon followed.

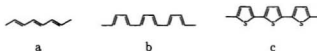


Figure 1.2: Conjugated polymer structure: (a) trans- and (b) cis-polyacetylene, and (c) polythiophene

The target was (and continues to be) a material which could combine the processibility, environmental stability, and weight advantages of a fully organic polymer with the useful electrical properties of a metal.

The essential structural characteristic of all conjugated polymers is their quasi-infinite π system extending over a large number of recurring monomer units. This feature results in materials with directional conductivity, strongest along the axis of the chain [19]. The simplest possible form is of course the archetype polyacetylene $(\text{CH})_x$ shown in Figure 1.2. While polyacetylene itself is too unstable to be of any practical value, its structure constitutes the core of all conjugated polymers. Owing to its structural and electronic simplicity, polyacetylene is well suited to *ab initio* and semi-empirical calculations and it has therefore played a critical role in the elucidation of the theoretical aspects of conducting polymers.

Electronically conducting polymers are extensively conjugated molecules, and it is believed that they possess a spatially delocalized band-like electronic structure [7, 20]. These bands stem from the splitting of interacting molecular orbitals of the constituent monomer units in a manner reminiscent of the band structure of solid-state semiconductors (Figure 1.3).

It is generally agreed [16, 21] that the mechanism of conductivity in these polymers is based on the motion of charged defects within the conjugated framework. The charge carriers, either positive p-type or negative n-type, are the products of oxidizing or reducing the polymer respectively. The following overview describes these processes

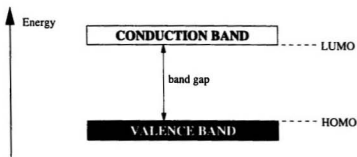


Figure 1.3: Band structure in an electronically conducting polymer

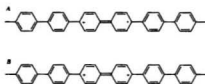


Figure 1.4: Positively charged defects on poly(p-phenylene). A: polaron B: bipolaron in the context of p-type carriers although the concepts are equally applicable to n-type carriers.

Oxidation of the polymer initially generates a radical cation with both spin and charge. Borrowing from solid state physics terminology, this species is referred to as a polaron and comprises both the hole site and the structural distortion which accompanies it. This condition is depicted in Figure 1.4A. The cation and radical form a bound species, since any increase in the distance between them would necessitate the creation of additional higher energy quinoid units. Theoretical treatments [22, 23] have demonstrated that two nearby polarons combine to form the lower energy bipolaron shown in Figure 1.4B. One bipolaron is more stable than two polarons despite the coulombic repulsion of the two ions. Since the defect is simply a boundary between two moieties of equal energy — the infinite conjugation chain on either

side — it can migrate in either direction without affecting the energy of the backbone, provided that there is no significant energy barrier to the process. It is this charge carrier mobility that leads to the high conductivity of these polymers.

The conductivity σ of a conducting polymer is related to the number of charge carriers n and their mobility μ :

$$\sigma \propto n\mu \quad (1.1)$$

Because the band gap of conjugated polymers is usually fairly large, n is very small under ambient conditions. Consequently, conjugated polymers are insulators in their neutral state and no *intrinsically* conducting organic polymer is known at this time. A polymer can be made conductive by oxidation (p-doping) and/or, less frequently, reduction (n-doping) of the polymer either by chemical or electrochemical means, generating the mobile charge carriers described earlier. The cyclic voltammetry of electronically conducting polymers is characterized by broad non-Nernstian waves. A typical example is shown in Figure 1.5 for an *N*-substituted pyrrole based conducting polymer [24].

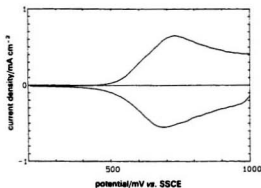


Figure 1.5: Cyclic voltammogram of a substituted polypyrrole [24]. Reprinted with permission from *J. Chem. Soc. Faraday Trans.*, 1990, **86**, 3631. Copyright 1990 The Royal Society of Chemistry

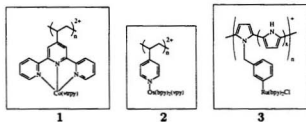


Figure 1.6: Three typical redox polymers

1.3 Redox Polymers

In contrast to the conjugated polymers there also exists another class of conducting polymer, namely the redox polymers. These polymers are characterized by the presence of specific spatially and electrostatically isolated electrochemically active sites. Electroactivity in the redox polymer is highly localized, while the electrochemical processes in conjugated polymers lead to a reorganization of the bonds in the molecule itself. Typically, a redox polymer consists of a system where a redox-active transition metal based pendant group is covalently bound to some sort of polymer backbone which may or may not be electroactive (although for synthetic convenience the backbone is frequently formed by the electropolymerization of suitable monomer complexes). A few representative examples are shown in Figure 1.6. The widespread interest in these polymers has been spurred by their applicability in the area of chemically modified electrodes [25–27]. One goal of coating electrodes with electroactive polymers is the development of new materials with very active catalytic properties. The bulk of the work has been with systems where the polymer itself is inert and serves only as a support for the electrocatalytic metal sites. The electrocatalyst site functions as a mediator, facilitating the transfer of electrons between the electrode and the substrate. Electrocatalysis in general is of great economic importance and the aim of these modified electrodes is to drive electrochemical reactions selectively

and/or at modest potentials, and with better control than could be possible by the direct interaction between the substrate and the electrode. The electrocatalytic reduction of O_2 is one example which has been of particular interest [27–31] for fuel cell applications.

Embedding electrocatalytic transition metal species in a polymer modified electrode matrix is a means to endow the electrode with the chemical, electrochemical, optical, and other properties of the immobilized molecule [25]. A number of additional advantages include:

1. Control of the reaction rate by the applied potential or current.
2. Close proximity of electrocatalytic sites to the electrode.
3. High concentration of active centres despite low amount of material required.
4. Cooperative effects stemming from the proximity of other catalyst sites.
5. Easy removal of the catalyst from the substrate.

Unlike the electronically conducting polymers, redox polymers characteristically exhibit conductivity only over a very narrow potential range, with maximum conductivity occurring when the concentrations of the oxidized and reduced forms are equal in the film, *i.e.*, at the formal potential of the redox centres. This leads to a voltammetric profile such as the one shown in Figure 1.7, with the characteristics of a surface bound redox system (or finite linear diffusion), $\Delta E_p \sim 0$ and $i_p \propto \nu$.

The details of charge transport between the electrode and the supported redox sites is a fundamental consideration. It is commonly held that redox conduction in polymers occurs by the electron hopping process proposed by Kaufman and coworkers [33, 34] whereby electron transfer proceeds as a process of sequential self-exchange

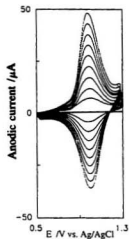


Figure 1.7: Cyclic voltammogram of a poly- $[\text{Fe}(\text{NH}_2\text{-phen})_3]^{2+}$ coated Pt disc electrode in acetonitrile containing 0.2 M Et_4ClO_4 , scanned between 100 and 900 mV/sec in 100 mV/sec intervals [32]. Reprinted with permission from *J. Electroanal. Chem.*, 1994, **365**, 289. Copyright 1994 Elsevier Science.

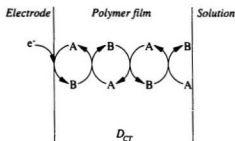


Figure 1.8: Charge propagation by means of quasi-diffusional charge percolation in a redox polymer

steps between adjacent redox groups. The rate of self exchange R_{SE} and electron transfer (ET) processes are connected by the simple relationship $R_{SE} = k_{ET}C_{ox}C_{red}$. In the polymer film where the total amount of redox species must be fixed (i.e., $C_{ox} + C_{red} = C_{tot}$) the self-exchange rate will reach a maximum when the concentration of both species is equal, i.e., $C_{ox} = C_{red}$, hence maximum conductivity occurs at E° . The sequence of self-exchanges which give rise to conductivity through the thickness of the film is depicted in Figure 1.8. Two processes are involved. The first is charge injection at the polymer-electrode interface, which involves redox sites close (ca. 1 nm [35]) to the surface. This is a potential-driven process and conforms to Butler-Volmer kinetics. The second process is the percolation of charge through the film which is (to a first approximation) driven by concentration gradients and is quantifiable as a quasi-diffusional process. While more sophisticated models have been developed [36–40], the linear diffusion gradient approach accounts for most of the charge transport behaviour in redox films and provides an adequate foundation for the work in this thesis.

Since electroneutrality in the film must be maintained, the generation of charge at the electrode and the motion of the charge throughout the polymer must be accompanied by the ingress and motion of counterions. This is an important consideration since electroactive polymers are really mixed conductors, displaying both electronic and ionic conductivity. Often the ionic contribution may be safely disregarded, in which case the charge transport diffusion D_{CT} may be ascribed entirely to electron diffusion D_e . However this is not always the case, and electron hopping rates can be strongly influenced by the nature of the counterion [32, 41]. Full characterization should consider both electronic and ionic conductivities of the material.

1.4 Conjugated Redox Polymers: Hybrid Materials

The rate of electron exchange between the electrode and the catalyst sites is of obvious importance in the context of electrocatalysis. Facilitated electron transfer will translate to higher turnover rates. It was shown in the preceding sections that redox polymers have a somewhat slow rate of electron transport by self-exchange through a potential gradient, and that electronically conducting polymers exhibit rapid electron transport through a delocalized electronic structure. A polymer which somehow combines these properties would clearly be desirable; the use of an electronically conducting polymer as an electron pipeline is intuitively sensible. Early attempts to combine redox-active centres with conjugated backbones [42], such as the copolymer **3** [43] (see figure 1.6), showed little improvement. In these cases the redox active group was held at some distance from the conjugated backbone by a saturated link and was therefore effectively isolated electronically from the backbone.

This thesis introduces the concept of coordinating a metal atom directly into the long-range π system of a conjugated polymer as a means of enhancing electron transport. We have come to call these systems “conjugated/redox polymer hybrids” or “conjugated metallopolymers”. At the onset of this project, only a few examples of this class of material existed in the literature, but they demonstrated many novel properties. Since then a few more examples have been reported including several from this research group [44–47]. Polymer hybrids have also been featured in two recent review articles [48, 49]. It should be noted that a closely related type of polymer where a metal atom forms a bridge between two conjugated segments, for instance polyferrocenes [50, 51], salen-based polymers [52–54], and the meta-linked bpy system of Petersen [55], has also been of interest. However, since these polymers do not possess

a quasi-infinite conjugated backbone they will be considered outside the scope of this work.

The premise is that the hybrid system will facilitate self-exchange in much the same way that conjugated bridging ligands lead to more rapid self-exchange in dinuclear complexes [56]. One means of assessing the relative strength of the interactions between the bridged pair is through the comproportionation constant K_{com} . For the hypothetical system



$$K_{com} = \frac{[M-L-M]^{n+}]^2}{[M-L-M]^{(n-1)+} [M-L-M]^{(n+1)+}} \quad (1.2)$$

$$= \exp \left[\frac{(E_1^+ - E_2^+)F}{RT} \right] \quad (1.3)$$

The strength of the interaction through the bridge is indicated by the separation of the voltammetric waves. [57]

The stability of the mixed valence state is a reflection of the strength of the electronic interactions between metal atoms, and this can be assessed voltammetrically if the interaction is strong enough. Materials that possess these strong interactions are being examined for use in advanced applications such as energy storage and molecular electronics [58].

Conjugated bridging ligands are advantageous as they allow the metal atoms to interact through the adjoining π segment, influencing the metal-metal communication. It has been recognized [59] in dinuclear Ru(II) complexes bridged by a conjugated ligand that K_{com} is primarily related to the orbital overlap between the metal atoms and the bridging ligand. The distance between metal centres is apparently less important. In a series of dinuclear Ru(II) complexes bridged with benzimidazole- and

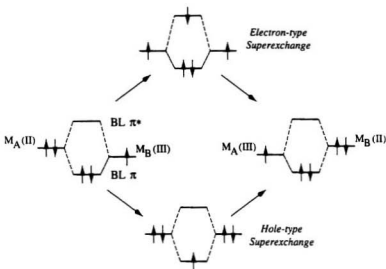


Figure 1.9: Superexchange mechanisms. BL=bridging ligand

benzothiazole-based ligands [60–64] a superexchange mechanism is believed to be at play. As indicated in Figure 1.9, two pathways are possible. In the hole-type superexchange pathway, an electron is promoted from the bridging ligand (BL) HOMO to the $M(III)$ site, giving the symmetric transition state with both metals in the reduced form. The missing electron from the BL HOMO is subsequently replaced by an electron from the other metal atom, resulting in a system where the valences have been swapped. Conversely, electron-type superexchange involves the transition of an electron from the $M(II)$ state metal to the BL LUMO, leaving a symmetric transition state with the metals in the oxidized form. Exchange is completed by the electron's transfer to the opposing $M(III)$ atom. The preferred pathway and the ease with which it is taken depend on the relative energies of the metal orbitals and the BL π or π^* orbitals; metal-d and BL- π orbital mixing leads to hole superexchange and metal-d and BL- π^* orbital mixing leads to electron superexchange. In either route the valences are interchanged, enhancing stability of the mixed valence system.

We propose that the concept of the bridging ligand superexchange mechanism can be extended to describe long distance charge migration in a hybrid polymer, with infinite propagation being achieved through the sequential superexchanges between neighbouring redox sites

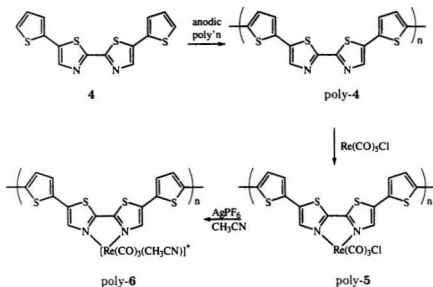
1.4.1 Conjugated Metallopolymers in the Literature

1.4.1.1 Poly[5,5'-(2-thienyl)-2,2'-bithiazole]

Wolf and Wrighton reported [65] the synthesis of the novel conducting polymer poly-**4** via the anodic polymerization of 5,5'-(2-thienyl)-2,2'-bithiazole which was prepared by the Stille coupling of 2-bromothiophene with 5,5'-(trimethylstannyl)-2,2'-bithiazole. The conjugated cationic Re metallopolymer poly-**6** was also prepared. This work represents an early attempt to combine the unique characteristics of conjugated conducting polymers with catalytic metals to form interesting new materials. It recognizes that the oxidation state of adjoining ligands has an impact on the catalytic properties of the central metal atom [66], and that the wide range of "oxidation states" that a conducting polymer displays might be potentially employed to tune the response of the electrocatalytic group.

The strategy of using moieties that are easily polymerized electrochemically, thiophene for instance, to cap aromatic monomers which do not polymerize readily is a sound one [67]. Electropolymerization of bithiazole was unsuccessful [68,69] and chemical polymerization of bithiazole via Grignard coupling only produced a polymer with very low conductivity [68]. The electrochemically polymerized thiophene substituted bithiazole gave a much more satisfactory conductivity, *ca.* 0.2 S/cm at 1.5 V *vs.* Ag wire as measured *in situ* on specially constructed microelectrode arrays.

Studies of bithiazole model compounds showed that the chloro complex exhibited an irreversible wave near 1.4 V *vs.* SCE. Substitution of Cl with CH₃CN however gave



Scheme 1.2: Poly[5,5'-(2-thienyl)-2,2'-bithiazole] and its Re(I) complexes

cyclic voltammograms with a reversible metal-based wave at 1.8 V. The complex poly-5 was prepared by immersing the polymer coated electrode in a refluxing chloroform solution of $\text{Re(CO)}_5\text{Cl}$ for several minutes. Subsequent treatment with a solution of AgPF_6 in CH_3CN yielded poly-6, in accordance with Scheme 1.2. The cyclic voltammetry of the polymer derivative is not as clear as for the monomer complex since the polymer and metal waves overlap.

The carbonyl ligands serve as a useful infrared handle by which the electron density at the Re atom may be monitored. Surface reflectance IR spectra of films of poly-6, which had been oxidized at +1.5 V and removed from solution under potential control, showed frequency shifts from 2040 to 2044 cm^{-1} and from 1934 to 1940 cm^{-1} . Films which had been oxidized for 30 s and returned to 0 V did not show such a shift. There is no mention of attempts to measure spectra under potentiostatic control. The band

shift effect is seen at a potential below the formal potential of the Re oxidation, and so it is concluded that the electron density of the partially oxidized polymer backbone modulates the density on Re and consequently the ancillary CO ligands. This shows how the electronic characters of the polymer and the metal are intimately related. While the effect seems small, minor electronic energy changes at the metal centre can have an enormous impact on the reactivity. For example it has been pointed out that a 15 cm^{-1} shift in the carbonyl stretch of a comparable Re complex is accompanied by a two hundred-fold increase in the rate of nucleophilic attack upon the metal [70].

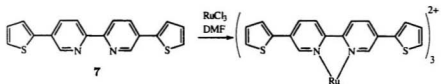
The metallopolymers were characterized by XPS and surface reflectance IR. From comparisons of the Re 4f peaks with the S and N peaks in the XPS spectrum it was estimated that 60-75% of available coordination sites were occupied. It was noted that the complexed polymer exhibited a drop in conductivity of three orders of magnitude compared to the parent polymer, a phenomenon that the authors ascribe to "less delocalization of the charge carriers" in the polymer complex. It was also observed that the metallopolymer's electrochemistry was much more stable towards exposure to elevated potentials. The explanation offered suggests that deactivation of the backbone occurs at the nitrogen atoms, and the metal atoms in poly-6 physically block access to these regions. This reasoning is questionable since it does not account for the vacancy of up to 40% of the sites; attack at the remaining uncomplexed nitrogen atoms should lead to a much greater effect than the one seen. An alternate rationale based on the "less delocalization" hypothesis might state that the buildup of positive charge primarily at the Re atoms only (even though the potentials were kept below $E_{1/2}\text{ Re(II/I)}$ as measured in the model complexes) makes nucleophilic attack at other regions of the polymer less favourable. An alternate explanation for the stability enhancement and the conductivity loss can be proposed from geometric considerations. The influx of the bulky metal groups into the solid polymer results

in the torsion of many of the bithiazole groups out of the plane of the thiophene rings. The twist reduces p-orbital overlap and hence conjugation is diminished. This reasoning accounts for both the drop in conductivity upon derivatization and for the greater perceived electrochemical stability. Since the conjugation is already disrupted, any additional defects stemming from deactivation will be insignificant. The twisted polymer hypothesis also introduces the disturbing notion that double bond reorganization, the process so critical for rapid charge transport, is blocked in twisted poly-**6** and that the experimental results are therefore largely irrelevant.

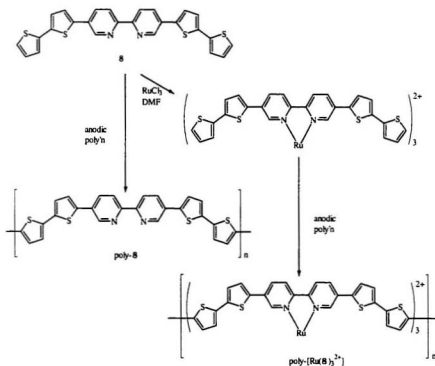
1.4.1.2 Thiophene-bipyridine copolymers

Swager and co-workers have employed Wrighton's strategy of affixing thiophene units to a bidentate ligand as a route to readily electropolymerized metallopolymer [71–74] based on 2,2'-bipyridine. Bipyridines capped with thiophene **7** and bithiophene **8** were prepared along with their Ru complexes. Strangely, only the bithiophene-capped species could be electropolymerized. The formation of the complex before polymerization (see Scheme 1.4) is advantageous in that 100% occupancy of the sites is assured (provided that no decomplexation occurs during the polymerization), presenting a more regular environment for the metal centres as well as forming a better characterized film. The electrochemical responses of poly-**8** and poly-[Ru(**8**)₃²⁺] are shown in Figure 1.10.

The oxidative cyclic voltammetry of poly-**8** shows the p-doping wave shape and position typical of a thiophene polymer [19]. An n-doping wave is also evident at a potential much less negative than usual for a thiophene polymer, but very similar in shape and position to the n-doping wave of poly-bipyridine [75]. This indicates that the p-doping and n-doping processes are localized on the thiophenes and pyridines respectively. (The region of non-conductivity between the waves – the band gap – in



Scheme 1.3: Thiophene-capped bipyridine complexation



Scheme 1.4: Bithiophene-capped bipyridine complexation and polymerization

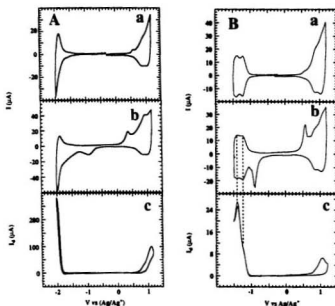


Figure 1.10: Cyclic voltammograms at 100 mV/sec (a and b) and drain current ($I_d \times$ conductivity) profile (c) for **A**:poly-**8** and **B**:poly-[Ru(**8**)₃²⁺] on interdigitated microelectrode arrays (10 μm spacing) in acetonitrile containing Bu₄PF₆. Panel b shows the cyclic voltammetry over a potential range which includes both oxidation and reduction of the polymer [71]. Reprinted with permission from *Adv. Mater.*, 1996, **8**, 497. Copyright 1996 Wiley-VCH Verlag GmbH.

this copolymer is smaller than in the parent homopolymers.) The small peaks on the full range sweeps are a result of charge trapping [76] and therefore provide further indications of charge localization.

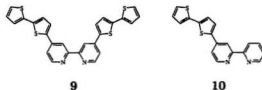
Poly-**8** shows a maximum p-type conductivity of ca. 2×10^{-3} S/cm at ca. +1.0 V and a maximum n-type conductivity of ca. 4×10^{-3} S/cm at ca. -2.0 V. This is an interesting condition since polythiophenes generally exhibit much higher p-type conductivity. In this case it suggests that the bipyridine segments inhibit to some extent the delocalization of the p-type charge carriers [48]. This is not unreasonable in light of their π deficient nature and the fact that polypyridines can not be p-doped within

the normally accessible potential range [75].

The cyclic voltammetry of poly-[Ru(**8**)₃²⁺] in the positive potential region is similar to that of poly-**8**, further indicating the lack of contribution of the bipyridine segment to the electrochemistry of this region. There is no mention of the Ru(III/II) wave which should appear at potentials slightly more positive than the upper sweep limit in Figure 1.10B. This is unfortunate since the double thiophene substitution should facilitate oxidation of the polymer, encouraging hole superexchange.

The cathodic electrochemistry shows a pair of bpy-based reductions at -1.23 and -1.39 V, characteristic of Ru(bpy)₃²⁺ type complexes (*e.g.*, see Figure 1.12C). The monomer complexes exhibit similar waves at slightly more negative potentials, at -1.32 and -1.56 V for Ru(**7**)₃²⁺, and at -1.34 and -1.54 V for Ru(**8**)₃²⁺. Curiously these reductions were assigned to Ru(II/I) and Ru(I/0) processes. The conductivity profile of the reduction waves is characteristic of a redox polymer, being at a maximum (or a shoulder for the first wave) at *E*^o. This behaviour is analogous to the non-conjugated polymer poly[Os(bpy)₂(vpy)₂] [77], suggesting that the n-type charge carriers are mostly localized in the bipyridine portion of the polymer. The small shifts in reduction potentials in these systems compared to Ru(bpy)₃(PF₆)₂ (by *ca.* 35–40 mV) and the somewhat higher conductivity than poly[Os(bpy)₂(vpy)₂] indicate that there is weak delocalization across the thiophene units. This is further supported by the observation that damaging the polymer conjugation by exposure to very negative potentials leads to a decrease in conductivity and loss of definition of the two bpy reduction waves.

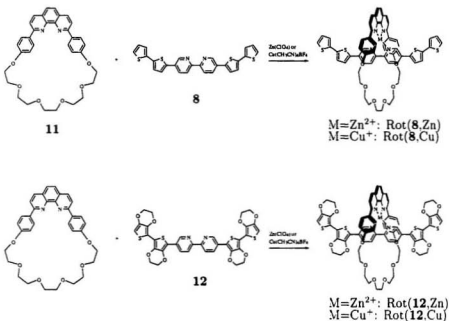
The related isomer **9** and its analogue with only one biethienyl substituent **10**, along with their Ru(II) complexes were recently reported [72]. Owing to the *meta*-relationship of the parent monomer, the electrochemically generated poly-**9** does not possess extended conjugation. Not surprisingly, this polymer did not exhibit conductivity above the detection limit of the experimental conditions (10⁻⁶–10⁻⁷ S/cm).



In contrast, the metallopolymer poly-[Ru(**9**)₃²⁺] showed a maximum conductivity of 3.3×10^{-3} S/cm, which is 2.8 times greater than the conductivity of the conjugated polymer poly-[Ru(**8**)₃²⁺]. Evidently, the self-exchange between adjacent Ru sites is enhanced by having the tetrathienyl bridge *para* to the metal, creating a conjugated link. The presence of the metal atom is crucial, since the parent polymer is essentially non-conductive. Cross-linking of chains has an additional influence on the electrochemistry of poly-[Ru(**9**)₃²⁺] since the conductivity of the related polymer complex poly-[Ru(**9**)(bpy)₂²⁺] was an order of magnitude lower.

Charge transport occurs through the Ru(II) atom. In poly-[Ru(**10**)₃²⁺], where an entirely organic backbone is prohibited, the conductivity is only slightly lower than that of poly-[Ru(**9**)(bpy)₂²⁺].

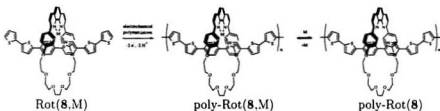
While this metallopolymer displays some interesting behaviour, it probably would be unsuitable for use in electrocatalytic systems because of the critical role the metal atom plays in the conduction mechanism. Accidental decomplexation of even a small fraction of sites would have a very detrimental effect on the polymer's conductivity. Indeed it was pointed out that the polymer complex is not electrochemically stable in CH₃CN, and that experiments had to be undertaken in CH₂Cl₂, a non-coordinating solvent. Partial dissociation of polypyridine-type ligands upon reduction has been observed in other systems [28], and presumably a similar mechanism might account for the instability of poly-[Ru(**9**)(bpy)₂²⁺] in conditions that stabilize the dissociation product. Under reductive conditions, the presence of a coordinating solvent could



Scheme 1.5: Rotaxane monomer formation

facilitate total dissociation of a small number of complexes in the backbone, leading to disastrous loss of conductivity. Systems with a true conjugated backbone such as poly- $[\text{Ru}(\mathbf{8})_3^{2+}]$ would be much less sensitive to the loss of metal sites. The original experiments on poly- $[\text{Ru}(\mathbf{8})_3^{2+}]$ were performed in CH_3CN .

Electropolymerizable $\text{Zn}(\text{II})$ and $\text{Cu}(\text{I})$ complexes of phenanthroline-containing macrocycle **11** with **8** and its dioxymethylene analogue **12** have been prepared [73, 74]. Anodic polymerization produces the corresponding “polyrotaxanes” poly-Rot(**8**,M) and poly-Rot(**12**,M) ($\text{M}=\text{Zn}$ or Cu) where the polymer chain is threaded through the macrocycle rings [78, 79]. Following extraction of the metal ion by treatment with ethylenediamine, the macrocycle necessarily remains physically associated with the polymer, giving poly-Rot(**8**) and poly-Rot(**12**). This threaded motif is important



Scheme 1.6: Poly-Rot(8) formation. Poly-Rot(12) is similar.

since it provides well-behaved reversible complexation. Spectroscopic studies proved that the coordination and removal of the metal atom is completely reversible. The design was intended as a prototype receptor site for polymer-based sensors. It has been suggested [80] that molecular wire type polyreceptors could produce useful signal amplification in the design of extremely sensitive chemodetectors.

The cyclic voltammetry of the decomplexed poly-Rot(12) (Figure 1.11A) is rather unusual in that a pair of distinct redox waves are clearly evident, rather than the broad wave of p-doping current normally associated with conducting polymers (*cf.* Figure 1.5). The conductivity profile shows a maximum at the potential of the first wave, followed by a sharp decrease and a second maximum at the second wave. This behaviour is indicative of a charge-localized redox polymer which is reasonable given the alternation of strong donor tetra(ethylenedioxythiophene) segments and strong acceptor bipyridine segments [48]. The p-type carriers would be expected to reside primarily on the tetra(ethylenedioxythiophene) units, with the two voltammetric waves corresponding to the creation first of polarons and then bipolarons.

The complexes poly-Rot(12,Zn) and poly-Rot(12,Cu) also show highly localized cyclic voltammogram character, with small ΔE_p and $i \propto \nu$. The addition of Zn(II) or Cu(I) causes a sharpening of the voltammetric waves and a significant loss in conductivity (note the scales in Figures 1.11A and 1.11B), indicating reinforcement of the

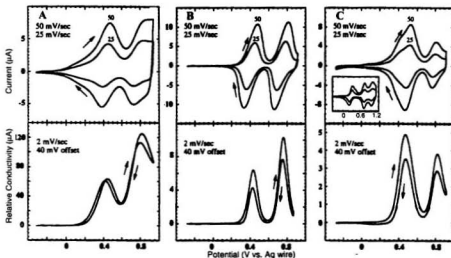
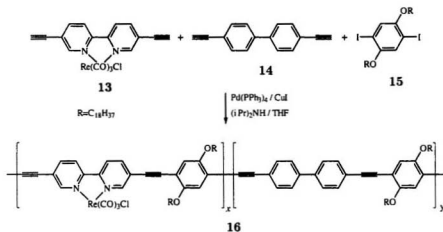


Figure 1.11: Cyclic voltammetry and conductivity profiles for (A) poly-Rot(12), (B) poly-Rot(12,Zn), and (C) poly-Rot(12,Cu) with poly-Rot(8,Cu) inset in CH_2Cl_2 containing Bu_4PF_6 [74]. Reprinted with permission from *J. Am. Chem. Soc.*, 1997, 119, 12568. Copyright 1996 American Chemical Society.

localization of p-type charge carriers. In Figure 1.11C, poly-Rot(12,Cu) shows the added contribution of the Cu(II/I) wave, superimposed on the first redox wave. This wave is clearer in the inset poly-Rot(8,Cu) voltammogram, where the redox waves of the polymer occur at higher potential in the absence of the electron-rich ethylenedioxythiophene moieties. The copper wave serves as a useful coulombic reference, showing that each of the two polymer waves does indeed correspond to the removal of one electron per repeat unit. The conductivity profile of poly-Rot(8,Cu) indicates that the Cu(II/I) wave does not contribute significantly to conductivity, presumably as a result of kinetic sluggishness [73]. Therefore the enhanced conductivity of the first wave in poly-Rot(12,Cu) over the first wave in poly-Rot(12,Zn) cannot be ascribed to a simple additive contribution. Evidently Cu(II/I) is mediating the electron exchange between the tetra(ethylenedioxythiophene) segments. This is an interesting

development, although the simple conductivity measurements do not supply adequate information to draw conclusions about the mechanisms at work.

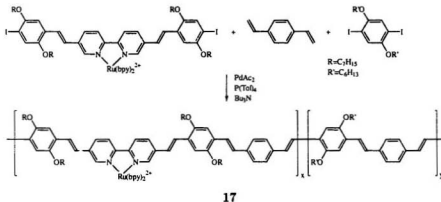
The interactions of poly-Rot(**8**) and poly-Rot(**12**) with Cu(II) present an interesting situation. It was found that poly-Rot(**8**) does not have a high affinity for Cu(II) ions, while poly-Rot(**12**) does. It turns out that this behaviour is probably connected to the electronic nature of the two ligands. The electron-rich ethylenedioxythiophene units in poly-Rot(**12**) enhance its chelating ability by increasing the basicity of the bipyridine segments and biasing the macrocycle towards the bipyridine segments. Some striking results from resistance measurements suggest there is a more intricate mechanism at work. The treatment of poly-Rot(**12**) with Cu(II) led to a decrease in dry resistance by a factor of over 10^6 . Similar treatments with Cu(I) or Zn(II) led to a modest tenfold change in the resistance, while the reaction with Cu(II) with poly-Rot(**8**) resulted in a drop by a factor of only 10^2 . It would seem that the close proximity of the redox potentials of the first poly-Rot(**12**) wave and the Cu(II/I) couple permit the Cu(II) ion to oxidize the polymer, effecting chemical p-doping. Presumably the need for the copper ion to comply with the imposed tetrahedral geometry helps to drive the metal towards the Cu(I) state, although this issue was not mentioned. The reaction of the macrocycle-free poly-**12** with Cu(II) also results in a large resistance drop, although the possible contribution of Cu bridging adjacent polymer chains is not addressed. The resistance results are significant to sensory applications in that they demonstrate how the reversible perturbation of a potential analyte can induce very large changes in a parameter which is almost trivially simple to measure.



Scheme 1.7: Re-aryleneethynyl copolymer

1.4.1.3 Copolymerized 5,5'-diethynyl-2,2'-bipyridine

A series of conjugated polymers containing $\text{Re}(\text{CO})_3\text{Cl}$ (Scheme 1.7) were prepared in order to explore possible interactions between two distinct and well defined chromophores: the polymer backbone $\pi \rightarrow \pi^*$ absorption and the lower energy $d\pi(\text{Re}) \rightarrow \pi^*_{\text{poly}}$ metal to ligand charge transfer [81, 82]. The overall composition of the polymer was controlled by the relative proportions of **13** and **14** used in the polymerization process. The photophysical response of the polymer **16** variants was characteristic of the individual components; the chromophores were apparently not strongly coupled. It was proposed that the unusually weak communication was due either to irregularity in the polymers' composition — blocks of **13** and **15** and blocks of **14** and **15** as opposed to the regular alternation depicted in Scheme 1.7 — or that the energy crossover between excited states was inefficient. The electrochemistry of the system was not examined, and it is difficult to predict whether comparably poor coupling would appear in the longer timescale of electrochemical experiments.

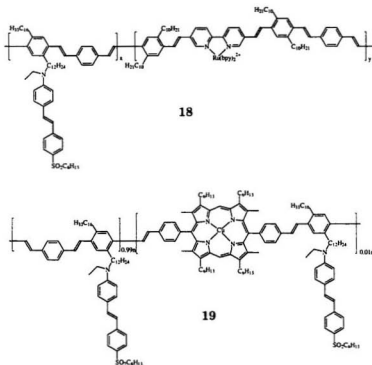


Scheme 1.8: Copolymers of vinylstyrene and bipyridine or porphyrins

1.4.1.4 Copolymerized 2,2'-bipyridine, vinyl styrene

A similar strategy of varying the relative proportions of starting materials was used by Yu *et al.* in the synthesis of several polymers of the general form **17** for the purpose of creating new photorefractive materials [83]. This approach allows specific control of the metal loading. $\text{Ru}(\text{bpy})_3^{2+}$ forms the core of their system owing to its efficient MLCT [84,85] which serves as a charge generation source, while the conjugated backbone is intended to function as a charge transport channel and non-linear optical chromophore. A light induced MLCT will in this case be equivalent to injecting an n-type carrier into the polymer backbone, and should therefore contribute to conductivity. As before, the coordination of $\text{Ru}(\text{II})$ before polymerization assures 100% site occupancy.

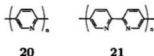
As expected, the polymers exhibited photoconductivity when exposed to 690 nm light from a diode laser. The polymers containing the ruthenium moiety ($x = 0.1$) displayed a much greater response than the one without ($x = 0$), indicating the validity of using metal complexes as photosensitizers.



Yu and coworkers have also reported [86] the low glass transition temperature (T_g) polymers **18** and **19** for photorefractivity study. The photoconductive sensitivity of **19** was found to be two orders of magnitude lower than **18**, presumably as a result of its less efficient MLCT process and faster relaxation of the excited state. It was not, however, prone to the local shielding effects found in the ionic metal site in **18**. These effects are detrimental to the photophysical performance of these systems.

1.4.1.5 Polypyridine and polybipyridine

Yamamoto and coworkers have reported several conjugated polymers based on polypyridine **20** (PPy) and polybipyridine **21** (PBpy) along with methyl- and hexyl-substituted variants [75, 87–89] via zerovalent nickel coupling of the corresponding



dihalo compounds. Complexes with $\text{Ru}(\text{bpy})_2^{2+}$, NiCl_2 , $\text{Cu}(\text{I})$, and $\text{Fe}(\text{bpy})_2^{2+}$ were reported and were the first bipyridine-based metallopolymer.

The cyclic voltammograms of the uncomplexed polymers are similar, exhibiting a wave due to n-doping in the region of $-2.2 \text{ V vs. Ag/Ag}^+$ (see Figure 1.12B) with accompanying electrochromism and no waves due to p-doping. Chemical n-doping of uncomplexed PPy with sodium naphthalide reportedly increased the dry conductivity from 10^{-14} S/cm to $1.6 \times 10^{-1} \text{ S/cm}$ [75].

PBpy was derivatized by refluxing in water with $\text{Ru}(\text{bpy})_2\text{Cl}_2$. The resulting water-insoluble material consisted of a methanol-extractable fraction with a MLCT band at *ca.* 450 nm and a site occupancy of approximately 20%, estimated from the UV-vis spectrum, while the remaining intractable and poorly characterized material only had approximately 1.4% site occupancy from elemental analysis data.

Depositing PBpy on a Pt electrode and subsequently reacting it with $\text{Ru}(\text{bpy})_2\text{Cl}_2$ resulted in a film containing 10–15% coordination estimated by XPS. This metallopolymer exhibits the intriguing cyclic voltammogram shown in Figure 1.12A. Compared to voltammogram of the monomer $\text{Ru}(\text{bpy})_3^{2+}$ in Figure 1.12C, it appears that ligand reduction waves have moved to less negative potentials, the Ru oxidation wave to less positive potentials, and there is an overall broadening into the wide unresolved charge envelope. The authors claim that this is a result of extensive charge delocalization and paradoxically describe this behaviour as being both “unique” and “characteristic of electrically conducting π -conjugated polymer ligands” [75] although the total dissimilarity between this voltammetric response and that of every other known conjugated metallopolymer tends to discredit the second claim. The lack of

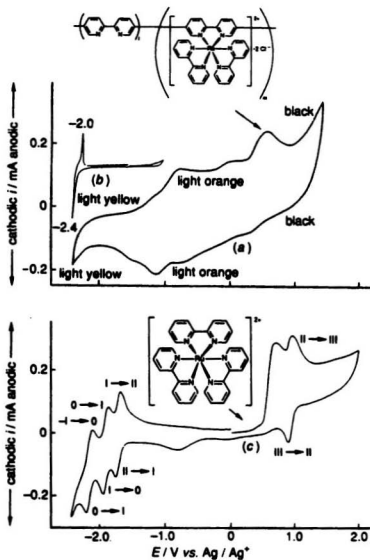


Figure 1.12: Cyclic voltammetry of (a) PBpy-Ru, (b) PBPy, and (c) Ru(bpy)₃²⁺ in acetonitrile solutions containing 0.1 M Bu₄NClO₄ [87]. Reprinted with permission from *J. Am. Chem. Soc.*, 1994, **116**, 4832. Copyright 1994 American Chemical Society

any statement of reproducibility or any comparisons between films of differing thickness (and the use of the same figure in at least two papers) certainly validates the first assertion, and the paucity of characterization data of the film in question suggests that the result must be viewed with skepticism. An alternate explanation [48] proposes that the low bpy site population leads to a wide range of polymer-based (from different chain lengths between metallated units) and metal-based (different distances to nearest neighbour) redox site environments.

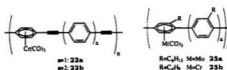
The voltammetry of Cu(I) complexes of 6,6'-dimethyl and 6,6'-dihexyl substituted PBpy [88] (having 74-99% site occupancy) display more conventional behaviour. A well-defined Cu(II/I) wave appears at 0.59 V *vs.* Ag⁺/Ag, although there is no attempt to explain the constant $\Delta E_p = 260$ mV over a wide range of sweep rates ($20 < \nu < 100$ mV/sec). A well-defined wave ($\Delta E_p = 90$ mV) also appears in the cathodic region at -1.84 V. Strangely, this was described as a Cu(I)/Cu(0) couple even though it occurs at potentials only slightly less negative than the polymer reduction. It was found from the cyclic voltammograms that approximately twice the amount of charge was passed in this wave than in the metal's oxidation wave, and the authors attribute this to an effect stemming from the better charge conductivity at low potentials (*i.e.*, n-doping). On the basis of the potential and the coulomb ratio, a more likely explanation is that the reduction is in fact due to bipyridines coordinated to Cu; the ratio of bpy to Cu in these complexes should be 2:1.

Electrocatalytic properties have been claimed [75,87] for the NiCl₂ complex of PBpy although the report is lacking in details. Redox waves similar to those in Ni(bpy)₂Br₂ were detected. Electrocatalytic reduction of CO₂ in CH₃CN was ostensibly observed at -2.15 V reaching a maximum coulombic efficiency (0.3 mol CO evolved per mol of electrons) at -2.40 V. There was however no mention of characterization of products (*e.g.*, by rotating ring-disc voltammetry or GC on the evolved gas),

no proposed mass balance (i.e., the fate of the second oxygen atom in the aprotic solvent), nor even details of any control experiments on similar films not containing Ni.

Complexes of PBpy were shown to have interesting photocatalytic properties towards the reduction of water to H_2 . Several metal species were introduced to the polymer in the presence of triethylamine as a sacrificial electron donor. The complex generated *in situ* by irradiation of $Pt(bpy)_2^{2+}$ (spectroscopically confirmed from the release of bpy and XPS measurements) proved to be the most active. The addition of RuO_2 as a co-catalyst improved the performance of the PBpy- $Ru(bpy)_2$ system in the absence of triethylamine, yet, strangely, the experiment was not repeated in the presence of a sacrificial donor.

1.4.1.6 Organometallic polyphenylenes



The synthesis of the η^6 organometallic polymers **22** and **23** have been reported [90, 91] and represent an interesting departure from the Werner type complexes that form the balance of this field. Thermogravimetric analysis of **22b** in air showed that it was stable to nearly 200°C. Other than a rudimentary conductivity study of **23**, no electrochemical data were presented. This sort of system leads to some intriguing catalyst possibilities, since the electrochemical oxidation or reduction of the 18-electron centre should lead to its destabilization and hence an enormous increase in the reactivity of the site. It might even be possible in this way to switch a supported chemical catalyst on and off by simple potential manipulations. In the present materials only

low molecular masses were observed (degree of polymerization was 10 to 17); these systems might be better thought of as oligomers.

1.5 Objectives

The goal of this project was quite straightforward: to test the hypothesis that the coordination of metal atoms to a conjugated polymer backbone will lead to an enhancement of the rate of electron transport compared to similar polymers not having the conjugation. The electron diffusion coefficient D_e was the parameter of interest since this gives a more reliable indication of the underlying processes than, say, conductivity.

Pyridine-benzimidazole based conjugated polymers were chosen as the support for the redox centres $\text{Ru}(\text{bpy})_2^{2+}$ and $\text{Os}(\text{bpy})_2^{2+}$. Polybenzimidazoles are an attractive choice for a number of reasons:

1. Polybenzimidazoles tend to be very robust [2], remaining stable under considerable thermal and chemical stress. In the harsh environment of an electrocatalytic system, chemical stability is crucial.
2. There exists an excellent bidentate site between the pyridine and imidazole nitrogens.
3. The second imidazole nitrogen has an acidic proton which may be removed and replaced, influencing the electron density along the polymer.
4. Several dinuclear complexes with a similar structure have been shown to possess notable coupling between the two metals.

$\text{Ru}(\text{bpy})_2^{2+}$ and $\text{Os}(\text{bpy})_2^{2+}$ are logical choices for metal centres with which to form complexes of these polymers because

1. They form stable low-spin d^6 complexes in the bipyridine-like environment.
2. The electrochemistry is well-behaved.
3. The non-conjugated redox polymers to which the results are compared are also based on these metal centres.

CHAPTER 2

EXPERIMENTAL

In this chapter the syntheses of the materials used in this project are detailed. The smaller molecules are categorized on the basis of whether or not they possess functionalities which could render them electrochemically polymerizable. The details of electrochemical and related experiments are presented separately in later chapters.

2.1 General Procedures and Instrumentation

Unless stated otherwise, all commercial chemicals and solvents were used as received without further purification. Reported yields are not optimized.

Nuclear magnetic resonance (NMR) spectra were acquired on a GE GN-300NB instrument at 300 MHz (^1H NMR). Where appropriate, chemical shifts are reported in ppm relative to $(\text{CH}_3)_4\text{Si}$ as an internal standard. Spectra acquired in deuterated trifluoroacetic acid (TFA-*d*), which had no internal standard, are referenced against the solvent peak at $\delta = 11.50$ ppm. In the spectra acquired in TFA-*d* with D_2O , the solvent signal did not appear at a predictable location; in these cases the absolute reported shifts are meaningless and only the relative positions of signals should be considered. In all cases individual peaks are reported as chemical shift, multiplicity (s=singlet, d=doublet, dd=doublet of doublets, t=triplet, q=quartet, m=multiplet), relative integrated intensity, and coupling constants.

Mass spectra (MS) were determined using a V.G. Micromass 7070HS spectrometer. Some of the more intense fragments are reported as m/z and percent relative intensity.

Elemental analyses were performed by Canadian Microanalytical Services, 207-8116 Alexander Road, RR #7, Delta, BC, V4G 1G7.

Spectroelectrochemistry was undertaken in a single beam spectrometer built in-house, consisting of a PRA-M303 lamp, Hamamatsu R374 photomultiplier tube with Keithley 427 current amplifier, and an ISA Instruments monochromator. Wavelength

and potential control, and output response readings were automated by means of a PC equipped with a Data Translations DT-2801 analogue-digital digital-analogue converter computer board and controlled by software written specifically for those experiments.

Cyclic voltammograms shown in this thesis were acquired with a Pine Instruments RDE-4 potentiostat in conjunction with a PC equipped with a Data Translations DT-2801 analogue-digital digital-analogue converter computer board, using custom software written by the author. Other cyclic voltammograms were obtained with a Hokuto-Denko HA301 potentiostat with HB104 function generator, or with a Solartron Schlumberger 1268 electrochemical interface controlled with custom software[92]. More sophisticated electrochemistry experiments are detailed in the appropriate sections. Unless stated otherwise, all potentials are *vs.* SSCE.

2.2 Starting Materials and Miscellaneous

2.2.0.1 Polyphosphoric Acid (PPA)

PPA is most conveniently used by generating it immediately prior to use. Approximately 25 mL is prepared by mixing 18 g P_2O_5 and 10 g 85% H_3PO_4 . The reagents are stirred at *ca.* 100 °C under a dry atmosphere until a homogeneous, clear viscous liquid has formed. Typically this takes around 24 h. The use of higher temperatures usually results in the discoloration of the PPA, although its efficacy appears unaffected in such cases. Additionally, owing to the high viscosity of the medium, all PPA reactions require mechanical stirring.

2.2.0.2 *cis*-Bis(2,2'-bipyridine-*N,N'*) dichlororuthenium(II) (24)

This preparation is based on the published method of Meyer and coworkers [93]. The dihydrate may be obtained by Taube's adaptations [94]. " $RuCl_3 \cdot xH_2O$ " (1.70 g,

8.22 mmol) and 2,2'-bipyridine (2.57 g, 16.4 mmol) were stirred in 50 mL DMF to which 2.0 g LiCl was subsequently added. The mixture was refluxed under N₂ for 5 h. The solvent volume was then reduced to ca. 10 mL under reduced pressure and diluted with 50 mL of acetone and allowed to stand at 0 °C overnight. The resulting black solid was collected by filtration, washed with H₂O until the rinsings were colourless and dried in air. The solid was redissolved in 250 mL of 50% aqueous ethanol by refluxing under N₂ for 1 h., 20 g of LiCl was added, and the solution volume was reduced to ca. 75 mL. Cooling overnight at 0 °C produced a dark solid which was collected, rinsed copiously with water, and dried *in vacuo* at r.t. giving **24** as a dark solid (1.58 g, 40%). The purity was verified by cyclic voltammetry ($E_{1/2}$ = 0.30₈ V *vs.* SSCE in CH₃CN containing 0.1 mol dm⁻³ Et₄NClO₄) and thin layer chromatography (methanol, R_f = 0.70). Elemental analysis: Calc'd for C₂₀H₁₆N₄Cl₂Ru·0.6H₂O: C 48.51%, H 3.50%, N 11.31%. Found C 48.49%, H 3.35%, N 11.26%.

2.2.0.3 2,2',2''-Terpyridyl trichlororuthenium(III) (**25**)

This follows Sullivan's preparation [95]. "RuCl₃·xH₂O" (263 mg, 1.00 mmol) and 2,2',2''-terpyridine (227 mg, 0.97 mmol) were stirred and refluxed in 125 mL of ethanol (freshly distilled over Mg/I₂) for 3 h. The contents were allowed to settle at r.t. overnight. The resulting dark solid was rinsed with abs. ethanol (3 × 10 mL) and then diethyl ether (3 × 10 mL). The residue was air dried to give **25** (398 mg, 93%) as a dark solid.

2.2.0.4 *cis*-Bis(2,2'-bipyridine-*N,N'*) dichloroosmium(II) (**26**)

This is based on the published procedure by Lay, Sargeson, and Taube [94]

2.2.0.4.1 *cis*-bis(2,2'-bipyridine-*N,N'*) dichloroosmium(III) chloride dihydrate K_2OsCl_6 (0.95 g, 2.0 mmol) and 2,2'-bipyridine (0.65 g, 4.2 mmol) were refluxed in 20 mL dimethyl formamide with stirring for 1 h. The dark solution was cooled to r.t., gravity filtered, and diluted, first with 10 mL of ethanol and then dropwise with 250 mL of diethyl ether with vigorous stirring. The resulting red solid was collected by filtration, rinsed sparingly with diethyl ether, and air dried overnight to give the product (1.20 g, 94%). $E_{1/2}$ (CH_3CN containing $0.1 \text{ mol dm}^{-3} Et_4NClO_4$) -0.04_5 V vs. SSCE.

2.2.0.4.2 *cis*-bis(2,2'-bipyridine-*N,N'*) dichloroosmium(II) dihydrate

The product of the preceding section (1.14 g, 1.77 mmol) was dissolved in a mixture of 23 mL of dimethyl formamide and 11.5 mL of methanol. A 1% w/w solution of sodium dithionite in water (225 mL, 13 mmol) was added dropwise with stirring. Following cooling in ice, a dark purple solid was collected by filtration, rinsed with water ($2 \times 10 \text{ mL}$), methanol ($2 \times 10 \text{ mL}$), and diethyl ether ($3 \times 10 \text{ mL}$), and air dried to give 0.45 g of product. More solid formed overnight from the mother liquor, and following the addition of more $Na_2S_2O_4$ (0.9 g, 5 mmol) and stirring, a further 0.12 g of product was isolated and rinsed as above. Total yield = 0.57 g (56%). $E_{1/2}$ (CH_3CN containing $0.1 \text{ mol dm}^{-3} Et_4NClO_4$) -0.04_1 V vs. SSCE. Elemental analysis: Calc'd for $C_{20}H_{16}N_4Cl_2Os \cdot 2H_2O$: C 39.41%, H 3.31%, N 9.19%. Found C 40.70%, H 2.54%, N 9.09%

2.3 Electropolymerizable Monomers

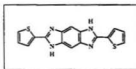
2.3.1 Thiophene-based Monomers

2.3.1.1 2-(2-Thienyl)-benzimidazole

**27**

A solution of 1,2-diaminobenzene (2.15 g, 19.9 mmol) and 2-thiophenecarboxylic acid (2.56 g, 20.0 mmol) in PPA (28 g) was stirred overnight under N_2 at 150 °C. The resulting dark viscous solution was poured into ca. 500 mL H_2O giving a black amorphous solid. This solid was collected by filtration and resuspended in 100 mL of methanol. This was filtered, and the filtrate was diluted with cold water, resulting in the formation of a fine white precipitate. This was collected, rinsed with water, and dried *in vacuo* at room temperature to give novel compound **27** as an off-white solid (0.9 g, 19%). MP 330–332 °C. 1H NMR (MeOH- d_4) δ 7.77 (dd, 1H), 7.63 (dd, 1H), 7.56 (dd, 1H), 7.23 (m, 4H). MS m/z (%) 200(M^{+} , 100), 167(6), 156(8), 155(5), 143(2), 129(3), 110(6), 109(5), 96(10). FTIR (KBr, cm^{-1}): 3418 (br), 2674 (br), 1622 (w), 1571 (m), 1451 (vs), 1425 (vs), 1314 (m), 1276 (s), 1235 (s), 944 (m), 852 (m), 743 (vs), 706 (vs).

2.3.1.2 2,2'-Bis(2-thienyl)-benzenediimidazole (attempted)

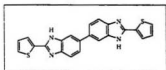
**28**

1,2,4,5-tetraminobenzene tetrahydrochloride (1.37 g, 4.8 mmol) and 2-thiophenecarboxylic acid (1.30 g, 10.1 mmol) were added to 14 g of PPA at ca. 80 °C. Following 8 h of stirring at 170 °C, the reaction mixture was poured into a large volume of water, yielding a quantity of black solid which was neutralized in a large volume of aqueous

Na_2CO_3 . Extraction of the black solid with methanol produced a red solution which, when concentrated and diluted with water, yielded an orange solid (0.20 g). MS indicated the desired compound was present (m/z 322) along with the corresponding monothienyl compound (m/z 230) and other unidentified contaminants (e.g., m/z 372). Attempts to purify chromatographically resulted in product decomposition and/or polymerization.

Similar results were obtained repeatedly despite variations of the experimental parameters, including the use of 5-bromo-2-thiophenecarboxylic acid which was prepared by literature methods [96,97]. An adaptation of Dotrong's thiazole method (see section 2.3.1.4) also failed, giving a black amorphous residue.

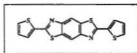
2.3.1.3 2,2'-Bis(2-thienyl)-6,6'-bibenzimidazole (attempted)



29

PPA (15 g) was prepared and degassed under vacuum. 3,3'-diaminobenzidine (0.54 g, 2.5 mmol) was added to the cold PPA under N_2 and warmed to 120 °C with stirring. The flask was evacuated and refilled with N_2 three times, and cooled to r.t. 2-Thiophenecarboxylic acid (0.65 g, 5.0 mmol) was added and the flask slowly warmed to 160–170 °C and stirred 24 h. Degassed H_2O (ca. 80 mL) was added, stirred several hours, and filtered to give a black paste and a red filtrate. Careful addition of solid NaOH to the filtrate until pH 5–6 produced 0.85 g of yellow solid. MS indicated it was a mixture of starting materials and the monothienyl intermediate. Extraction of the black solid with methanol yielded after evaporation ca. 10 mg of green solid which proved to be a complex mixture of materials that could not be resolved.

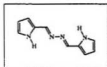
2.3.1.4 2,2'-Bis(2-thienyl)-benzodithiazole

**30**

This preparation follows Dotrong's method [10]. A mixture of trimethylsilylpolyposphate (9.13 g), 1,2-dichlorobenzene (30 mL), tributylamine (5 g), 2-thiophenecarboxylic acid (1.29 g, 10 mmol), and 2,5-diamino-1,4-benzenedithiodihydrochloride¹ (1.22 g, 5.0 mmol) were stirred under N₂ at 90°C for 20 h, at 130 °C a further 24, and finally at 150 °C for 2 h. The resulting suspension was cooled to r.t. and poured into *ca.* 250 mL methanol, giving a brown solid which was collected by filtration and rinsed thrice with small portions of methanol and dried. The crude solid was recrystallized from *N*-methylpyrrolidinone, and the resulting yellow crystals collected by filtration and washed with methanol, giving 0.79 g (44%) of **30** as fine yellow crystals. MP 310 °C (dec) ¹H NMR (TFA-*d*) δ 8.75 (s, 1H), 8.25 (d, 1H), 8.12 (s, 1H), 7.39 (t, 1H) MS *m/z* (%) 356(M⁺, 100), 247(9), 178(15), 138(6), 69(33). FTIR (KBr, cm⁻¹): 3414 (br), 1639 (br), 1548 (vs), 1486 (vs), 1419 (vs), 1400 (s), 1307 (s), 897 (s), 852 (vs), 828 (s).

2.3.2 Pyrrole-based Monomers

2.3.2.1 Pyrrolyl-2-aldazine

**31**

Pyrrole-2-carboxaldehyde (1.0 g, 10 mmol) and 85% hydrazine (1.5 mL, 50 mmol) were refluxed in 30 mL of ethanol for 24 h. The solvent was removed by rotary evaporation leaving a yellow oil. An orange solid formed following several days of

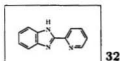
¹ provided *gratis* by Daychem Chemicals (Dayton, Ohio)

refrigeration. The solid was washed with cold water then cold diethyl ether, and recrystallized from ethanol to give **31** (0.29 g, 32%) as an orange solid. MP 168 °C (lit 190 °C [98]). ^1H NMR ($\text{DMSO}-d_6$) δ 11.56 (s, 1H), 8.39 (s, 1H), 6.99 (s, 1H), 6.61 (s, 1H), 6.19 (s, 1H) MS m/z (%) 186(M^+ , 100), 156(11), 120(5), 94(74), 93(73), 79(13), 66(33). FTIR (KBr, cm^{-1}): 3417 (br), 3226 (br), 1634 (vs), 1541 (m), 1409 (vs), 1132 (s), 1095 (m), 1028 (s), 954 (s), 880 (m), 812 (m).

2.4 Non-electropolymerizable Models

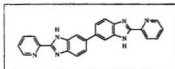
2.4.1 Pyridine Type Benzimidazoles

2.4.1.1 2-(2-Pyridyl)benzimidazole



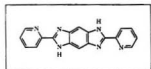
Picolinic acid (2.45 g, 20.0 mmol) and 1,2-diaminobenzene (2.15 g, 20.0 mmol) were added to 28 g PPA, and stirred under N_2 at 160 °C for 8 h. The resulting viscous solution was poured into 500 mL H_2O , producing a tan solid which was collected by suction filtration. The solid was then suspended in 500 mL of aqueous 0.5 M Na_2CO_3 , and filtered giving a pale yellow powder. Recrystallization from methanol/water yielded **32** (2.80 g, 72%) as a fine yellow solid. MP 219 °C (lit 218–220 °C [99]). ^1H NMR ($\text{TFA}-d$) δ 9.17 (d, 1H), 8.93 (d, 1H), 8.88 (t, 1H), 8.34 (t, 1H), 7.87 (m, 4H) MS m/z (%) 195(M^+ , 100), 167(12), 105(5), 90(6). FTIR (KBr, cm^{-1}): 3415 (br), 3058 (br), 1595 (m), 1468 (m), 1444 (vs), 1401 (vs), 1315 (vs), 1280 (vs), 1151 (m), 1123 (s), 994 (m), 972 (m).

2.4.1.2 2,2'-Bis(2-pyridyl)bibenzimidazole

**33**

Picolinic acid (2.46 g (20.0 mmol) and 3,3'-diaminobenzidine (2.14 g, 10.0 mmol) were added to 28 g PPA and stirred under N_2 at 175 °C for 7 h. The reaction mixture was then stirred vigorously in 700 mL H_2O for 1 h giving a yellow powder which was filtered, and washed with several mL of dilute aqueous $NaHCO_3$. The solid was recrystallized from methanol/water to give **33** (1.39 g, 36%) as a fine yellow powder. MP 232–235 °C (lit 230–233 °C [62]). 1H NMR (TFA- d) δ 9.27 (d, 1H), 9.07 (d, 1H), 8.96 (t, 1H), 8.44 (t, 1H), 8.36 (s, 1H), 8.23 (s, 2H) MS m/z (%) 388(M^+ , 100), 356(7), 345(5), 283(8), 194(24), 180(4). FTIR (KBr, cm^{-1}): 3419 (br), 3230 (br), 3055 (br), 1596 (vs), 1568 (s), 1447 (vs), 1402 (s), 1304 (m), 742 (s).

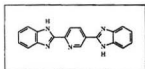
2.4.1.3 2,6-Bis(2-pyridyl)benzodiiimidazole

**34**

PPA (14 g) was degassed by stirring under vacuum at 120 °C for 18 h, and subsequently cooled to r.t. 1,2,4,5-Tetraminobenzene tetrahydrochloride (0.75 g, 2.6 mmol) was added and the temperature was slowly increased. The HCl gas released was flushed from the flask by a steady stream of N_2 . Removal of HCl was completed through repeated cycles of evacuating the flask and refilling it with N_2 . Picolinic acid (0.65 g, 5.2 mmol) was added, and the reaction was stirred under N_2 for 18 h at 120 °C and then 150 °C for a further 6 h. The reaction was then cooled to r.t. and diluted with 50 mL H_2O giving a brown solid which was collected by filtration. The solid was stirred in ca. 200 mL dilute aqueous $NaHCO_3$ and recrystallized twice from

1:1 methanol/water and once more from 4:1 methanol/water, giving **34** (0.40 g, 50%) as a yellow solid (which becomes red when exposed to gaseous HCl or aqueous acids). MP >345 °C (lit >280 °C [63]). ¹H NMR (TFA-*d*) δ 9.00 (d, 1H), 8.78 (d, 1H), 8.64 (t, 1H), 8.45 (s, 1H), 8.14 (t, 1H) MS *m/z* (%) 312(M⁺, 100), 286(3), 284(3), 207(6), 156(11), 105(13), 78(15). FTIR (KBr, cm⁻¹): 3432 (br), 3095 (br), 1592 (s), 1567 (m), 1452 (vs), 1404 (s), 1390 (m), 1278 (vs), 1238 (m), 1150 (w), 875 (m), 792 (m), 744 (m).

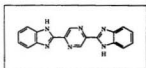
2.4.1.4 2,5-Bis(2-benzimidazolyl)pyridine



35

1,2-diaminobenzene (0.54 g, 5.0 mmol) was added to 32 g PPA at 120 °C under N₂. The temperature was raised to 175 °C and 2,5-pyridinedicarboxylic acid (0.43 g, 2.5 mmol) was added slowly over five days. When approximately one-half had been added, more P₂O₅ (1.4 g, 10 mmol) was added to compensate for the water of condensation. Following addition of all the diacid, the reaction was allowed to stir for a further two days. The PPA solution was then poured into 150 mL H₂O and stirred for 8 h, giving a fine tan solid which was collected by suction filtration and stirred overnight in 200 mL of 0.5 M aqueous NaOH, then filtered again to give a tan solid (0.91 g). This was recrystallized from methanol/water and dried *in vacuo* to give novel compound **35** (0.53 g, 68%) as a yellow powder. MP >310 °C. ¹H NMR (TFA-*d*) δ 9.73 (s, 1H), 9.01 (dd, 1H), 8.79 (d, 1H), 8.02 (m, 4H), 7.87 (m, 4H). MS *m/z* (%) 311(M⁺, 100), 283(4), 285(5), 194(14), 155.5(18). FTIR (KBr, cm⁻¹): 3377 (br), 3066 (w), 1602 (m), 1446 (s), 1432 (vs), 1313 (w), 1142 (m), 809 (w), 753 (s), 743 (s).

2.4.1.5 2,5-Bis(2-benzimidazolyl)pyrazine

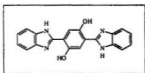
**36**

2.4.1.5.1 2,5-pyrazinedicarboxylic acid (37) KMnO_4 (8.6 g, 54 mmol), NaOH pellets (4.3 g, 0.11 mol), and 5-methyl-2-pyrazinecarboxylic acid (2.96 g, 21.4 mmol) were refluxed together in 250 mL H_2O overnight. Filtration, and acidification of the filtrate with conc. HCl gave a solid which was recrystallized from water and vacuum dried to give the desired diacid (1.30 g, 36%) as a pale orange solid.

2.4.1.5.2 2,5-bis(2-benzimidazolyl)pyrazine 2,5-pyrazinedicarboxylic acid (**37**, 0.52 g, 3.1 mmol) and 1,2-diaminobenzene (0.69 g, 6.4 mmol, recrystallized from benzene) were added to 14 g of PPA at r.t. The reaction was warmed to 115 °C under N_2 and stirred 24 h. P_2O_5 (1.7 g, 12 mmol) was added and the reaction was stirred at 140 °C for a further 72 h. Dilution of the resulting red PPA solution with 75 mL of water produced a quantity of green solid which was redissolved in 750 mL of 0.3 M NaOH and filtered. The filtrate was acidified with HCl , precipitating a yellow solid that was collected and dried *in vacuo* to give novel compound **36** (0.96 g, 96%) of as a fine yellow solid. MP > 320 °C. ^1H NMR ($\text{TFA}-d$) δ 9.89 (s, 2H), 7.96 (m, 4H), 7.80 (m, 4H) MS m/z (%) 312(M^+ , 100), 286(2), 284(3), 195(3), 169(18), 156(12), 142(14), 118(24). FTIR (KBr, cm^{-1}): 3358 (br), 3070 (w), 1623 (m), 1589 (m), 1555 (w), 1441 (s), 1430 (s), 1320 (vs), 1282 (vs), 1181 (s), 1143 (s), 890 (m,br), 768 (s), 753 (s), 743 (s).

2.4.2 Phenol-based Benzimidazoles

2.4.2.1 2,5-(2-Benzimidazolyl)-1,4-dihydroxybenzene

**38**

1,2-diaminobenzene (recrystallized from benzene, 0.76 g, 7.0 mmol) and 2,5-dihydroxy terephthalic acid (0.70 g, 3.5 mmol) were stirred together in 14 g PPA at 120 °C under N_2 for 24 h. 2 g of P_2O_5 was added and the reaction stirred at 140 °C for three days. The product was extracted in 600 mL H_2O giving a bright yellow solid which was purified by dissolution in aqueous NaOH and precipitation by acidifying to pH 7 with HCl, twice. The precipitate was collected by suction filtration, dried *in vacuo* at r.t. to give novel material **38** (0.81 g, 67%) as a fine yellow-orange powder MP > 320 °C. 1H NMR (TFA-*d*) δ 8.66 (s, 1H), 7.94 (s, 1H), 7.84 (m, 4H), 7.66 (m, 4H), 3.98 (s, 1H). MS m/z (%) 342 (M^{+} , 100), 285(29), 143(28), 65(10) FTIR (KBr, cm^{-1}): 3412 (br), 1624 (s), 1569 (s), 1507 (s), 1460 (m), 1454 (m), 1404 (m), 1313 (w), 1281 (s), 1148 (m), 1118 (m), 1092 (m), 875 (m,br), 750 (s), 740 (s).

2.4.3 Benzothiazoles

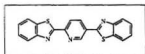
2.4.3.1 2-(2-Pyridyl)benzothiazole

**39**

Picolinic acid (0.66 g, 5.4 mmol) and 2-amino thiophenol (0.66 g, 5.3 mmol) were added together to PPA (18 g) at 120 °C. The reaction was stirred under N_2 for 20 h at 160 °C. The mixture was cooled, added to water (125 mL) and filtered to give a small quantity of solid (which was later determined to be comprised of a mixture of starting materials and product) and a yellow filtrate. The filtrate was neutralized slowly with

solid Na_2CO_3 and NaOH , resulting in the formation of a yellow precipitate. This was recrystallized from methanol to yield novel compound **39** (0.66 g, 60%) as a pale solid. MP 133–134 °C. ^1H NMR ($\text{TFA}-d$) δ 9.04 (d, 1H), 8.86 (dd, 1H), 8.64 (d, 1H), 8.28 (m, 2H), 8.18 (d, 1H), 7.80 (m, 2H). MS m/z (%) 212(M^+ , 100), 186(6), 185(3), 184(4), 108(15), 106(8), 78(10), 69(20) FTIR (KBr, cm^{-1}): 3421 (br), 3052 (m), 1585 (m), 1566 (m), 1510 (m), 1457 (s), 1434 (vs), 1317 (s), 996 (m), 980 (s), 783 (s), 760 (s), 740 (s).

2.4.3.2 2,5-Bis(2-benzothiazolyl)pyridine

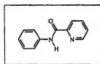


40

2-amino thiophenol (2.90 g, 23.2 mmol) and 2,5-pyridinedicarboxylic acid (1.80 g, 10.8 mmol) were stirred in PPA (28 g) under N_2 for 3 days at 163 °C. A further 6.1 g of P_2O_5 was added to the reaction during this time to compensate for water of condensation. The PPA solution was then poured into 400 mL H_2O , and the resulting yellow precipitate was collected, stirred in methanol and again in dilute aqueous NaOH during the course of which it became green. Crude yield ~100%. The green solid was recrystallized from ethylene glycol, yielding novel compound **40** (1.3 g, 35%) as shiny green plates. MP > 320 °C. ^1H NMR ($\text{TFA}-d$) δ 9.70 (d, 1H), 8.96 (dd, 1H), 8.70 (d, 1H), 8.36 (m, 4H), 8.03 (m, 4H). MS m/z (%) 345 (M^+ , 100), 319(6), 236(3), 211(22), 172.5(11), 108(14). FTIR (KBr, cm^{-1}) 3413 (br), 1619 (m), 1516 (m), 1454 (s), 1432 (vs), 1389 (m), 1313 (s), 1255 (m), 1013 (s), 967 (vs)

2.4.4 Other

2.4.4.1 *N*-phenyl-2-carboxamide



41

This preparation is considerably simpler than the one reported in the literature [100]. Aniline (distilled over Zn, 4.69 g, 50 mmol) was added to PPA (56 g) at 120 °C and stirred under N₂ for 1 h. Picolinic acid (6.20 g, 50 mmol) and P₂O₅ (6.9 g) were added and the reaction was stirred for 24 h under N₂ at 140 °C. The reaction was diluted with water and extracted with CHCl₃. The organic layer was washed with saturated aqueous NaHCO₃ solution and then with water, and then subjected to rotary evaporation to give a yellow solid. This solid was recrystallized from CHCl₃/low b.p. pet. ether to give **41** (4.22 g, 44%) as pale yellow fine needles. MP 75 °C (lit 76 °C) [100] MS *m/z* (%) 198(M⁺, 40), 169(4), 106(9), 79(100), 78(70). ¹H NMR (TFA-*d*) δ 8.95 (d, 1H), 8.80 (d, 2H), 8.26 (dd, 1H), 7.43 (d, 2H), 7.36 (t, 2H), 7.28 (d, 1H). FTIR (KBr, cm⁻¹): 1670 (vs), 1602 (s), 1529 (vs), 1466 (m), 1447 (s), 1431 (s), 1321 (m), 1236 (m), 1126 (m), 1044 (s), 1147 (w), 988 (s), 903 (s), 894 (m), 815 (s).

2.5 Model Complexes

Caution! Perchlorates are potentially explosive! While no detonation tendencies were observed in the following materials, appropriate care should be exercised.

2.5.1 Ruthenium Complexes

2.5.1.1 Dinuclear bisbipyridyl ruthenium complex of 2,2'-bis(2-pyridyl)-bibenzimidazole (**42**)

$\text{Ru}(\text{bpy})_2\text{Cl}_2 \cdot 2\text{H}_2\text{O}$ (0.0973 g, 0.187 mmol) and **33** (0.0397 g, 0.102 mmol) were dispersed in glycerol (50 mL) and gently refluxed for 24 h. The mixture was then diluted with an equal volume of water and filtered. The addition of a few mL of saturated aqueous NaClO_4 to the filtrate resulted in the formation of a red precipitate which was collected and dried *in vacuo* to give **42** (0.1408 g, 93%) as a red solid.

A methanol solution of **42** eluted as a single band on a Sephadex LH-20 column. Elemental analysis: Calc'd for $\text{C}_{64}\text{H}_{48}\text{N}_{14}\text{O}_{16}\text{Cl}_4\text{Ru}_2 \cdot 0.4\text{H}_2\text{O}$: C 47.44%, H 3.04%, N 12.10%. Found C 47.89%, H 3.48%, N 11.64%.

2.5.1.2 Bisbipyridyl ruthenium complex of 2,5-bis(2-benzimidazolyl)pyridine (**43**)

$\text{Ru}(\text{bpy})_2\text{Cl}_2 \cdot 2\text{H}_2\text{O}$ (0.0572 g, 0.109 mmol) and **35** (0.0292 g, 0.0938 mmol) were stirred in gently refluxing glycerol (50 mL) for 24 h. The red solution was diluted with H_2O (50 mL) and filtered. The addition of a few mL of saturated aqueous NaClO_4 to the filtrate precipitated novel complex **43** (0.0954 g, 100%) as a red solid.

A methanol solution of **43** eluted as a single band on a Sephadex LH-20 column. Elemental analysis: Calc'd for $\text{C}_{39}\text{H}_{29}\text{N}_9\text{O}_8\text{Cl}_2\text{Ru} \cdot 4.3\text{H}_2\text{O}$: C 46.79%, H 3.79%, N 12.59%. Found C 47.51%, H 3.58%, N 11.84%.

2.5.1.3 Bisbipyridyl ruthenium complex of *N*-phenyl-2-carboxamide (**44**)

$\text{Ru}(\text{bpy})_2\text{Cl}_2 \cdot 2\text{H}_2\text{O}$ (0.0556 g, 0.107 mmol) and **41** (0.0205 g, 0.106 mmol) were dissolved in hot H_2O , gravity filtered, and allowed to stand overnight. A few drops of saturated aqueous NaClO_4 were added to the filtrate, leading to the formation of well defined crystals over the course of several days. These were collected and air

dried, giving novel compound **44** (0.0382 g, 46%) as dark red crystals. Large crystals could be grown from a methanol solution slowly diluted by absorption of water in a humid atmosphere. However, a crystal structure could not be obtained owing to twinning. Elemental analysis: Calc'd for $C_{32}H_{26}N_6O_9Cl_2Ru \cdot H_2O$: C 46.44%, H 3.29%, N 10.15%. Found C 46.45%, H 3.37%, N 10.14%.

2.5.1.4 Bisbipyridyl ruthenium complex of pyrrolyl-2-aldazine (**45**)

$Ru(bpy)_2Cl_2 \cdot 2H_2O$ (0.1460 g, 0.280 mmol) and **31** (0.0227 g, 0.149 mmol) were refluxed in a 2:1 ethanol water mixture (60 mL) for 48 h. The solvent was removed by rotary evaporation and the resulting residue was redissolved in a minimal volume (ca. 4 mL) of MeOH and loaded on a 12" Sephadex LH-20 column with methanol as the mobile phase. The desired novel dinuclear complex eluted first as a dark green band, followed by a red band.

The two fractions were evaporated, redissolved in water, and subsequently precipitated by the addition of a large excess of $NaClO_4$. The red species was formed in a quantity insufficient for isolation.

Elemental analysis: Calc'd for $C_{50}H_{40}N_{12}O_8Cl_2Ru_2 \cdot 5.5H_2O$: C 45.81%, H 3.94%, N 12.82%. Found C 45.72%, H 3.25%, N 12.93%.

2.5.1.5 Dinuclear bisbipyridyl ruthenium complex of 2,5-(2-benzimidazolyl)-1,4-dihydroxybenzene (**46**)

$Ru(bpy)_2Cl_2 \cdot 2H_2O$ (0.2658 g, 0.510 mmol) and **38** (0.0930 g, 0.272 mmol) were stirred together in 50% aqueous methanol (60 mL) at r.t. for three days then refluxed for one day, and filtered. Rotary evaporation of the filtrate produced a dark red solid which was stirred in ethanol (50 mL) and filtered. The filtrate's volume was reduced by rotary evaporation. Addition of water and a large excess of solid $NaClO_4$ produced

a dark solid which was suction filtered and air dried, yielding novel compound **46** (0.1674 g, 42%).

A solution of **46** in methanol eluted on a Sephadex LH-20 column in a single purple band. Elemental analysis: Calc'd for $C_{60}H_{46}N_{12}O_{18}Cl_4Ru_2$: C 45.99%, H 2.96%, N 10.73%. Found C 46.39%, H 3.10%, N 10.60%.

2.5.1.6 Dinuclear bisbipyridyl ruthenium complex of 2,5-bis(2-benzimidazolyl)pyrazine (**47**)

$Ru(bpy)_2Cl_2 \cdot 2H_2O$ (0.1908 g, 0.366 mmol) and **36** (0.0566 g, 0.181 mmol) were refluxed in DMA (50 mL) three days. The volume was reduced by rotary evaporation to ca. 10 mL and then diluted with H_2O (100 mL) and filtered. A large excess of $NaClO_4$ was added to the filtrate and the resulting green solid was collected by filtration.

The mononuclear and dinuclear compounds were separated on a Sephadex LH-20 column using 1:1 methanol/acetonitrile as eluant, with the dinuclear complex eluting first as a green band and the mononuclear compound as a red band. The overlap between the bands was returned to the column and further separated. The sequence was repeated until the two compounds were well resolved. The purified novel dinuclear complex **47** was obtained (0.0396 g, 14%) as a dark green solid. Elemental analysis: Calc'd for $C_{58}H_{44}N_{14}O_{16}Cl_4Ru_2$: C 45.32%, H 2.89%, N 12.76%. Found C 47.33%, H 3.68%, N 11.32%.

2.5.1.7 Terpyridylchloro ruthenium(II) complex of 2,5-bis(2-benzimidazolyl)pyridine (**48**)

$Ru(trpy)Cl_3$ (0.0600 g, 0.136 mmol) and **35** (0.0415 g, 0.133 mmol) were refluxed in ethylene glycol (30 mL) for 20 h. The reaction solution was diluted with H_2O (150 mL) and filtered. The addition of a large excess of $NaCl$ (4 g) to the filtrate produced a red solid which was collected, rinsed with H_2O (3×10 mL) and Et_2O (2×10 mL) and

air dried. Purification by silica column chromatography with acetone as the mobile phase gave novel compound **48** (0.0907 g, 85%) as a dark solid. Elemental analysis: Calc'd for $C_{34}H_{24}N_8Cl_2Ru \cdot 3.5H_2O$: C 52.58%, H 4.01%, N 14.37%. Found C 54.10%, H 3.50%, N 12.57%

Replacement of the chloro ligand with aquo is accomplished by refluxing **48** in 3:1 acetone:H₂O and filtering. Adding excess NaClO₄ to the filtrate gives the novel terpyridylquo complex **49** as a dark solid.

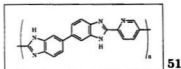
2.5.2 Osmium Complexes

2.5.2.1 Dinuclear bisbipyridyl osmium(II) complex of 2,5-bis(2-benzimidazolyl)pyrazine (**50**)

Os(bpy)₂Cl₂ (0.130 g, 0.227 mmol) and **36** (0.0317 g, 0.101 mmol) were stirred and refluxed in DMA (50 mL) for four days. Following cooling to r.t., the reaction was diluted with H₂O (200 mL) and filtered. A dark precipitate formed following the addition of a large excess of solid NaClO₄. This crude product was dissolved in 3:1 mixture Britton-Robinson buffer (pH=5):MeCN and loaded on a Sephadex C50 cation exchange column. Elution with this solvent produced a very pale yellow solution. The desired novel green dinuclear complex **50** was eluted with 3:1 buffer (pH=6.9):MeCN. The mononuclear complex was eluted as a red band with the same solvent combination containing an additional 0.5 M in NaCl. The purity of each complex was verified by cyclic voltammetry.

2.6 Polymers

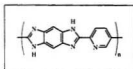
2.6.0.1 Poly([6,6'-bibenzimidazole-2,2'-diyl]-2,5-pyridine): PPyBBIM



51

3,3'-Diaminobenzidine (1.03 g, 4.8 mmol) and 2,5-pyridinedicarboxylic acid (0.82 g, 4.9 mmol) were added to PPA (14 g) and stirred under N_2 for 6 h at 120 °C. P_2O_5 (5 g) was added to the red viscous solution and the stirring was continued for 24 h at 125 °C and 43 h at 160 °C. The reaction was cooled to r.t., diluted with water (ca. 75 mL) and filtered. The resulting orange polymer was resuspended in a large volume of stirring water and filtered, three times. The amorphous orange solid which resulted was dried for 72 h *in vacuo* at 90 °C, yielding novel polymer **51** (1.44 g, 77%). Elemental analysis: Calc'd for $C_{19}H_{11}N_5 \cdot 4.5H_2O$: C 58.45%, H 5.16%, N 17.94%, O 18.44%. Found C 58.33%, H 4.11%, N 17.48%, O 18.24%. Trace P was detected by electron microprobe analysis. C/N (by atoms): Calc'd 3.80 for $C_{19}H_{11}N_5$. Found 3.89. The low found %H suggests that some of the oxygen accounted for by water in the proposed formula is actually present as a phosphorus containing species (*e.g.*, H_3PO_4) and $-CO_2H$ end groups. FTIR (KBr, cm^{-1}): 3410 (br), 3177 (br), 1629 (s), 1598 (s), 1442 (vs), 1302 (s), 1248 (m), 1227 (m), 1131 (m, br), 852 (m), 805 (s).

2.6.0.2 Poly([1,7-dihydrobenzo(1,2-*d*:4,5-*d'*) bisimidazole-2,6-diyl]-2,5-pyridine) (PPyBDIM)

**52**

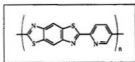
Recrystallization of tetraminobenzene tetrahydrochloride (TAB-4 HCl), based on the published method by Jenekhe's [11]: A 10% (w/w) aqueous HCl solution was prepared (50 g) and deoxygenated with a stream of argon gas. Crude TAB-4 HCl (2.0 g), a purple solid, was added along with activated charcoal (0.8 g). The mixture was stirred under Ar for ten min, and filtered under a blanket of Ar. The clear colourless filtrate was collected and was treated with concentrated HCl (20 g). The solution was cooled in ice under Ar, giving a fine white crystalline precipitate which was collected by

gravity filtration, dried *in vacuo* at r.t. overnight, giving the purified reagent (1.6 g, 80%).

PPA (30 g) was prepared and thoroughly degassed by repeated evacuations and flushes with N_2 . Recrystallized TAB-4HCl (0.690 g, 2.43 mmol) was added at r.t., and the flask was slowly warmed to 100 °C in a N_2 stream. HCl gas removal was completed by repeated cycles of evacuations and flushes. 2,5-Pyridinedicarboxylic acid (0.414 g, 2.48 mmol) was added and the reaction mixture was stirred under N_2 at 100 °C for 48 h. The temperature was raised to 120 °C, P_2O_5 (1.4 g, 10 mmol) was added, and the reaction was stirred for 48 h, and finally for 24 h at 143 °C.

The polymer was extracted from PPA by stirring the reaction mixture in H_2O (900 mL) for 24 h, giving an orange solid which was collected by filtration and re-suspended in 0.2 M NaOH (900 mL), stirred 3 days and filtered. The orange solid was finally resuspended in H_2O (900 mL) for 48 h, filtered and dried *in vacuo* to give novel compound **52** (0.562 g, 74%) as a dark grey solid with a metallic luster. Elemental analysis: Calc'd for $C_{13}H_7N_5 \cdot 4.5H_2O$: C 49.68%, H 5.10%, N 22.29%. Found C 50.51%, H 4.21%, N 21.78%. C/N (by atoms): Calc'd 2.60, found 2.70. FTIR (KBr, cm^{-1}): 3388 (br), 3172 (br), 1641 (m), 1597 (s), 1454 (vs), 1385 (s), 1352 (s), 1284 (s), 1240 (m,br), 1052 (m), 843 (s).

2.6.0.3 Poly([benzo(1,2-*d*:4,5-*d'*)bisthiazole-2,6-diyl]-2,5-pyridine) (PPyBDT)

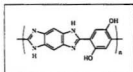


53

2,5-Diamino-1,4-benzenedithiodihydrochloride (0.77 g, 3.1 mmol) was added to PPA (56 g) at r.t. The mixture was gently warmed to 130 °C under a stream of N_2 to effect dehydrochlorination which was completed through repeated cycles of evacuating the

flask and flushing it with N_2 . While raising the temperature to 145 °C over 5 h, 2,5-pyridinedicarboxylic acid (0.53 g, 3.1 mmol) was added slowly, followed by P_2O_5 (1.8 g, 13 mmol). The reaction was allowed to proceed at 165 °C for 60 h and finally at 190 °C for 11 h. The PPA solution was cooled to r.t. and the polymer extracted in H_2O (1 L). The resulting polymer was collected and washed further by being suspended first in 0.02 M NaOH then water for several days in a large volume of each. The solid was collected by filtration, dried *in vacuo* at r.t. to give the novel polymer as a dark grey powder (0.62 g, 68%). Elemental analysis: Calc'd for $C_{13}H_5N_3S_2 \cdot 1.7H_2O$: C 52.40%, H 2.84%, N 14.10%. Found C 52.28%, H 2.64%, N 14.11. C/N (by atoms): Calc'd 4.33, found 4.32.

2.6.0.4 poly([1,7-dihydrobenzo(1,2-*d*:4,5-*d'*) bisimidazole-2,6-diyl]-2,5-[1,4-dihydroxyphenylene]) (PHyBDIM)



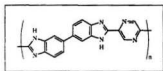
54

Recrystallized TAB-4HCl (0.69 g, 2.4 mmol, see §2.6.0.2) was added to PPA (14 g) at r.t. The mixture was gently warmed to 105 °C under a stream of N_2 and stirred for 24 h. Residual HCl was removed by successive evacuation/ N_2 flush cycles. 2,5-Dihydroxyterephthalic acid (0.48 g, 2.4 mmol) was added, and the reaction was stirred for 24 h at 100 °C under a N_2 atmosphere. P_2O_5 (1.6 g, 11 mmol) was added and the reaction stirred at 120 °C for another 24 h, and at 140 °C for 24 h further, after which time the reaction had become so viscous that it had rolled itself into a red ball around the stirrer. Stirring the mixture in water (750 mL) for 4 days led to the extraction of the polymer in thin red sheets and rubbery clumps which were subsequently minced with a metal propeller-type stirrer. The morphology of a small sample of the polymer was seen to undergo distinct changes on the basis of pH;

suspended in a fairly concentrated NaOH solution, it forms fluffy brown particles, and in the presence of aqueous, HCl it returns to the red sheet form.

The extracted polymer was stirred in 0.7 M NaOH (1 L) for 24 h, during which time it turned dark green-brown, and finally in a large volume of H₂O for two days, giving **54** (0.70 g, 74%) as shiny, fluffy, rubbery purple solid after vacuum drying. The polymer is insoluble in wet TFA, preventing the acquisition of a NMR spectrum. Elemental analysis: Calc'd for C₁₄H₈N₄O₂·1.3H₃PO₄: C 42.94%, H 3.06%, N 14.31%. Found C 43.30%, H 2.96%, N 14.06%. C/N (by atoms): Calc'd 3.50 for C₁₄H₈N₄O₂. Found 3.59.

2.6.0.5 Poly([6,6'-bibenzimidazole-2,2'-diyl]-2,5-pyrazine): PPzBBIM

**55**

3,3'-Diaminobenzidine (recr. 2× from H₂O, 1.65 g, 7.7 mmol) and 2,5-pyrazinedicarboxylic acid (1.30 g, 7.7 mmol) were added together to PPA (27 g) at r.t. The reaction was stirred under N₂ at 95 °C for 24 h, and 112 °C for 60 h. P₂O₅ (4.0 g, 28 mmol) was added and the reaction allowed to proceed a further 16 h at 150 °C.

The dark red PPA solution was cooled to r.t. and stirred in water (1 L) giving a red solid which was collected by suction filtration. The solid was resuspended and stirred in water for a day three more times. Drying *in vacuo* gave 2.6 g (76%) of the novel polymer as a dark green brittle solid. Elemental analysis: Calc'd for C₁₈H₁₀N₆·7.25H₂O: C 49.03%, H 5.60%, N 19.06%. Found C 49.08%, H 4.19%, N 19.03%. C/N (by atoms): Calc'd 3.00 for C₁₈H₁₀N₆. Found 3.01. FTIR (KBr, cm⁻¹): 3417 (br), 1628 (vs), 1578 (m), 1518 (s), 1443 (s), 1312 (s), 1170 (s), 897 (m,br), 806 (s).

2.7 Polymer Complexes

Caution! Perchlorates are potentially explosive! While no detonation tendencies were observed in the following materials, appropriate care should be exercised.

2.7.1 Ruthenium Complexes

2.7.1.1 Bisbipyridyl ruthenium(II) complex of **51**: Ru-PPyBBIM (**56**)

$\text{Ru}(\text{bpy})_2\text{Cl}_2 \cdot 2\text{H}_2\text{O}$ (0.0499 g, 0.096 mmol) and **51** (0.0319 g, 0.082 mmol-site) were refluxed together in glycerol (50 mL) for 24 h. The solution was cooled to r.t., diluted with 50 mL H_2O , and filtered. To the dark orange filtrate was added several mL of saturated aqueous NaClO_4 solution. A dark precipitate slowly formed. This was collected by filtration, rinsed with water, and air dried at r.t. to give novel material **56** (0.0550 g, 73%) as a fine dark red-brown solid. Elemental analysis: Calc'd for $\text{C}_{19}\text{H}_{11}\text{N}_5(\text{C}_{20}\text{H}_{16}\text{N}_4\text{Cl}_2\text{O}_8\text{Ru})_{0.85} \cdot 5.25\text{H}_2\text{O}$: C 46.78%, H 3.83%, N 12.73%, Cl 6.52%, Ru 9.29%. Found C 47.48%, H 3.10%, N 11.99%, Cl 6.53%, Ru 7.26%

2.7.1.2 Bisbipyridyl ruthenium(II) complex of **52**: Ru-PPyBDIM (**57**)

$\text{Ru}(\text{bpy})_2\text{Cl}_2 \cdot 2\text{H}_2\text{O}$ (0.0899 g, 0.173 mmol) and **52** (0.0390 g, 0.127 mmol-site) were refluxed for four days in glycerol (50 mL) under N_2 . Dilution with two volumes of water, filtration, and addition of a large excess of saturated aqueous NaClO_4 solution to the filtrate produced a red solid which was resuspended in water (ca. 20 mL) and stirred overnight. The solid was collected by filtration and washed with water then diethyl ether and air dried to give novel complex **57** (0.124 g, 100% yield) as a fine red-brown solid. Elemental analysis: Calc'd for $\text{C}_{33}\text{H}_{23}\text{N}_9\text{O}_8\text{Cl}_2\text{Ru} \cdot (\text{H}_2\text{O})(\text{C}_3\text{H}_8\text{O}_3)$: C 45.24%, H 3.48%, N 13.19%. Found: C 45.16%, H 3.12%, N 13.23%

2.7.1.3 Bis(bipyridyl) ruthenium(II) complex of **55**: Ru-PPzBBIM (**58**)

Ru(bpy)₂Cl₂·2H₂O (0.0980 mg, 0.188 mmol) and **55** (0.0308 g, 0.070 mmol-site) were refluxed in glycerol (50 mL) for three days. The resulting red liquid was cooled to r.t., filtered (leaving no residue), diluted with H₂O (200 mL), and filtered again. Addition of a large excess of sat'd aqueous NaClO₄ solution precipitated novel material **58** as a green solid which was filtered off, rinsed copiously with water and air dried to give **58** (0.130 g, 108%), a dark green solid. This compound is green in the presence of excess ClO₄⁻, red in the presence of OH⁻. The colour and the extra mass of the product suggest it may have been contaminated with residual NaClO₄. Since this condition would have no adverse effect on the electrochemistry, no further purification steps were taken. Elemental analysis: Calc'd for C₁₈H₁₀N₆(C₂₀H₁₆N₄Cl₂O₈Ru)_{1.95}·(H₂O)(C₃H₈O₃)₂: C 44.34%, H 3.50%, N 11.33%. Found C 44.51%, H 3.18%, N 11.24%.

A similar polymer complex with lower Ru content was prepared analogously, with only one equivalent of Ru(bpy)₂Cl₂·2H₂O having been used.

2.7.1.4 Bis(bipyridyl) ruthenium(II) complex of **54** (attempted)

All attempts to synthesize this complex failed. The approaches included:

- reaction in glycerol (reflux)
- reaction in glycerol with 5% H₂O (reflux)
- reaction in glycerol with 5% H₂O and base (tetrabutylammonium hydroxide) (reflux)
- reaction in glycerol with polymer precipitated from methanesulphonic acid (reflux)

- reaction in nitromethane (reflux and r.t.)
- reaction in nitromethane with base (tributyl amine) (reflux and r.t.)
- reaction in dimethyl formamide (reflux and r.t.)
- reaction in dimethyl acetamide (reflux and r.t.)

2.7.1.5 Terpyridylchloro ruthenium complex of **51** (attempted)

$\text{Ru}(\text{trpy})_3\text{Cl}_3$ (0.187 g, 0.425 mmol) and **51** (0.125 g, 0.404 mmol-site) were suspended in a 75% solution of glycerol in water (50 mL). LiCl (0.5 g) and triethylamine (1 mL) were added. The reaction was stirred and refluxed gently for 6 days, producing an opaque brown liquid. Filtration yielded a dark solid and a red filtrate which did not give a precipitate when treated with an excess of solid NaClO_4 . The dark solid was rinsed with H_2O , diethyl ether, and air dried giving a final mass of 0.276 g. The dark solid was insoluble in all solvents tried, including the mixed solvent systems in which other polymer complexes were soluble.

2.7.2 Osmium Complexes

2.7.2.1 Bisbipyridyl osmium(II) complex of **51**: Os-PPyBBIM (**59**)

$\text{Os}(\text{bpy})_2\text{Cl}_2$ (0.118 g, 0.207 mmol) and **51** (0.061 g, 0.157 mmol-site) were refluxed together in glycerol (50 mL) for six days. The resulting dark solution was filtered and diluted with H_2O (ca. 300 mL). A large excess of solid NaClO_4 was added, and the resulting red precipitate was collected by filtration. It was resuspended and stirred in a large volume of water overnight, and filtered again, giving novel polymer complex **59** (0.148 g, 90%) as a fine black powder. Elemental analysis: Calc'd for $\text{C}_{19}\text{H}_{11}\text{N}_5(\text{C}_{20}\text{H}_{16}\text{N}_4\text{Cl}_2\text{O}_8\text{Os}) \cdot 2\text{H}_2\text{O}$: C 44.75%, H 2.98%, N 12.04%, Cl 6.77%. Found C 45.26%, H 3.21%, N 11.01% Cl 6.16%.

2.7.2.2 Bisbipyridyl osmium(II) complex of **55**: Os-PPzBBIM (**60**)

Os(bpy)₂Cl₂ (0.045 g, 0.079 mmol) and **55** (0.011 g, 0.025 mmol-site) were refluxed in glycerol (25 mL) under N₂ for four days. Dilution of the resulting dark solution with two volumes of water, filtering, and addition of excess solid NaClO₄ to the filtrate produced dark green-brown solid which was collected and resuspended in H₂O (*ca.* 20 mL) and stirred overnight. The resulting black solid was collected by filtration, rinsed with water then ether, and air dried to give novel compound **60** (39.8 mg, 80%) as a fine black solid. Elemental analysis: Calc'd for C₁₈H₁₀N₆(C₂₀H₁₆N₄Cl₂O₈Os)_{1.95}·3.4C₃H₈O₃: C 40.53%, H 3.46%, N 9.71%. Found C 40.95%, H 3.12%, N 9.31%.

CHAPTER 3

SYNTHESIS AND CHARACTERIZATION OF UNCOMPLEXED POLYMERS

3.1 Thiophene-based Polymers

3.1.1 Attempted Synthesis

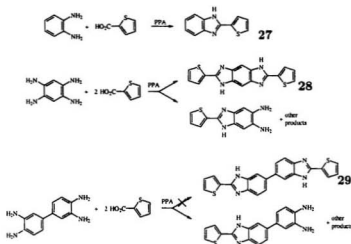
The development of electrochemically generated polymers is an area of research which has been the focus of a great deal of attention over the past fifteen years, with much of this having been devoted to polythiophene and its derivatives [26,101–105]. The option of grafting the polymer directly to the electrode surface is an attractive one for a number of reasons. Polymers grown through anodic polymerization have been shown to possess excellent conductivity. The *in situ* growth of the polymer has the additional advantages of allowing for the facile regulation of thickness and surface coverage by controlling charge passed, and the preclusion of difficulties of processing polymers with near-zero solubility.

Interest has been directed towards the fine tuning of the polymers' electronic properties by the synthesis of substituted thiophene monomers or the production of copolymers involving various conjugated spacers [106]. The latter was potentially of interest in this project in that the coordination compounds of such "spaced" thiophenes could introduce a new dimension of control over the electronic nature of the monomer, and consequently of the polymer.

To this end the three novel benzimidazole-type thiophene monomers presented in Scheme 3.1 were targeted, one as a model and two intended for electropolymerization.

The diamine-acid condensation in PPA used predominantly in this project failed to produce the desired products. Invariably, the reaction yielded an amorphous black solid which, when precipitated from the PPA dope, would not redissolve. The black solid was likely some polymerized thiophene byproduct. Pyrolysis GC-MS¹ of the solid from one experiment indicated fragments suggesting that benzimidazole, thiophene-benzimidazole, and bithiophene were present in the black solid. Four-point probe

¹The assistance of Dr. Robert Helleur is gratefully acknowledged



Scheme 3.1: Target thiophene-benzimidazole monomers and byproducts

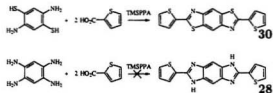
measurements on compressed pellets of this byproduct recorded very low conductivities, on the order of $10^{-6} \text{ S}\cdot\text{cm}^{-1}$, suggesting that this material is not highly conjugated.

It was possible to extract some materials from the black solid with methanol. In the case of **27**, the desired compound was isolated, although in very low yields. In the best cases involving reactions intended to form **28**, a small quantity of yellow solid was extracted from the black material. MS indicated that the desired compound was present (m/z 322), along with the intermediate monothieryl product indicated in Scheme 3.1 (m/z 230) and other unidentified materials (*e.g.*, m/z 372). Attempts to purify this material by column chromatography resulted in immediate decomposition, leaving only a black residue at the top of the silica column. Attempts to use the impure material in electrochemical experiments were also unsuccessful, with no polymer film resulting on the electrode surface. There was no evidence of the desired product in

materials extracted from the residue of the reactions leading to bibenzimidazole **29**; only the “halfway” monothienyl product was observed.

Variations of the experimental conditions did not bring about any improvements. Protecting the 5-position on the starting material 2-thiophene carboxylic acid with bromine made no difference.

In the synthesis of a related compound, 2,6-bis(2-thienyl)benzo(1,2-d:4,5-d')bis-thiazole (**30**), Dotrong *et al.* used an alternate approach involving trimethylsilylphosphite, tributyl amine, and *o*-dichlorobenzene [10]. The chemical synthesis of the corresponding polymers however employed the standard PPA method. Although it is not explained in the paper, it appears that the motivation behind this alternate method is the inhibition of thiophene radical formation in order to prevent spontaneous polymerization. This experiment was successfully duplicated, however its adaptation to the preparation of **28** was unsuccessful; once again only the intractable black solid was obtained. Clearly the benzimidazole analogue is much more reactive than the benzothiazole. *Ab initio* calculations on these monomers, performed at the HF/6-31G* level on geometries optimized with the STO-3G basis set are presented in table 3.1. The results indicate the HOMO energy of the imidazole compound is considerably higher and therefore this compound should be more easily oxidized than the thiazole. This implies that the generation of radical cations is more favourable for the



Scheme 3.2: Dotrong's method

CORE	HOMO (eV)	LUMO (eV)
IMIDAZOLE (28)	-6.47	0.75
THIAZOLE (30)	-7.81	1.47

Table 3.1: HF/6-31G**/HF/STO-3G HOMO and LUMO energies of **28** and **30**

imidazole compound, giving support to the claim that spontaneous polymerization in the reaction vessel had taken place.

Attempts to polymerize **30** electrochemically were unsuccessful.

3.2 Condensation Polymers

3.2.1 Synthesis

The polyphosphoric acid condensation polymerization was outlined in section 1.1. The two *o*-diamine type monomers used for the polymers studied in this project were 1,2,4,5-tetraminobenzene tetrahydrochloride and 3,3'-diaminobenzidine. In general, owing to their air sensitivity, the amine reagents used in this type of reaction are often not used directly in the synthesis; rather, the hydrochloride salts are used and/or the reaction must be performed in an inert atmosphere. When a hydrochloride is used, the polymerization stage must be preceded by a dehydrochlorination step whereby the amine hydrochloride is slowly warmed to *ca.* 100°C in PPA in a stream of N₂ and finally under reduced pressure. Care must be taken to avoid foaming. The use of an inert atmosphere holds the further advantage of excluding atmospheric water which is detrimental to PPA's effectiveness.

Addition of a stoichiometric quantity of the diacid follows, and it was found that rapid or slow addition made no apparent difference. A partial implementation of Wolfe's P₂O₅ adjustment method [12] was employed to account for the change in PPA composition from the water released in the condensation reaction, and thereby maintain the efficacy of the PPA.

Polymer	C/N (atoms)	
	calc	found
PPyBBIM	3.80	3.89
PPyBDIM	2.60	2.69
PPyBDIM	2.60	3.37
PPyBDT	4.33	4.32
PHyBDIM	3.50	3.59
PPzBBIM	3.00	3.01

Table 3.2: Relative carbon and nitrogen content in polymers as determined by elemental analysis. The second **PPyBDIM** results is included to illustrate the worst result obtained with this polymer.

3.2.2 Elemental Analysis

Elemental analyses (sections 2.6.0.1 through 2.6.0.5) were in good accordance with the proposed structures with between 1.7 and 7 water molecules per repeat unit. The high water content is consistent with the hygroscopic nature of polybenzimidazoles. Poly(1,3-phenylenebiphenylbenzimidazole), for instance, absorbs around 15% w/w water in a 100% relative humidity atmosphere [107].

The C:N atom ratio (table 3.2) provides a good measure of the quality of the polymer sample. High C:N ratios were obtained in early syntheses, as demonstrated by the second **PPyBDIM** entry in the table. This high carbon content may be ascribed to disproportionate contributions by carboxyl termini and splitting of the polymer chain by failed closure of the imidazole rings.

Excellent agreement between calculated and experimental C/N ratios is seen for **PPyBDT** and **PPzBBIM**, while **PPyBBIM**, **PPyBDIM**, and **PHyBDIM** give reasonable results.

3.2.3 IR Spectroscopy

Infrared spectra of the polymers (as KBr pellets) share several important features with their corresponding model compounds. A few representative spectra are shown

33	34	35	PPyBBIM	PPyBDIM	36	PPeBBIM	38	PHyBDIM
3419	3432	3377	3410	3388	3358	3417	3412	3436
3230	3095		3177	3172				
3055		3066			3070			
		1602	1629	1641	1623	1628	1624	1624
1596	1592		1598	1597	1589	1578		
1568	1567				1555		1569	1550
						1518	1507	
1447	1452	1446	1442	1454	1441	1443	1460	1452
		1432			1430		1454	1445
1402	1404						1404	
	1390			1385				1387
				1352				
1304		1313	1302		1320	1312	1313	
	1278			1284	1282		1281	
	1238		1248	1240				1257
			1227					1205
								1195
					1181	1170		1177
	1150	1142	1131		1143		1148	
							1118	
				1052			1092	1108
								1012
	875				890	897	875	
			852	843				
	792	809	805			806		788
					768			
		753			753		750	
742	744	743			743		740	

Table 3.3: Selected IR frequencies in cm^{-1} for polymers and model compounds

in Figures 3.1 through 3.3, while others may be found in appendix A.2. Selected frequencies are tabulated in table 3.3. Broad features appear in the $3000\text{--}3500\text{ cm}^{-1}$ region indicating that the imidazole N-H proton is hydrogen bonding either to water molecules or to neighbouring imine functionalities in a manner typical of benzimidazoles in the solid state. All compounds show bands in the $1625\text{--}1592\text{ cm}^{-1}$ and $1454\text{--}1441\text{ cm}^{-1}$ regions characteristic of benzimidazoles [108–110]. The shift of the

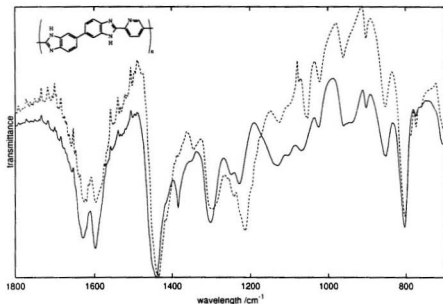


Figure 3.1: Comparative infrared spectra of two **PPyBBIM** samples (KBr)

1454 cm^{-1} band in **38** to 1445 cm^{-1} in **PHyBDIM** is typical of protonated imidazoles [110], suggesting (i) that the polymer is protonated and therefore contains H_3PO_4 , a condition that is consistent with the elemental analysis data (see §2.6.0.4), and (ii) that there is inter- or intrachain hydrogen bonding between the imidazole and hydroxyl group. Interchain hydrogen bonding could account for this polymer's insolubility in everything other than strong acid.

IR spectroscopy is also useful for verifying the consistency of polymer synthesis. As shown in Figure 3.1, very similar spectra were obtained for samples of **PPyBBIM** synthesized under different conditions; the dashed line is the spectrum of **PPyBBIM** synthesized under more dilute conditions (the peak at 1384 cm^{-1} is a spurious signal due either to spectrometer malfunction or to KBr contamination).

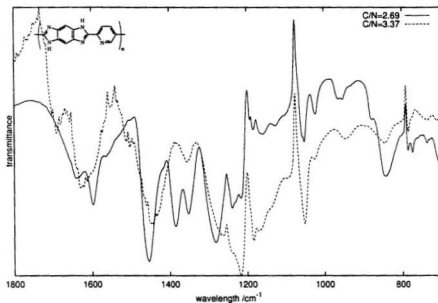


Figure 3.2: Comparative infrared spectra of two **PPyBDIM** samples (KBr)

Consequently, in conjunction with elemental analysis, IR spectra can provide evidence of the presence of structural defects in the polymers. For example, in Figure 3.2 the IR spectra of the products of two **PPyBDIM** syntheses are overlaid. The dashed line is for a polymer whose C/N ratio was very high— 3.37 vs. the predicted value of 2.60, while the solid line is for a sample whose C/N ratio is 2.69. Significant differences are seen, not least of which is the broadening of bands, which is indicative of a highly defective polymer. Furthermore, the band near 1690 cm⁻¹ implies the presence of unexpected carbonyl functionalities.

During the workup of the polymers by water extraction, it was occasionally observed that two forms of the polymer were present; **PPyBBIM** for example produced both orange and purple solids. Samples of each type were physically isolated and examined separately by IR spectroscopy. The spectra are overlaid in Figure 3.3. Apart

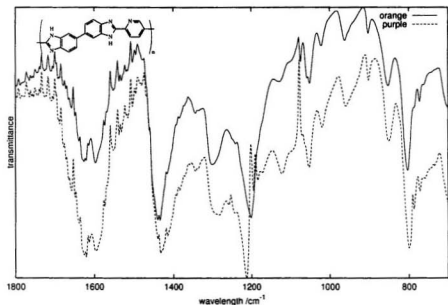


Figure 3.3: Comparative infrared spectra of orange (solid line) and purple (dashed line) PPyBBIM isolated during the water extraction stage (KBr)

from some slight peak shifts and some added detail in the N-H stretch region the spectra are essentially the same. This demonstrates that the apparent physical difference between the forms should be ascribed to phenomena such as packing, protonation, water content, or interactions between chains rather than to some gross structural defect. This claim is supported by the observation that the purple form gradually becomes orange if it is suspended in a large volume of water for several days.

3.2.4 NMR Spectroscopy

Jenekhe has reported [8, 9, 11, 111, 112] reversible donor-acceptor interactions between a number of polybenzobisazole polymers and Lewis acids such as AlCl_3 . This permits dissolution of the polymers in certain organic solvents, typically nitromethane, and

allows for the subsequent processing of otherwise insoluble polymers and their analysis by NMR. The polymers prepared in this project were also found to be soluble to varying degrees by this method.

The solubility of the polymers in strong acids also permits the acquisition of reasonable NMR spectra in CF_3COOD (TFA-*d*). Interestingly, the polymers were found to dissolve only in wet TFA; as a consequence, the addition of a small quantity (<5% v/v) of D_2O was required. This effected a shift in the solvent's residual proton signal, $\delta = 11.50$ for pure TFA-*d*, upfield by several ppm to some new position which varied from sample to sample. In the absence of an internal standard, the absolute shifts reported in the spectra are not informative. The relative positions of the peaks are however useful for comparison against spectra of model compounds. The use of TFA-*d* for NMR has the advantage of simplicity over Jenekhe's method. The AlCl_3 (or other Lewis acid) must be carefully purified by sublimation, and the nitromethane solutions must be prepared in a dry box. The polymer solutions must be kept rigorously free of water in order to preclude the formation of aluminum hydroxides which add spurious signals to the NMR spectra. In the case of these benzimidazole polymers, it was found that the aluminum hydroxide signals overlapped with the polymers', rendering the spectra considerably more difficult, if not impossible, to interpret.

It was sometimes found that the polymers, particularly the rigid-rod variety, were not very soluble in the wet TFA medium. **PHyBDIM** was completely insoluble. The low solubility presents a potential problem, since oligomers and low weight polymers would tend to dissolve preferentially. This then implies that the NMR spectrum might not be completely representative of the bulk sample and any perceived impurities, particularly chain termini, might be exaggerated as a result.

Figure 3.4 presents NMR spectra in TFA of **PPyBBIM** and the indicated model compound **33**. The expected disappearance of the proton at the model's pyridine 5

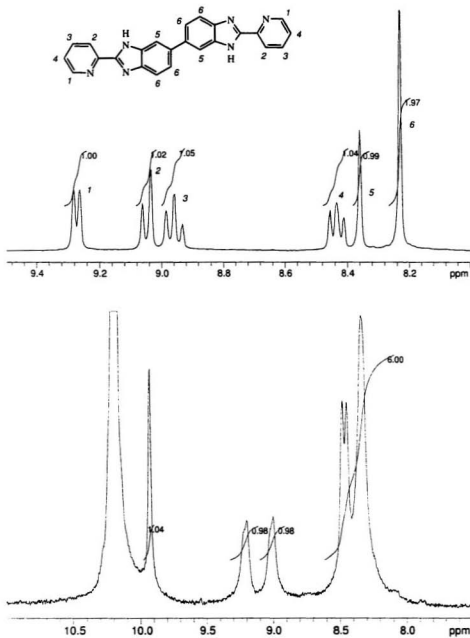


Figure 3.4: ^1H NMR spectra of model compound **33** (top) in TFA- d and PPyBBIM (bottom) in TFA- d + D_2O (the peak near $\delta=10.2$ ppm is solvent)

position (signal #4) as well as the halving of the remaining pyridine signals relative to the benzene is observed. The absence of other signals indicates that this polymer is of a high quality with few defects.

3.2.5 UV-Vis Spectroscopy

The optical properties of the five polymers and several model compounds are summarized in table 3.4, and overlaid spectra of the polybenzimidazoles are shown in Figure 3.5. The model compounds give information on the functionalized benzimidazole as an isolated chromophore, and comparison with the polymers illustrates the influence of extended conjugation on their electronic structure. The optical bandgaps E_g in table 3.4 were estimated from the onset of the $\pi \rightarrow \pi^*$ band. Since it is often difficult to determine this point, the error in E_g is no less than ± 0.1 eV. λ_{max} and E_g values of similar benzimidazoles in the literature [11] are found at somewhat longer wavelengths, but this is due to those spectra having been taken as thin films; it has been shown [8] that absorptions often become red-shifted in solid state optical spectra.

	DMA		MSA		ϵ (L mol ⁻¹ cm ⁻¹)
	λ_{max} (nm)	E_g (eV)	λ_{max} (nm)	E_g (eV)	
PPyBBIM	401	2.6	427	2.3	3.7×10^4
PPyBDIM	—	—	419	2.3	3.9×10^4
PPyBDT	433	2.4	414	2.3	
PHyBDIM	—	—	433	2.3	
PPzBBIM	424	2.3	415	2.2	
32	312		327		3.6×10^4
33	343		356		
34	360		346		
35	355		379		
38	336		344		
36	376		375		

Table 3.4: Summary of polymer and model optical properties in dimethyl acetamide and in methane sulphonic acid

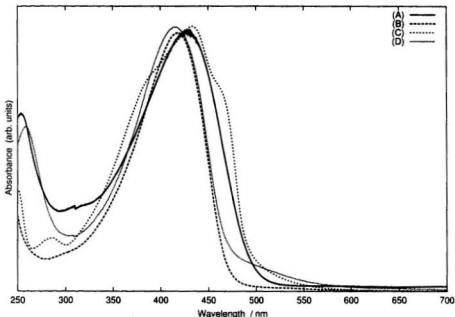


Figure 3.5: Normalized UV-vis spectra of (A) **PPyBBIM**, (B) **PPyBDIM**, (C) **PHyBDIM**, and (D) **PPzBBIM** in methanesulphonic acid

In conjunction with the data in table 3.4, the spectra in Figure 3.5 suggest that there is little difference in the electronic band structures of the four imidazole polymers **PPyBBIM**, **PPyBDIM**, **PHyBDIM**, and **PPzBBIM**. The $\pi \rightarrow \pi^*$ transition gives λ_{max} ranging between 415 and 427 nm in MSA. **PHyBDIM** is slightly unusual in that its $\pi \rightarrow \pi^*$ peak is complicated by several shoulders. Similar features are seen in the spectra of model compounds **38** and **36**, but not **35** (Figure 3.6). In DMA, all model compounds exhibit shoulders on the large central absorption. Of the polymers, only **PPzBBIM** and **PHyBDIM** exhibited this behaviour in both solvents. Comparable benzimidazole polymers in the literature [11] have similar shoulders in their spectra although no explanation was offered.

The extensive delocalization of the π electrons in the polymers is reflected in the

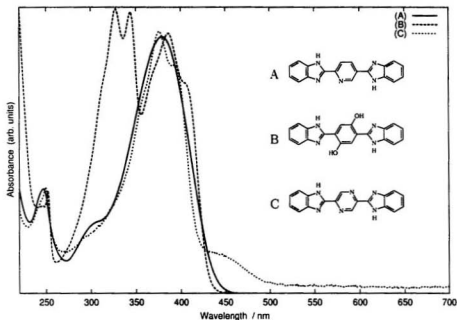


Figure 3.6: Normalized UV-vis spectra of model compounds (A) **35**, (B) **38**, and (C) **36** in methanesulphonic acid

shift of the $\pi \rightarrow \pi^*$ transition to longer wavelengths compared to the model compounds (*cf.* Figure 3.5 with Figures 3.6 and 3.7) in a manner typical of conjugated systems [113]. The similarity of λ_{max} and E_g between the rigid rod (**PPyBDIM**, **PPyBDT**, and **PHyBDIM**) and the biphenyl-type (**PPyBBIM** and **PPzBBIM**) polymers suggests that any contribution from the added rotational freedom through the biphenyl link to non-coplanarity is negligible. This observation apparently contradicts Jenekhe's claim [11] based on the spectra of related benzimidazole polymers having a non-rigid divinylene link. In that case however the polymers were examined as free-standing films, not in solution, and this presumably has significant consequences in both macroscopic and molecular terms.

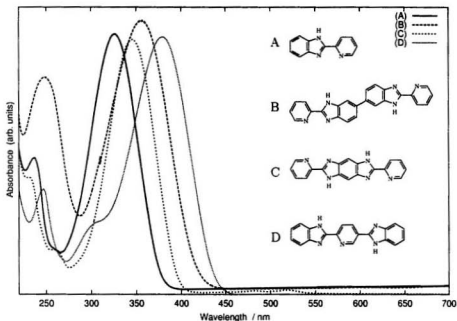
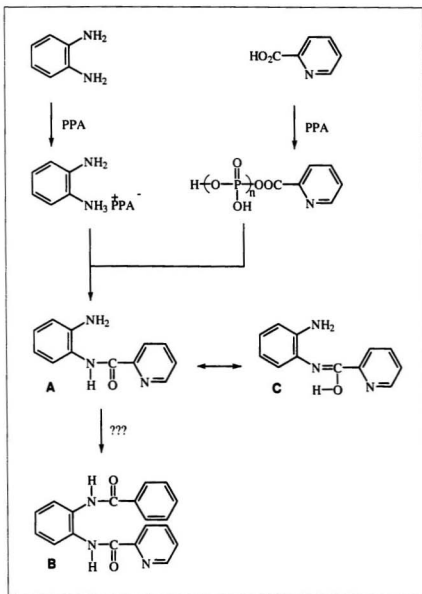


Figure 3.7: Normalized UV-vis spectra of model compounds (A) **32**, (B) **33**, (C) **34** and (D) **35** in methanesulphonic acid

3.3 Local Defects: Incomplete Ring Closure

Incomplete ring closure, as outlined in Scheme 3.3 can lead to defects and splits in the polymer chain. The reaction between two acids and one diamine could lead to a branched structure (structure B) with a relative carbon content higher than the target cyclized product. Evidence of incomplete ring closure and/or branching is seen in the infrared spectra of some polymers, where an unexpected carbonyl signal appears near 1690 cm^{-1} (see Figure 3.2).

An important ramification of incomplete ring closure is that it leads to a disruption in the conjugation. While this condition is clearly undesirable, there exists the possibility of an amide-imide tautomerization giving structure C in Scheme 3.3.



Scheme 3.3: Proposed structures resulting from polymer splitting and tautomerization

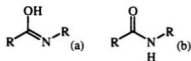


Figure 3.8: Model tautomers (a) imide and (b) amide

The formation of the imide tautomer provides a link through which long-range conjugation could return. A similar process is thought to occur in polythiophenes deactivated by the nucleophilic addition of OH at the 3-position [114]. Unfortunately, the equilibrium ratio of imide to amide is generally very small, $K \sim 8 \times 10^{-9}$ for formamide [115, 116]. It is reasonable that the extended conjugation in the polymers could act as a driving force towards the imide tautomer. This possibility was explored in a separate *ab initio* computational study [117], the results of which are combined with some new additional calculations and summarized below.

3.3.1 *Ab initio* Modeling of the Structural Defect

A series of models was constructed with varying lengths of straight conjugated chain containing n carbon atoms on each side of a core comprising the imide or the amide isomer (Figure 3.8). Straight chains were chosen to avoid added steric complications. Two representative optimized structures are shown in Figure 3.9. All calculations were performed with the software package Gaussian 94 [118], with geometries optimized at the HF/3-21G level of theory [119]. The following criteria were considered:

- HOMO-LUMO gap: The decrease of this energy difference with increasing conjugation length is well known [120] and this trend should be reflected in changes in the relative HOMO-LUMO gap energies of the tautomers as the side chains interact through the core.

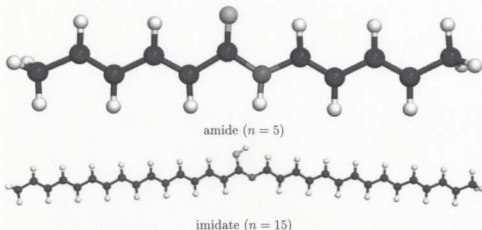


Figure 3.9: HF/3-21G optimized structures of two models

- Relative energies: The energies of the amide and imidate isomers will be compared. Any stabilization of the imidate core by pendant conjugated chains should be indicated by a drop in this tautomer's energy relative to its amide analogue.

3.3.1.1 HOMO-LUMO gap

The difference in HF/6-31G*//HF/3-21G energies of the last occupied and first virtual orbitals are tabulated in table 3.5. The difference between the values $\Delta\Delta E$ is

Chain Length (# of C atoms)	Imidate ΔE (eV)	Amide ΔE (eV)	$\Delta\Delta E$ (eV)
1	15.971	16.064	0.094
3	11.372	11.784	0.412
5	9.713	9.997	0.283
8	8.456	8.524	0.068
9	8.422	8.487	0.064
10	8.150	8.155	0.005
15	7.781	7.711	-0.070

Table 3.5: LUMO-HOMO energy gap for a series of amide and imidate models, and the difference between them

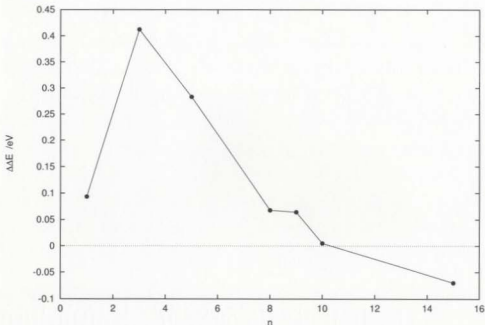


Figure 3.10: LUMO-HOMO energy gap of the amide tautomer compared to the imide, for a variety of chain lengths

also indicated and plotted as a function of side chain length n in Figure 3.10. An interesting trend is evident. Not surprisingly, the HOMO-LUMO gap is larger initially for the amide tautomer since the imide double bond explicitly permits the conjugation continuity through the core segment. The difference in gaps decreases with increasing n , and surprisingly the amide's gap becomes smaller than the imide's when $n \sim 10$. These results clearly suggest that the amide form does allow the two conjugated chains to interact, and in fact appears to do so more effectively than the imide. This might be explained by the partial double bond character between the C and N that is present in all amides becoming more prevalent in the longer chain models.

3.3.1.2 Tautomer relative energies

The energy of the imidate isomer with respect to the amide is plotted in Figure 3.11 for six calculation methods. In all cases a relatively large drop is seen when the first conjugated segment is added (i.e., between $n = 1$ and $n = 3$), indicating the partial stabilization of the imidate form. Additional conjugation results in a further drop in the relative energy for Hartree-Fock methods, although the drop is very slight. The B3LYP density functional post Hartree-Fock energies indicate a similar trend. The most credible results are given by the B3LYP/6-31G**//HF/6-31G* series of calculations, where the presence of conjugated sidechains leads to a relative stabilization of the imidate form by around 10 kJ/mol. This modest improvement is small compared

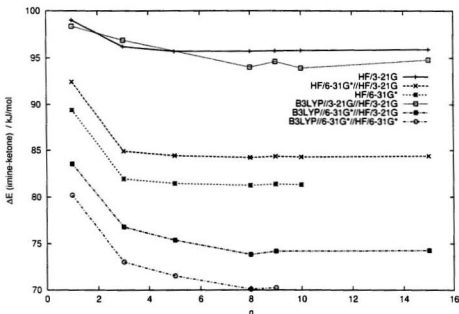


Figure 3.11: Energy difference between the imidate and amide tautomers as a function of chain length, at different levels of theory

to the absolute energy difference between the tautomers, which is on the order of 80 kJ/mol in favour of the amide isomer. These results imply that nearby conjugation leads to a slight stabilization of the imidate tautomer, although the amide form will still dominate.

3.3.1.3 Calculation conclusions

The relative molecular energies of the tautomers suggests that a minor stabilization of the imidate form over the amide form does take place when long conjugated chains are associated with the core component. The most sophisticated calculations here suggest that this stabilization is on the order of 10 kJ/mol which is small compared to the overall energy difference between the tautomers; the amide will continue to be the dominant form. Nonetheless, it appears that there might be good communication between the conjugated sidechains through the non-conjugated amide core, and therefore the presence of defects in the real polymers might not be exceedingly detrimental to their electrochemical properties. Further study of this phenomenon is warranted, and could include a comparison of the properties of a benzimidazole polymer and a deliberately-split polyamide.

3.4 Electrochemistry

3.4.1 Film Preparation

Polymer films suitable for electrochemical study may be cast onto Pt disc electrodes from solutions of the polymer either in MSA or DMA. Preparation from DMA solutions is straightforward as a drop placed on the electrode will slowly lose solvent by evaporation leaving behind a thin film. This method proved unsuitable for the rigid rod polymers owing to their limited solubility in this medium; MSA was used instead. MSA solutions require slow precipitation of the polymer by the careful dissolution of

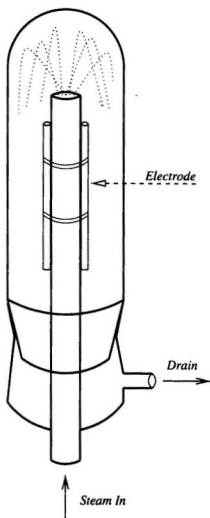


Figure 3.12: The Electrode Sauna

the acid in water. The most effective means by which this could be accomplished was found to be the "electrode sauna" pictured in Figure 3.12. This apparatus, which is simply an inverted cold trap, allows the slow dilution of the acid in the humid atmosphere provided by steam. Best results were obtained when the polymer film was subsequently allowed to soak overnight in a solution of electrolyte, permitting the influx of solvent and ions. Failure to do this, and allowing the polymer film to dry out, frequently resulted in a film which was electrically insulating.

Attempts to cast films from other solutions *e.g.*, $\text{MeNO}_2 + \text{AlCl}_3$ proved to be unsatisfactory.

3.4.2 Cyclic Voltammetry

The cyclic voltammetry of thin films of the polymers is characterized by broad irreversible oxidation and reduction waves whose positions and current magnitude are influenced by the pH of the electrolyte solution.

Figure 3.13 shows cyclic voltammograms of a thin film of **PPyBBIM**, cast from DMA, on a Pt disc electrode with 0.1 M Et_4NClO_4 in MeCN as the electrolyte. A broad, poorly defined oxidation wave is evident in the region between 1.0 and 1.4 V *vs.* SSCE. The magnitude of the oxidation current decreases slightly with successive sweeps possibly as a result of deactivation or degradation of the π backbone.

Increasing the sweep width for the same film gives a cyclic voltammogram as shown in Figure 3.14. A reduction is seen at $E_p = -1.65$ V and the oxidation wave has shifted to a lower potential, 1.15 V. From the onset of these waves, near -1.4 V and 0.9 V respectively, the bandgap may be estimated at 2.3 eV. This agrees well with the optical bandgap listed in table 3.4. Note that the oxidation wave's current in Figure 3.14 is significantly larger than in Figure 3.13.

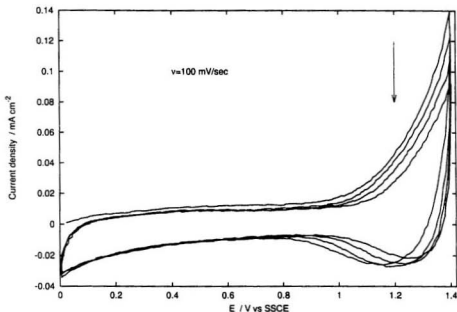


Figure 3.13: Cyclic voltammetry of a thin film of **PPyBBIM** on a Pt disc electrode in CH_3CN containing $0.1 \text{ mol dm}^{-3} \text{Et}_4\text{NClO}_4$ showing oxidation and degradation.

It turns out that the oxidation wave's potential is variable, or at least can be convoluted by another oxidation, the source of which is not certain, but is likely to be connected to the reduction and oxidation of the water trapped inside the film. The electroactivity of trace water in thiophene polymers has been reported previously [76]. The H^+ and OH^- produced in this process will be free to interact with the polymer film as can the parent H_2O . Dietz and Beck [121] have produced strong evidence that water leads to the deactivation of polyacetylene via the nucleophilic attack mechanism outlined in Scheme 3.4. Similar findings have been reported for polypyrrole [122] and polythiophene [114].

Cyclic voltammetry of another film of **PPyBBIM** is shown in Figure 3.15. The

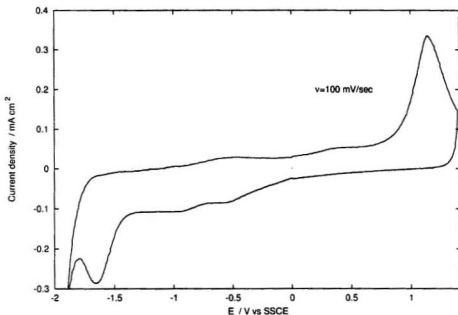
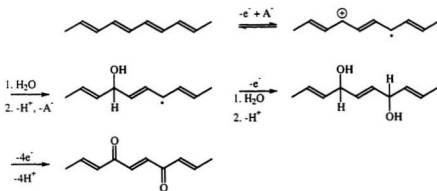


Figure 3.14: Cyclic voltammetry of a thin film of **PPyBBIM** in CH_3CN containing $0.1 \text{ mol dm}^{-3} \text{ Et}_4\text{NClO}_4$ over a wider sweep width.



Scheme 3.4: Mechanism of polymer deactivation by nucleophilic attack by water

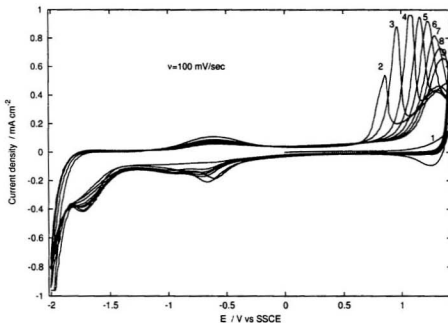


Figure 3.15: Evidence of **PPyBBIM** degradation by cyclic voltammetry in CH_3CN containing $0.1 \text{ mol dm}^{-3} \text{Et}_4\text{NClO}_4$.

movement of the anodic wave is quite clear, moving to increasingly positive potentials with successive sweeps. This behaviour is only evident after cycles through the reduction waves at negative potentials (*cf.* Figure 3.13). The migration of the wave is an indication of degradation of the backbone, and brings into consideration the influence of hydroxide generated at negative potentials. In addition to its role in the rate of polymer deactivation, the pH of the electrolyte solution is particularly relevant to the electrochemical response of the polymer complexes, and this will be explored in later chapters. The uncomplexed polymers also exhibit electrochemical behaviour strongly influenced by the nature of the electrolyte solution.

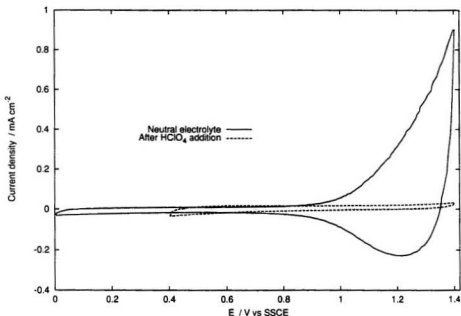


Figure 3.16: Cyclic voltammetry of a thin film of **PPyBBIM** in CH_3CN containing $0.1 \text{ mol dm}^{-3} \text{ Et}_4\text{NClO}_4$, before (solid line) and after (dashed line) the addition of HClO_4 . $\nu=100 \text{ mV/sec}$

PPyBBIM exhibits clearly distinct responses in acidic and basic media. Figure 3.16 shows the effect of adding a few drops of concentrated HClO_4 on the cyclic voltammetry of a thin film of **PPyBBIM** on a Pt disc electrode in CH_3CN containing $0.1 \text{ mol dm}^{-3} \text{ Et}_4\text{NClO}_4$. Following addition of the acid, the oxidation wave current drops to near zero. Figure 3.17 shows the corresponding influence of adding a few drops of base (MeOH containing $1 \text{ mol dm}^{-3} \text{ Bu}_4\text{NOH}$) on the polymer's cyclic voltammetry. In this case, the oxidation current becomes significantly augmented on the first sweep following addition of base, but rapidly degrades to zero on successive sweeps. Additionally, the cathodic current seen in neutral electrolyte vanishes. These results indicate that:

1. The electron density and conductivity of the backbone can be influenced by the degree of the polymer's protonation. This is of course a function of the composition of the electrolyte solution to which the polymer is exposed.
2. Degradation of the polymer backbone is accelerated in the presence of base, presumably either through a mechanism by which the oxidized regions of the backbone are attacked nucleophilically by hydroxide anions directly, or through the acceleration of the process outlined in Scheme 3.4. This in turn gives some support to the claim that the behaviour seen in Figure 3.15 stems from hydroxide generated from the reduction of interstitial water during exposure to negative potentials only.

The other polymers exhibit similar behaviour. For completeness, cyclic voltammograms of thin films of **PHyBDIM** and **PPzBBIM** are presented in Figures 3.18 and 3.19 respectively.

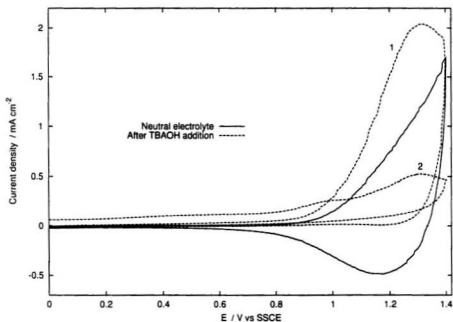


Figure 3.17: Cyclic voltammetry of a thin film of **PPyBBIM** in CH_3CN containing $0.1 \text{ mol dm}^{-3} \text{ Et}_4\text{NClO}_4$, before (solid line) and after (dashed line) the addition of Bu_4NOH . $\nu = 100 \text{ mV/sec}$

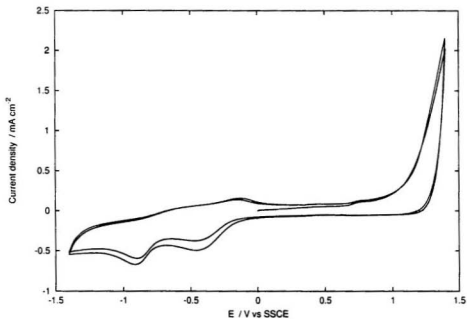


Figure 3.18: Cyclic voltammetry of a thin film of **PHyBDIM** in CH_3CN containing $0.1 \text{ mol dm}^{-3} \text{ Et}_4\text{NClO}_4$. $\nu=100 \text{ mV/sec}$

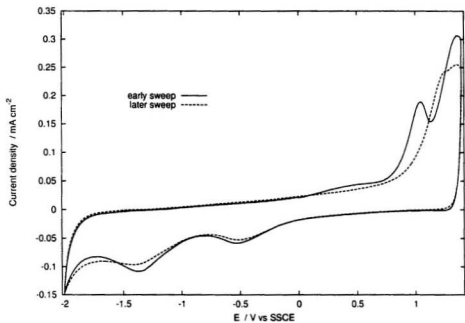


Figure 3.19: Cyclic voltammetry of a thin film of **PPzBBIM** in CH_3CN containing $0.1 \text{ mol dm}^{-3} \text{ Et}_4\text{NClO}_4$. $\nu=100 \text{ mV/sec}$

CHAPTER 4

COORDINATION COMPOUNDS
AND ELECTROCHEMISTRY

4.1 Model Compound Electrochemistry

A series of novel and literature mono- and dinuclear complexes were synthesized to provide a foundation for the study of the target polymers. The electrochemistry of these model complexes is summarized in table 4.1. Half-wave potentials and anodic-to-cathodic peak separations are listed as measured in acetonitrile solution. Errors of several millivolts should be considered as a result of limited analogue-to-digital converter bit resolution, the acquisition and smoothing algorithms, and in some cases due

cmpd code	ligand	metal centre	Acid		Base	
			$E_{1/2}$	ΔE_p	$E_{1/2}$	ΔE_p
42	33	2 Ru(bpy) ₂ ²⁺	1.11 ₈	0.08 ₅	0.66 ₃	0.15 ₅
43	35	Ru(bpy) ₂ ²⁺	1.20 ₆	0.07 ₇	0.71 ₄	0.06 ₅
46	38	2 Ru(bpy) ₂ ²⁺	0.88 ₄	0.05 ₈		
47	36	2 Ru(bpy) ₂ ²⁺	1.39 ^{a,b}	0.08		
			1.60 ^{a,b}	0.07		
48	35	Ru(trpy)(Cl) ⁺	0.67 ₁ ^a	0.11 ₆		
49	35	Ru(trpy)(H ₂ O) ²⁺	1.08 ₀ ^a	0.16 ₁		
50	36	2 Os(bpy) ₂ ²⁺	0.77 ₈	0.10 ₅		
			1.01 ₉	0.22 ₇		

^a neutral electrolyte

^b $\nu=200$ mV/sec

Table 4.1: $E_{1/2}$ (V vs. SSCE) and ΔE_p (V) of model complexes in CH₃CN containing 0.1 mol dm⁻³ Et₄NClO₄ containing HClO₄ or Bu₄NOH, except where noted, as measured with a Pt disc electrode. $\nu=100$ mV/sec, except where noted.

to poor clarity of the peaks. This was particularly true of the dinuclear complexes **47** and **50**.

Model compound **42** shows peak separation considerably greater than the 29.5 mV which would be ideally anticipated for a concerted two electron transfer process. This phenomenon is even more evident in the basic medium, providing support for Haga's findings [62] for the same compound at a glassy carbon electrode under slightly different conditions. Haga attributed this behaviour to the manifestation of a pair of independent waves, separated by only a few millivolts. The pair of waves stemmed from the interaction of the two metals through the ligand, with this coupling being enhanced upon deprotonation of the ligand. Novel mononuclear compound **43** provides further support for this claim: its redox wave's peak-to-peak separation is much closer to the expected 59 mV, and does not display a significant pH dependence.

The novel dinuclear complexes **46**, **47**, and **50** explore an alternate benzimidazole construct, with the two metal atoms being located on opposing sides of the spacer unit. The hydroxy-based complex **46** exhibits an additional redox wave in neutral media at -0.93_5 V ($\Delta E_p = 0.07_0$ V, $\nu = 100$ mV/sec) due to a hydroquinone-quinone process on the central ring. This indicates that the complex exists in the quinoid form under ambient conditions, consistent with the four perchlorate counterions found in the elemental analysis (see §2.5.1.5). This wave is similar in area to the Ru(III/II) wave, showing that two electrons are involved in this ligand-based process. The Ru(III/II) wave occurs at a potential much lower than that found in the pyridine type complexes, consistent with the increased electron density at the oxygen atom, compared to nitrogen. The evident increase of electron energy at the metal centre could have had interesting implications in the analogous polymer complex's electrochemical behaviour, but unfortunately that compound could not be synthesized. The peak separation of the Ru(III/II) wave suggests that there may be some

slight coupling between the metal sites, at a level comparable to **42**. The pyrazine models **46** and **50** on the other hand have metal-metal interactions across the ring so strong that two waves are clearly resolved. This phenomenon will be shown to have important consequences in the electrochemistry of the corresponding polymers.

The terpyridyl complexes **48** and **49** represent the exploration of the applicability of the benzimidazole polymer systems towards electrocatalysis. The intended goal of preparing a polymer with a labile chloro ligand is reflected here; displacement of this ligand by some other species represents the first step in an electrocatalytic system. The ease with which **48** is converted to the aquo complex **49**, as implied by the change in $E_{1/2}$ (see table 4.1) shows the validity of this approach, and the rapid aquation of halopentaamine type ruthenium complexes is well known [123]. The polymer aquo complex could be potentially useful as a catalyst precursor polymer modified electrode. Unfortunately, attempts to synthesize and isolate the corresponding polymer were unsuccessful, giving only an intractable solid, probably consisting of a polymer crosslinked through the coordination site vacated by the labile chloro ligand. Attempts to prove this through the disappearance of the $\nu(\text{Ru-Cl})$ signal, which occurs near 330–340 cm^{-1} [123] in the far infrared spectrum, were unsuccessful owing to decomposition of the polymer under the intense green laser light of the Raman microprobe equipment used.

4.2 Polymer Complexes

The metal complexes of the polymers exhibit many interesting electrochemical and spectroelectrochemical traits. Electron transport and intervalence transfer will be treated separately in later chapters. Like the model compounds, the polymer complexes are strongly influenced by the presence or absence of the imidazole proton, and hence by pH.

4.2.1 Molecular Mass

Gel permeation experiments were employed to ascertain the approximate molecular masses of the polymer complexes. With Sephadex G-75 (rated MM 1000-50,000) as the stationary phase, solutions of the polymer complexes, appropriate model compounds, and a similar osmium polymer¹, $\text{Os}(\text{bpy})_2(\text{polyvinylpyridine})\text{Cl}_2$ of known $\text{MM} > 10^5$ were eluted individually with aqueous methanol solutions acidified slightly with HCl. The polymers eluted simultaneously with the solvent front, while the relatively low molar mass model compounds were retained at the head of the column. From this it was concluded that the polymer complexes were true polymers, having MM greater than 5×10^4 . This is sufficiently high that the electrochemical and spectroscopic properties of these systems may be considered to reflect material of effectively infinite chain length; the electronic properties of conjugated systems are known to converge to approximately constant values by ca. twenty repeat units [124].

4.2.2 Film Preparation and Solubility Concerns

The solubility of the polymers is greatly enhanced by the introduction of the coordinated metal sites. Conveniently, the bisbipyridyl ruthenium(II) and osmium(II) complexes dissolve well in acetonitrile containing optimally ca. 8% v/v water, and in wet nitromethane (water is not miscible with nitromethane, but warming a mixture of the two solvents with the polymer complex results in the desired dissolution). Either of these solvent systems is suitable for casting the polymer complex onto Pt disc electrodes, however it was found that the nitromethane system usually gave films of superior quality and uniformity. Other solvent systems, *e.g.*, methanol acidified with HCl, proved not to be as widely applicable. The complexes of **PPzBBIM** are soluble in dry MeCN; for electrochemical experiments other solvent combinations must be employed. The mixed solvent system 2:1 CH_2Cl_2 :MeCN was found to be suitable.

¹ Courtesy of Dr. Johannes G. Vos, Dublin City University

4.2.3 Optical Properties

4.2.3.1 UV-visible spectroscopy

The UV-visible spectrum of **Ru-PPyBBIM** is shown in Figure 4.1 overlaid with the uncoordinated polymer for comparison. It is evident that the coordination compound retains many features of the parent polymer. The intense polymer $\pi \rightarrow \pi^*$ transition is shifted only slightly, from 400 to 410 nm, although this could be in part attributed to solvent effects. New absorptions at 292 and 342 nm are attributed to bipyridine-based $\pi \rightarrow \pi^*$ and MLCT transitions respectively [125]. A broad Ru(II) \rightarrow polymer $d \rightarrow \pi^*$ [126] MLCT band appears on the shoulder of the $\pi \rightarrow \pi^*$ peak at *ca.* 510 nm. This is red-shifted considerably from its position in model compound **42** (*ca.* 450 nm),

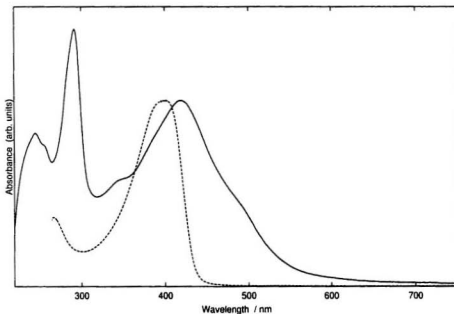


Figure 4.1: Normalized UV-Vis spectra of **Ru-PPyBBIM** in wet nitromethane (solid line) and **PPyBBIM** in dimethyl acetamide (dashed line)

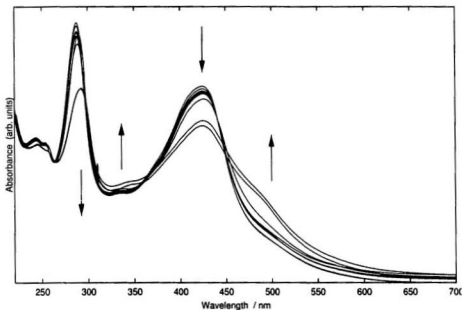


Figure 4.2: Spectral changes in **Ru-PPyBBIM**. Arrows indicate the direction of change with increasing pH over the range of 2.0 to 8.3

indicating that the Ru centre is indeed incorporated into the conjugated polymer backbone [83].

The spectral characteristics of **Ru-PPyBBIM** vary as a function of pH. In Figure 4.2, this is illustrated. A stock solution of the polymer complex was diluted quantitatively in a series of phosphate buffers, the pH of which had been measured. The resulting spectra were normalized to the local minimum at 264 nm to compensate for minor variations due to dilution and spectrometer errors.

As the pH is raised, the intensity of the polymer and bipyridine $\pi \rightarrow \pi^*$ transitions decrease while the intensity of the MLCT band increases. The changes are fairly gradual except in the pH \approx 5–6 region. This behaviour strongly parallels that of the

reported [62] dinuclear ruthenium complex **42** whose pK_{a1} was estimated to be 5.8. The isosbestic points at 360 and 450 nm suggest that protonation and deprotonation do not inflict irreversible change on the polymer complex.

4.2.3.2 Electrochromism

As is typical of pyridine-type complexes of these metals, the ruthenium and osmium metallopolymer complexes are characterized by intense coloration due to charge transfer. The previous section detailed the spectral changes resulting from the modification of the polymer ligand electron density by protonation. Changes in the metal centres' oxidation states by electrochemical means produces the spectacular colour changes summarized in table 4.2.

Two colour changes are observed for **Ru-PPzBBIM** and for **Os-PPzBBIM**, one for each oxidation. After reduction, **Ru-PPzBBIM** does not revert to its original green colour, suggesting the polymer complex is damaged by exposure to negative potentials.

The differential spectroelectrochemistry of a film of **Ru-PPyBBIM** deposited on an optically transparent ITO electrode is shown in Figure 4.3 for positive potentials only, and in Figure 4.4 over a wider voltage range. Each spectrum is presented as the change in transmission with respect to a reference spectrum taken at 0 V. Bleaching of the Ru-polymer $d\pi$ -to- $L\pi^*$ MLCT transition at 497 nm is observed

Polymer	neutral colour	oxidized colour	reduced colour
Ru-PPyBBIM	red	green-yellow	brown
Ru-PPyBDIM	red	green-yellow	
Ru-PPzBBIM	green	red-brown (1) purple (2)	brown
Os-PPyBBIM	red-brown	green	dark brown
Os-PPzBBIM	green	red (1) purple (2)	

Table 4.2: Electrochromism in the polymer complexes

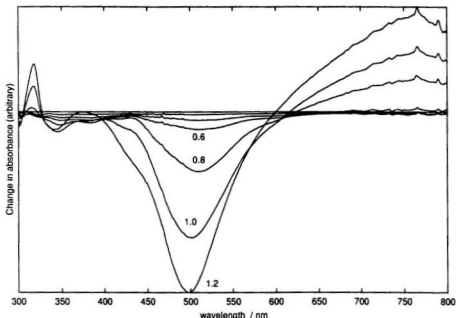


Figure 4.3: Differential spectroelectrochemical response of **Ru-PPyBBIM** as deposited on an ITO electrode. Electrolyte solution is CH_3CN containing 0.1 mol dm^{-3} Et_4NClO_4 . Spectra are referenced against that acquired at 0 V, and are shown in 0.2 V intervals

as Ru(II) is oxidized to Ru(III) . Concurrently, a broad new band due to polymer- Ru(III) LMCT [85, 127] arises with $\lambda_{\text{max}} = 775 \text{ nm}$. This behaviour is similar to the solution spectroelectrochemistry of the dinuclear Ru complex bridged by model compound **34** [61]. It should be pointed out that the bleaching is due entirely to the change of oxidation state at the metal centre, not to dissociation of the complex.

Reducing the polymer film down to -1.4 V results in the intensification of the Ru-polymer $\text{d}\pi\text{-to-L}\pi^*$ MLCT, indicating that the introduced electrons are indeed located on the bipyridine ligands; concentration of electron density on the polymer would discourage this transition. Further reduction to -2.0 V leads to the splitting

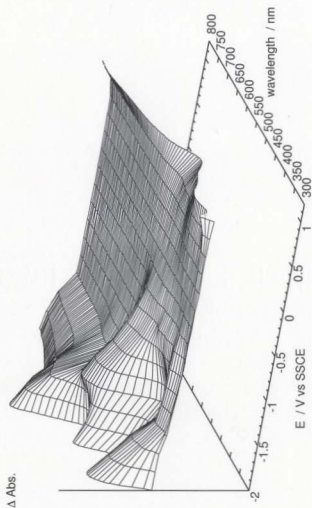


Figure 4.4: Differential spectroelectrochemical response of **Ru-PPyBBIM** as deposited on an ITO electrode. Electrolyte solution is CH_3CN containing 0.1 mol dm^{-3} Et_4NClO_4 . Spectra are referenced against that acquired at 0 V, and are shown in 0.2 V intervals from -2.0 V to 1.2 V

of this band into two new absorptions at 442 and 557 nm. It is also interesting to note that slight spectral changes are detected in potential regions where the polymer complex is electrochemically inactive.

4.2.4 Cyclic Voltammetry

The cyclic voltammetry of thin films of Ru and Os complexes of the polymers exhibit several interesting features. For all but very thick films, thin layer cyclic voltammetry was exhibited, even for sweep rates up to 1 V/sec. Small ΔE_p and $i \propto \nu$ were the rule [128].

For Ru(bpy)₂ complexes, a redox wave due to the Ru(III/II) couple appears in the region of ca. 0.8 to 1.3 V, while for the corresponding osmium complexes the Os(III/II) waves are found in the range of 0.4 to 1.1 V.

The potential of the M(III/II) wave is influenced by the degree of protonation of the polymer backbone. The two extremes are presented in Figure 4.5, where a thin film of **Ru-PPyBBIM** on Pt was cycled in CH₃CN containing 0.1 mol dm⁻³ Et₄NClO₄ which had been treated with a few drops of either concentrated HClO₄ or MeOH containing 1 mol dm⁻³ Bu₄NOH. In the basic medium, $E_{1/2}$ [Ru(III/II)] is at ca. 0.8 V vs. SSCE, while in acidified electrolyte the wave occurs at ca. 1.2 V vs. SSCE. These potentials vary slightly between films. This behaviour opens up some intriguing possibilities of using this sort of polymer complex system as a proton-switched molecular wire or valve [129].

The acid-base behaviour of the Ru(III/II) wave is predictable. In Figure 4.6, the relationship between $E_{1/2}$ and pH is plotted for a series of **Ru-PPyBBIM** cyclic voltammograms acquired in aqueous phosphate buffer electrolyte. It is evident that there is a linear relationship between these two parameters, with a slope of -63 mV/pH in the pH 2–4 region. This is consistent with the anticipated one-electron one-proton

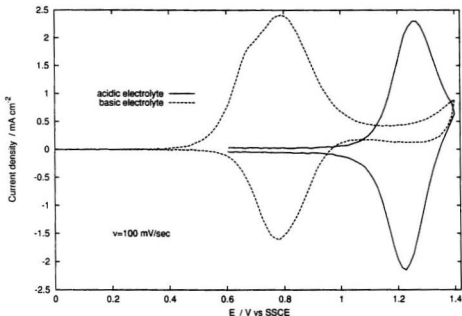


Figure 4.5: Cyclic voltammetry of a thin ($\Gamma_{Ru}=3.6 \times 10^{-8}$ mol \cdot cm $^{-2}$) film of **Ru-PPyBBIM** on a 0.0052 cm 2 Pt disc electrode. 0.1 M NEt $_4$ ClO $_4$ in MeCN containing ca. 50 mM HClO $_4$ (solid line) or ca. 5 mM NBu $_4$ OH (dashed line)

process. The relationship between $E_{1/2}$ and pH is an important one since it clearly indicates that the charge distribution along the polymer backbone, controlled by adding or removing the imidazole proton, has a direct influence over the electron density on the metal centre. The pK_a of this system is 5.5 which compares well with the pK_a of the analogous dinuclear compound **42** (see § 4.2.3.1).

The steady state cyclic voltammetry of a thin film of **Ru-PPyBBIM** on Pt in neutral CH $_3$ CN containing 0.1 mol dm $^{-3}$ Et $_4$ NClO $_4$ over a broad potential window typically resembles that presented in Figure 4.7. A pair of bipyridine-based reductions [126, 130] appear at -1.50 and -1.76 V *vs.* SSCE. The Ru(III/II) couple is present

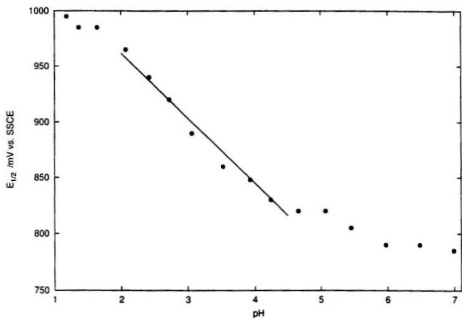


Figure 4.6: Changes in $E_{1/2}$ of a film of **Ru-PPyBBIM** exposed to a series of aqueous phosphate buffers. The indicated line has slope -63 mV/pH

near its previously established lower extreme of ca. 0.8 V, and varies somewhat between films.

An interesting development in the present voltammogram is the appearance of a pair of sharp pre-peaks, an oxidation before the Ru(III/II) wave, and a reduction before the first bipyridine wave. The pre-peaks vary in position and magnitude from film to film, and exist only as a pair; one peak will not appear for more than one or two cycles unless the sweep potential window is sufficient such that the other has been accessed. The evidence suggests that the pre-peaks result from the oxidation and reduction of water trapped within the polymer complex film: exposing the film to potentials below ca. -1.2 V reduces the water to OH^- , while sweeping the potential

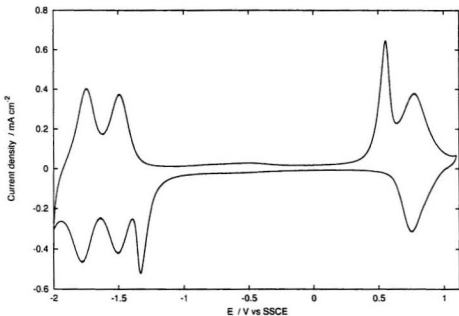


Figure 4.7: Steady state cyclic voltammetry for a thin film of **Ru-PPyBBIM** on a 0.078 cm^{-2} Pt disc electrode in CH_3CN containing $0.1 \text{ mol dm}^{-3} \text{ Et}_4\text{NClO}_4$. $\nu=100 \text{ mV/sec}$

past ca. 0.6 V results in the oxidation of OH^- to O_2 and H^+ . This is supported by the following observations:

1. Either peak exists for any extended duration only when the other is present.
2. The influence of the reduction pre-peak on the Ru(III/II) redox wave.

The influence of hydroxide on this wave was detailed earlier. If the reduction pre-peak is in fact due to some hydroxide producing process, this can account for the observed position of the Ru(III/II) wave in Figure 4.7, near the limit exhibited in basic electrolyte. If the potential limits of cyclic voltammetry are set so that the

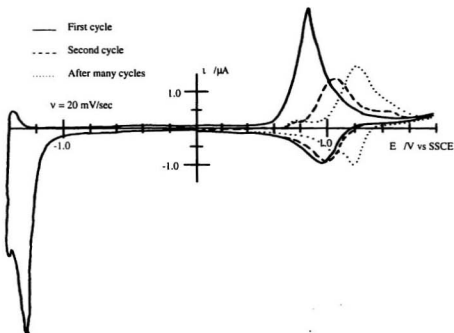


Figure 4.8: Gradual migration of the **Ru-PPyBBIM** Ru(III/II) wave following change of the lower switching potential to more positive than the reduction pre-peak

reduction pre-peak is accessed, and then the lower limit changed so that the switching potential is made more positive than the pre-peak, a gradual drift of the Ru(III/II) wave towards the acidic limit is seen. This is demonstrated in Figure 4.8 (note that in this CV the oxidation pre-peak overlaps the Ru(III/II) wave).

The addition of a small quantity of water to the electrolyte solution has no effect on the position or magnitude of these pre-peaks. It appears then that the water involved in this process is trapped within the polymer matrix and has its origin either before or during the film casting process. Benzimidazole polymers are extremely hygroscopic [2], and on the basis of elemental analyses (see section 2.7) this trait is

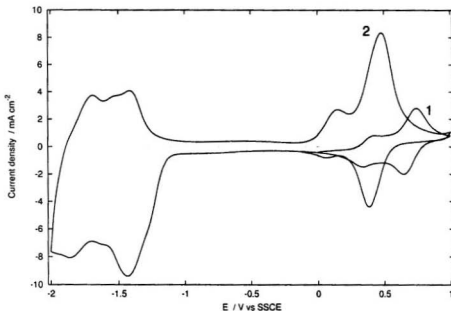


Figure 4.9: Cyclic voltammetry of a thin **Os-PPyBBIM** film in CH_3CN containing $0.1 \text{ mol dm}^{-3} \text{Et}_4\text{NClO}_4$

shared to some extent by their complexes.

The behaviour of the osmium analogue **Os-PPyBBIM** is similar with acid-mediated redox waves being evident. A cyclic voltammogram of **Os-PPyBBIM** in neutral CH_3CN containing $0.1 \text{ mol dm}^{-3} \text{Et}_4\text{NClO}_4$ is shown in Figure 4.9. Similar to the ruthenium analogue, the migration of the Os(III/II) wave to lower potentials is observed following exposure to negative potentials. It is interesting to note that the first potential sweep exhibits two distinct waves, suggesting localized protonated and deprotonated regions exist along the backbone. In Figure 4.10 the behaviour of the polymer film in acidic and basic electrolyte is presented, indicating the potential extremes of the Os(III/II) wave. In the acidified electrolyte, there appears to be

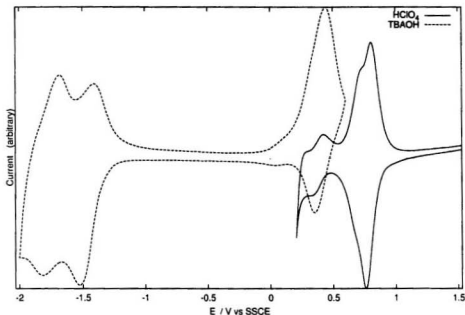


Figure 4.10: Cyclic voltammetry of two **Os-PPyBBIM** films in CH_3CN containing $0.1 \text{ mol dm}^{-3} \text{ Et}_4\text{NClO}_4$ containing either a small quantity of HClO_4 (solid line) or Bu_4NOH (dashed line)

some small response due to deprotonated backbone, suggesting the acid did not fully penetrate the film. Reasons for this discrepancy are not clear.

The cyclic voltammograms of **Ru-PPyBDIM** and **Ru-PPyBBIM** are very similar, and so the former will not be discussed in any detail. A list of $\text{M(II)}-\text{M(III)}$ redox potentials is summarized in table 4.3

Like its model compound **47**, the ruthenium and osmium complexes of the pyrazine polymer, **PPzBBIM**, exhibit the unusual property of two distinct M(III/II) based redox waves, indicating a high degree of coupling through the pyrazine ring. In Figure 4.11 the pair of ruthenium waves are clearly evident at 1.13 and 1.29 V

Polymer complex	$E_{1/2}$	
	acid	base
Ru-PPyBBIM	1.24	0.79
Ru-PPyBDIM	1.23	
Ru-PPzBBIM	1.13	
	1.29	
Os-PPyBBIM	0.78	0.40
Os-PPzBBIM	0.75	
	1.07 ₅	

Table 4.3: Estimated $E_{1/2}$ for the M(III/II) couple for ruthenium and osmium polymer complexes. Potentials are given in volts vs. SSCE

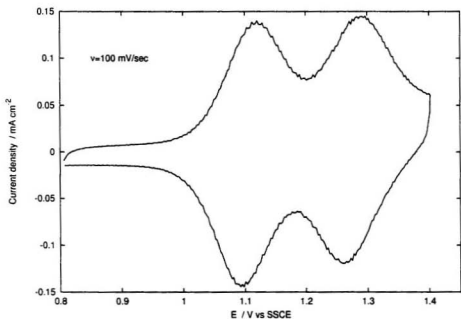


Figure 4.11: Cyclic voltammetry of a thin film of **Ru-PPzBBIM** on a Pt disc electrode in 2:1 CH_2Cl_2 :MeCN containing $0.1 \text{ mol dm}^{-3} \text{ Et}_4\text{NClO}_4$ and two drops HClO_4

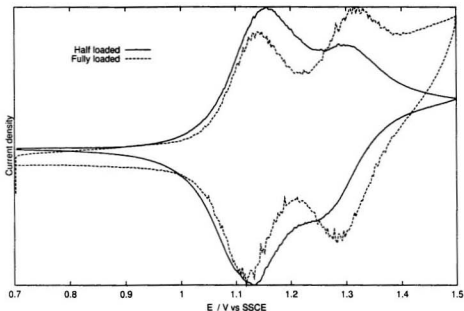


Figure 4.12: Cyclic voltammetry of films of fully loaded and half loaded **Ru-PPzBBIM** on a Pt disc electrode in 2:1 CH_2Cl_2 :MeCN containing 0.1 mol dm^{-3} Et_4NClO_4 and two drops HClO_4

vs. SSCE. The large separation between the $\text{Ru(III),Ru(III)}/\text{Ru(III),Ru(II)}$ and the $\text{Ru(III),Ru(II)}/\text{Ru(II),Ru(II)}$ waves is a well known characteristic [123, 131] of the famous Taube-Creutz compound $[(\text{NH}_3)_5\text{Ru}(\text{pz})\text{Ru}(\text{NH}_3)_5]^{5+}$ [132] and many pyrazine-bridged bis(ruthenium) variants such as this. Applying equation 1.3, K_{corr} for this system is 5.0×10^2 . Interestingly, the redox wave of the metal in a singly coordinated pyrazine is coincident with the first wave in a doubly coordinated ring (as opposed to occurring somewhere between the two waves). This was shown by a sample of **Ru-PPzBBIM** which had been prepared with one-half loading. The cyclic voltammograms in Figure 4.12 are for films of the half loaded and nearly fully loaded

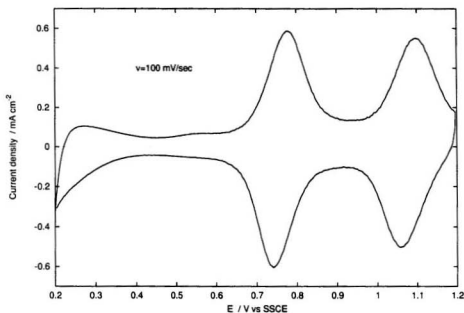


Figure 4.13: Cyclic voltammetry of a thin film of **Os-PPzBBIM** on a Pt disc electrode in 2:1 CH_2Cl_2 :MeCN containing $0.1 \text{ mol dm}^{-3} \text{ Et}_4\text{NClO}_4$ and two drops HClO_4

polymers. With the majority of Ru in singly occupied pyrazine units, the lower potential wave is much larger in magnitude than the second. This provides a quick and convenient means of ascertaining the fraction of metal centres that exist in dinuclear pyrazine sites in the polymer.

The osmium polymer complex exhibits a pair of redox waves with an even larger $\Delta E_{1/2}$, ca. 0.33 V, as shown in Figure 4.13. K_{com} for the Os complex turns out to be 3.1×10^5 , indicative of the enhanced stability of the mixed valence unit in this system.

Ru-PPzBBIM is not stable towards reduction as indicated in Figure 4.14. One sweep through the negative potential region results in the immediate disruption of the film's electrochemistry. Only in the first sweep are the two Ru(III/II) waves

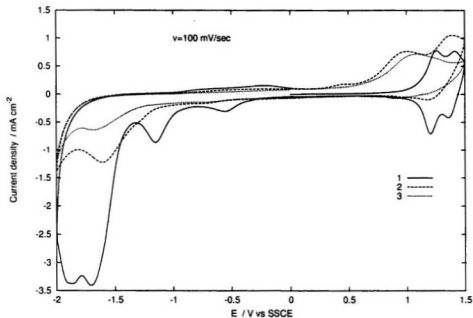


Figure 4.14: Three consecutive cyclic voltammograms of a thin film of **Ru-PPzBBIM** on a Pt disc electrode in 2:1 CH_2Cl_2 :MeCN containing 0.1 mol dm^{-3} Et_4NClO_4 .

clearly evident in addition to a pair of irreversible reductions at -1.70 and -1.87 V *vs.* SSCE. The current magnitude of these reductions seems disproportionately large, indicating there is more involved than the simple bipyridine reductions observed in **Ru-PPyBBIM**, probably some process which degrades the backbone. This is further supported by the failure of the polymer to return to its neutral colour after being reduced (see section 4.2.3.2).

Attempts to coordinate $\text{Ru}(\text{bpy})_2^{2+}$ with **PHyBDIM** and **PPyBDT** were unsuccessful.

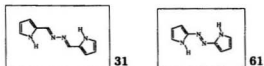


Figure 4.15: Polymerizable azopyrrole compounds pyrrolyl-2-aldazine (**31**) and 2,2'-azopyrrole (**61**)

4.3 Pyrroles

Zotti and co-workers recently reported [133] the electrochemical polymerization of the known azopyrrole compounds 2,2'-azopyrrole **31** [98] and 2,2'-azopyrrole **61** [134] (see Figure 4.15). The resulting polymers exhibited unusually narrow bandgaps for pyrrole electropolymers, and this was attributed to the inclusion of electron accepting azo groups, leading to a more easily accessed LUMO. An unexplored aspect of these compounds is their metal complexes; the azo linkage introduces an excellent bidentate coordination site in conjunction with the pyrrole nitrogen.

Pyrrolyl-2-aldazine **31** was successfully prepared in accordance with literature methods [98], and the electrochemical behaviour reported by Zotti was duplicated. Its dinuclear bisbipyridyl ruthenium(II) complex **45** was also isolated, but did not polymerize electrochemically.

CHAPTER 5

ELECTRON TRANSPORT IN POLYMER COMPLEXES

5.1 Polymer Thickness

A critical parameter for assessing the electron diffusion coefficient D_e is the thickness of the polymer film d . Slow sweep cyclic voltammetry of the M(II)–M(III) wave permits the straightforward evaluation of charge passed (Q) by integration of current through time. The surface coverage of species M (Γ_M) is related to the electrode area A :

$$\Gamma_M = Q/FA \quad (5.1)$$

The volume occupied by the individual metal units can be estimated on the basis of crystal structures and known dry densities of similar materials. From the crystal structure of $\text{Ru}(\text{bpy})_3(\text{PF}_6)_2$ [135], the concentration of metal sites C_M in the ruthenium metallopolymer may be inferred as $1.6 \times 10^{-3} \text{ mol/cm}^3$. Similarly, a concentration of $1.5 \times 10^{-3} \text{ mol/cm}^3$ (based on the dry density of $[\text{Os}(\text{bpy})_2(4\text{-vinylpyridine})_2]^{2+}$ [136]) was taken as an estimate for the osmium polymers. With this information, the film thickness d is calculated:

$$d = \Gamma_M / C_M \quad (5.2)$$

This approach has two flaws:

1. The actual volume occupied by a metal site in the polymer systems should in fact be larger than predicted above.
 - Size of unit: the length of the polymer repeat unit, *e.g.*, one pyridine plus one benzimidazole, is much longer than the length of the bipyridine found in the compounds after which the volume is modeled. This means that the effective size of a metal site is extended in at least one dimension

- Vacant units: Not all of the available sites along the polymer are necessarily coordinated to $M(\text{bpy})_2^{2+}$. For example, an early **Ru-PPyBBIM** sample was found to have only *ca.* 60% of its available ligating sites in use. Clearly this results in a further extension of the average volume of a site
 - Packing: Presumably the packing of the polymer complexes will not be nearly as ordered as that of the model compounds. This should result in an average unit size that is bigger still.
2. Polymer swelling: Film swelling by the uptake of electrolyte solution is a well-known [137] and important [138] phenomenon. The degree of swelling can vary from around 15 to 180% for non-polar aprotic polymers [139, 140] to as much as one hundred-fold for a protonated polar polymer [141]. The process is critical for the introduction of the counterions necessary to maintain electroneutrality and also for the creation of the free volume through which these ions may move. This point is further complicated by changes in the swelling concomitant with changes in the oxidation state of the redox active sites; an *in situ* ellipsometric study of a viologen-siloxane polymer indicated such changes on the order of 25% [137].

Neither is considered in the present calculation of d . It is clear from point (1) that the true concentration C_M should be lower than calculated, which, from equation 5.2, would entail a thickness larger than expected, and the swelling considered in point (2) will make d even larger still. These errors in d imply that calculated D_e values will be in error, but they will underestimate the true value as will be shown by the equations in later sections.

Scanning electron microscopy revealed that the estimates of d are not unreasonable. From the above treatment it is possible to estimate the average thickness of a

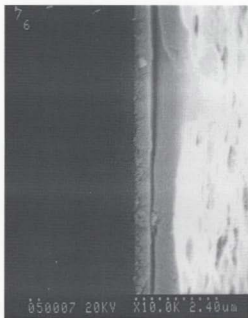


Figure 5.1: SEM image of the cross section of a **Ru-PPyBBIM** film cast on an ITO glass slide

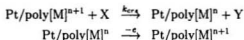
drop of **Ru-PPyBBIM** dried on a slide of conductive ITO glass. After measuring the surface coverage of the drop by cyclic voltammetry, carefully snapping the slide in the middle of the dried drop permitted the examination of the polymer film in cross section. Such an image is shown in Figure 5.1. While thicker at the edges, the bulk of the drop was seen to be of a regular thickness in good agreement with the calculated value of $0.35\ \mu\text{m}$.

5.2 Rotating Disc Voltammetry (RDV)

5.2.1 Background

The oxidation of an electrochemically active species X in solution at a rotating disc electrode coated with a redox polymer acting as a mediator can be represented as in

Scheme 5.1.



Scheme 5.1: Mediated electron transfer at a rotated electrode

It has been postulated [142] that the current may be controlled by four factors:

1. The rate of mass transport of X from the bulk solution to the polymer/solution interface, as dictated by the electrode rotation speed ω and the diffusion coefficient of X, D_X .
2. The rate of electron transfer (cross-reaction rate constant) k_{crs} between the polymer and X at the interface, and within the polymer if permeation has occurred.
3. The rate of permeation by X into and within the film, with partition coefficient P and diffusion coefficient $D_{X,poly}$. Measurements on films of polymerized tris(vinylbipyridyl) ruthenium(II) have shown that the permeability $PD_{X,poly}$ of fairly bulky species in solution (*e.g.*, Fe(bpy)_3^{2+} , $\text{Ru(bpy)}_2\text{Cl}_2$) is very small, $< 7 \times 10^{-12} \text{ cm}^2/\text{sec}$.
4. The rate of charge transport through the film. It is this diffusion-like process which is of interest in the present systems, and is described as the electron diffusion coefficient D_e .

On the basis of these criteria, Ikeda *et al.* have formulated [142] a general expression representing the limiting current of polymer mediated electron transfer at a rotating electrode (with negligible permeation):

$$\frac{1}{i_{lim}} = \frac{1}{nFAk_{cs}\Gamma C_X} + \frac{1}{nFAD_e C_M/d} + \left[1 + \frac{i_{lim}}{K_{eq}(nFAD_e C_M/d)} \right] \cdot \frac{1}{0.62nFAD_X^{2/3} \nu^{-1/6} \omega^{1/2} C_X} \quad (5.3)$$

where k_{cs} is the cross section rate constant, as above, Γ is the surface coverage of electroactive sites at the polymer-solution interface (*i.e.*, with which X may react), C_X and C_M are the concentrations of X in solution and M in the polymer, respectively, d is the film thickness, K_{eq} is a function of the difference between formal potentials of poly-M and X, $K_{eq} = \exp[RT/nF(E_{poly-M}^{o'} - E_X^{o'})]$ and the remaining terms have their usual rotating disc meanings: D_X is the diffusion coefficient of the sacrificial species, ν is the kinematic viscosity, and ω is the rotation speed of the electrode in rad s^{-1} .

If X is chosen so that $E_{poly-M}^{o'}$ is several hundred millivolts greater than $E_X^{o'}$ then the K_{eq} term becomes insignificant. Furthermore, when potentials sufficiently high to oxidize the polymer mediator are reached, the overpotential on X will be sufficiently high as to render $1/k_{cs}$ vanishingly small, and so that term may also be disregarded. Clearly equation 5.3 simplifies to equation 5.4, where i_{lim} is described by two discrete influences acting in parallel: one controlled by electron transport within the film, and one controlled by mass transport in the solution. The overall scheme is pictured in Figure 5.2

$$\frac{1}{i_{lim}} = \frac{1}{nFAD_e C_M/d} + \frac{1}{0.62nFAD_X^{2/3} \nu^{-1/6} \omega^{1/2} C_X} \quad (5.4)$$

It is evident from equation 5.4 that the response will tend towards being independent of ω under conditions of relatively rapid mass transport. An inverse Levich plot [128], $1/i_{lim}$ vs. $\omega^{-1/2}$, should yield the quantity $nFAD_e C_M/d$ as the reciprocal of its intercept.

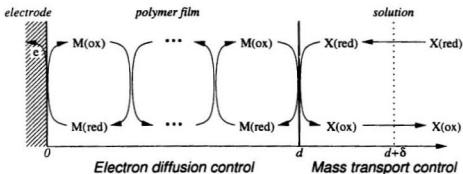


Figure 5.2: Polymer-mediated electron transfer to/from species X in solution

5.2.2 Experimental Details

The electrodes used in these experiments consisted of a Pt disc of diameter 1.0 mm ($A=0.0078 \text{ cm}^2$) sealed in a Teflon carrier. Electrode rotation was performed with a Pine Instruments ASR Analytical Rotator. A Pine RDE-4 potentiostat controlled the potential in a three-compartment cell. All potentials are referenced against an uncalibrated SSCE electrode.

Electrolyte solutions were made approximately 0.1 M in Et_4NClO_4 , acidified to ca. 10–50 mM in HClO_4 , and typically 5–10 mM in ferrocene (Cp_2Fe) as the sacrificial donor. Other sacrificial donors were tried, but they were deemed unsuitable owing to instability in the acidic medium ($\text{Co}(\text{bpy})_3^{2+}$, $\text{Fe}(\text{bpy})_2(\text{CN})_2$ [143]), to excessively positive E° ($\text{Fe}(\text{bpy})_3^{2+}$), or to prohibitively high cost ($\text{Os}(\text{bpy})_3^{2+}$).

5.2.3 Leak Current

A typical rotating disc voltammogram of a **Ru-PPyBBIM** film on a rotating Pt disc electrode is presented in Figure 5.3. One immediately apparent problem with the system is the appearance of a spurious current density plateau, j_{leak} ($j = i/A$),

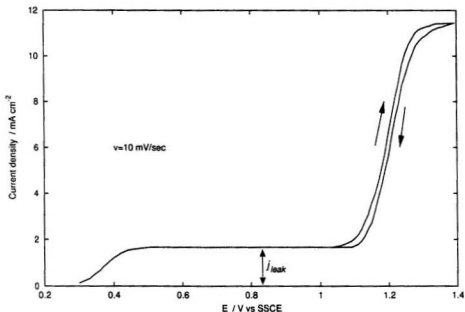


Figure 5.3: Typical rotating disc voltammogram of a mediating thin film of **Ru-PPyBBIM** on a Pt disc electrode in CH_3CN containing $0.1 \text{ mol dm}^{-3} \text{Et}_4\text{NClO}_4$ and 0.01 mol dm^{-3} ferrocene, and acidified with HClO_4

with $E_{1/2} \approx 0.37 \text{ V}$ due to Cp_2Fe . This is observed in a region where the mediating polymer is electrochemically inactive and, consequently, electrically insulating. The mediation current is observed subsequently with an onset near 1.1 V . To conclude whether i_{leak} should be included with i_{lim} , it is important to consider the source of i_{leak} . Two scenarios are possible. Small areas of the Pt surface may be exposed to the bulk solution due to incomplete coverage by the film during the casting process or to small portions of the film having been torn off due to the mechanical stress to which the film is subjected in the course of electrode rotation. In this case, the leak current should be disregarded. The alternate possibility is that Cp_2Fe is able to diffuse through the polymer film, permitting a small quantity to reach as far as

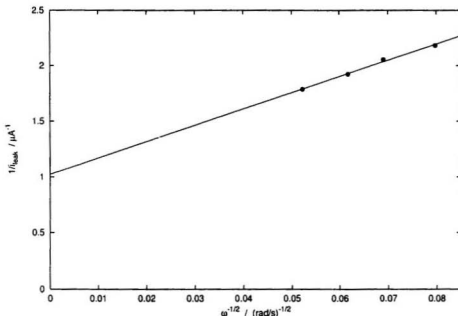


Figure 5.4: Linear relationship between $1/i_{\text{leak}}$ and $\omega^{-1/2}$ for a RDV electrode coated with **Ru-PPyBBIM**

the electrode-polymer interface. In this case, the presence of sacrificial species within the film would need to be accounted for when the redox concentration inside the film begins to build as the polymer is oxidized.

Several pieces of evidence suggest that the first model is the correct one:

1. $1/i_{\text{leak}}$ is linear with $\omega^{-1/2}$. A typical example is shown in Figure 5.4. This indicates that mass transport in the bulk solution is the main influence on the magnitude of this current. In the event where diffusion through the film were responsible one might anticipate this process to be limiting.
2. There is no relationship between i_{leak} and Γ for a series of coated electrodes.

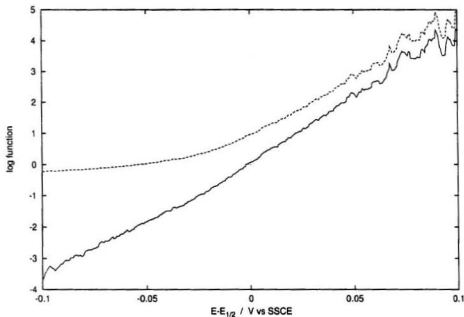


Figure 5.5: Effect of subtracting i_{leak} : $y = \log[(i - i_{leak})/(i_{lim} - i)]$ (solid line) and $y = \log[(i)/(i_{lim} - i)]$ (dashed line).

3. The shape of the i - E curve for the polymer-mediated current should (ideally) be Nernstian; a plot of $(i/(i_{lim} - i))$ against $E - E_{1/2}$ should be linear with zero intercept. Failure to subtract i_{leak} leads to non-ideal behaviour as shown in Figure 5.5. Related to this is the necessity that the current magnitude at $E_{1/2}$ equal $i_{lim}/2$. This is particularly evident when i_{leak} is relatively large as in Figure 5.6. Furthermore, the modified data treatment presented below in section 5.2.4 is applicable only when i_{leak} is removed from the $i - E$ curve.
4. Visual inspection: Following rotation, examination of the electrode surface under a microscope has revealed small regions where the film might have lifted off. The edge of the disc is particularly prone to improper film adhesion, and this is

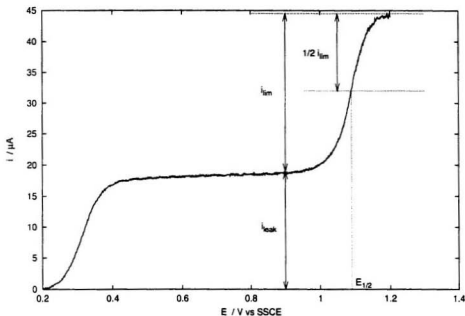


Figure 5.6: Annotated **Ru-PPyBBIM** RDV with a large leak current

likely due in part to the interaction between the Teflon sleeve and the polymer solution in the course of electrode preparation.

These conclusions are consistent with finding that mediator penetration in films of $\text{poly}[\text{Ru}(\text{vbpv})_3]^{2+}$ does not occur to significant depths [144].

5.2.4 Backbone Degradation

The preferred approach of measuring i_{lim} for a given ω involves the slow (ca. 5 mV/sec) potential sweep of the film to a potential around 200 mV more positive than $E_{1/2}$, allowing the concentration gradient in the film to become fully established. Coupled with the need for repetition at several rotation rates, this procedure leads to the

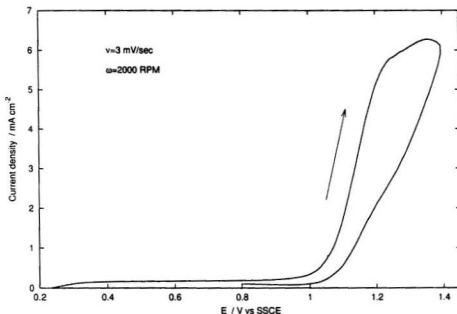


Figure 5.7: RDV current “looping” in **Ru-PPzBBIM**. Electrolyte: 2:1 (v/v) CH_2Cl_2 :MeCN 0.1 M in TEAP and ~ 8 mM in Cp_2Fe , acidified with HClO_4 .

exposure of the film to elevated potentials for extended periods of time, particularly for the ruthenium complexes. This condition leads to degradation of the polymer backbone which is manifested (i) as “loops” in the $i - E$ curves where the return sweep fails to overlap the forward sweep (figure 5.7), and (ii) decay of the limiting current, for example in back-to-back sweeps at the same rotation speed (figure 5.8), invariably the limiting current in the second voltammogram turns out to be lower than in the first.

Directly measuring the limiting current in these situations is clearly unsatisfactory. An alternate approach was developed, utilizing an adaptation of the Nernst equation (equation 5.5) to extrapolate i_{lim} from the shape of the $i - E$ curve at potentials

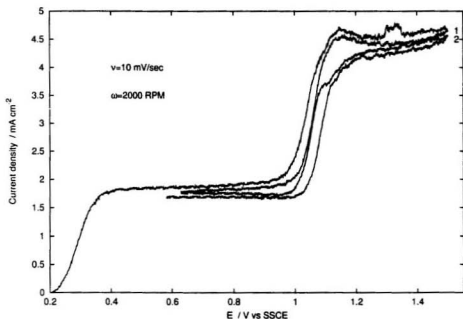


Figure 5.8: Limiting current degradation in two successive sweeps of a film of **Ru-PPyBBIM** on a RDV electrode.

below $E_{1/2}$.

$$E = E_{1/2} + (RT/nF) \ln[i/(i_{lim} - i)] \quad (5.5)$$

When the potential is below $E_{1/2}$, $i \ll i_{lim}$, and so equation 5.5 may be written as:

$$E = E_{1/2} + (RT/nF) \ln[i/(i_{lim})] \quad (5.6)$$

$$E - E_{1/2} = (RT/nF) \ln i - (RT/nF) \ln i_{lim} \quad (5.7)$$

Equation 5.7 indicates that a plot of $\ln i$ against $E - E_{1/2}$ will give a straight line with intercept equal to $\ln i_{lim}$. $E_{1/2}$ is determined from cyclic voltammetry of the electrode held stationary in an electrolyte solution not containing the sacrificial

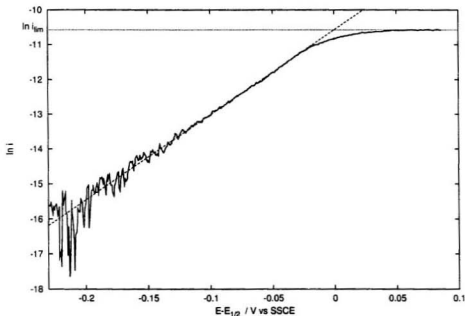


Figure 5.9: $\ln i$ vs. $E - E_{1/2}$ for a typical RDV of **Ru-PPyBBIM**, with the extrapolation line intersecting with $\ln i_{lim}$ at $E - E_{1/2} = 0$.

species. A plot representative of this alternate treatment is presented in Figure 5.9. For this particular case the true limiting current was measured for the purpose of comparison. Excellent agreement is seen between the predicted and true values of i_{lim} .

From the data in Figure 5.9 and similar experiments it is evident that with this alternate method linear sweeps need only go to around 50 mV below $E_{1/2}$; any data beyond this point is superfluous. By avoiding exposure to elevated potentials altogether, the present extrapolation method extends the life of the polymer film seemingly indefinitely.

One potential shortcoming to this approach arises from any error in the value used

for $E_{1/2}$. Small discrepancies in this quantity translate to rather large changes in i_{lim} through its logarithmic relationship on the graph. This in turn accentuates the error associated with extrapolation to the y intercept in the $1/i_{lim}$ vs. $\omega^{-1/2}$ plots which in itself can frequently be quite substantial. Additionally, a consistently inaccurate $E_{1/2}$ can introduce systematic errors into the extrapolated reciprocal current.

The present method also further supports the proposal that i_{leak} be disregarded; inclusion of i_{leak} renders this approach invalid. A small error in the value of i_{leak} used is manifested as a gentle curvature of the data in the target region.

5.2.5 Results

Owing to stability concerns, mediated RDV experiments were performed in acidic media only. Complexes of **PPyBBIM** and **PPyBDIM** were measured using acetonitrile solutions, while **PPzBBIM** complexes required the use of the mixed solvent system 2:1 CH_2Cl_2 :MeCN.

Early experiments were plagued with instability and reproducibility problems until the extrapolation method outlined in section 5.2.4 was adopted, although this approach also sometimes had problems in cases where the leak current was relatively large: minor relative errors in its measurement had a comparatively large influence on the mediation current.

An example of the inverse Levich treatment of results for a **Os-PPyBBIM** film (using the low potential i_{lim} method) is shown in Figure 5.10. This plot is typical of the minor amount of scattering resulting from errors in the extrapolated data. In this particular case a 14% error in the intercept is expected for a 68% confidence interval. This uncertainty is acceptable in light of the other sources of error in the final calculation of D_e .

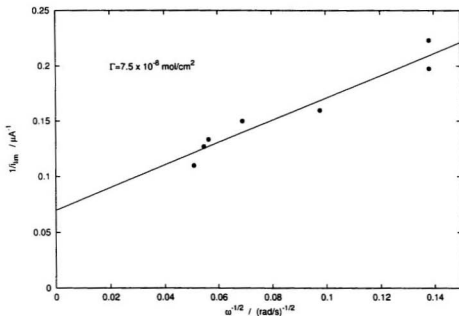


Figure 5.10: Illustrative inverse Levich plotted results for a **Os-PPyBBIM** mediated RDV, with 10 mM Cp_2Fe as sacrificial donor in 0.1 M CH_3CN containing 0.1 mol dm^{-3} Et_4NClO_4 acidified with $HClO_4$.

The pyrazine polymer **Os-PPzBBIM** gives particularly interesting voltammograms. The low formal potential of the first oxidation wave lessens the concern of instability, and the large separation of the two waves allows for the exploration of the contribution of each metal centre to charge transport in the polymer.

A typical RDV of **Os-PPzBBIM** is presented in Figure 5.11 along with a cyclic voltammogram to emphasize the position of the two $Os(III/II)$ waves. Mediation currents are observed for both redox processes, with the mediation current for the higher potential being significantly smaller than the first, in spite of the similar size of the redox waves in the cyclic voltammetry. This phenomenon will be discussed in detail in section 5.3.3. A summary of RDV data is given in table 5.1

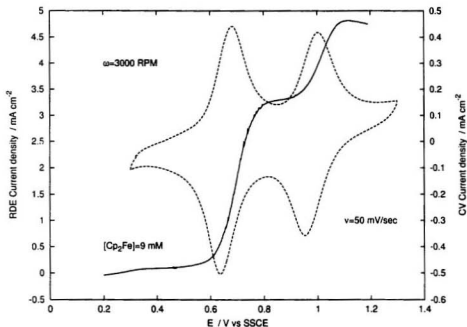


Figure 5.11: Mediated RDV of a film of **Os-PPzBBIM** (solid line) and a cyclic voltammogram (dashed line) in CH_3CN containing $0.1 \text{ mol dm}^{-3} \text{ Et}_4\text{NClO}_4$ without Cp_2Fe .

Polymer	$D_e/\text{cm}^2\cdot\text{s}^{-1}$	# of trials
Ru-PPyBBIM	4.5×10^{-9}	(4)
Ru-PPyBDIM	1.3×10^{-9}	(1)
Os-PPyBBIM	6.3×10^{-10}	(1)
Os-PPzBBIM	$2.3 \times 10^{-8 \text{ a}}$	(1)

^a first wave only

Table 5.1: Summary of RDV mediated results. **PPyBBIM** and **PPyBDIM** complexes used an acetonitrile solution, while **PPzBBIM** complexes used 2:1 $\text{CH}_2\text{Cl}_2:\text{CH}_3\text{CN}$ mixed solvent. All solutions contained ca. $0.1 \text{ M Et}_4\text{NClO}_4$, 5–20 mM Cp_2Fe , and ca. 50 mM HClO_4 .

5.3 Dual Electrode Voltammetry

5.3.1 Background

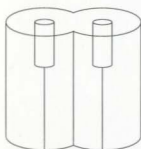
Also known as sandwich electrode voltammetry, the dual electrode technique shares many characteristics with the RDV method. Its basis also lies in determining a steady state current across the polymer film as the redox concentration gradient is maximized. Unlike the RDV, a sacrificial electron source is not required (for oxidized polymers); one electrode acts as an electrode sink, the other as an electron source. A schematic representation of the sandwich electrode is provided in Figure 5.12.

The sandwich electrode consists of a thin film of polymer complex deposited on a small ($A=1.3 \times 10^{-4} \text{ cm}^2$) Pt disc microelectrode. A thin layer of gold is vapour deposited over the polymer film and allowed to form an Ohmic contact with a second bare Pt disc. This provides electrical contact on both sides of the polymer film, hence a sandwich. The gold film is however sufficiently porous to permit the passage of counterions necessary to maintain electroneutrality within the film during the course of the electrochemical experiments. Application of potentials to the electrodes so that oxidized and reduced sites are generated across the film leads to the formation of steady-state concentration gradients. This condition is illustrated in Figure 5.13. The similarity to Figure 5.2 is obvious.

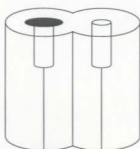
For the M(II)–M(III) process of interest here, the shape of the $i - E$ curve arises from one electrode being permitted to generate oxidized sites while the other is held far below $E_{1/2}$. The curve is generally described by [136, 145, 146]:

$$i = \frac{nFAD_e C_M^2}{\Gamma_M (1 + \exp[(gnF/RT)(E^{or} - E)])} \quad (5.8)$$

$$= \frac{nFAD_e C_M}{d (1 + \exp[(gnF/RT)(E^{or} - E)])} \quad (5.9)$$



A: Coplanar Pt disc electrodes sealed in glass housing



B: Coating of one electrode with polymer



C: Gold film coating via vapour deposition

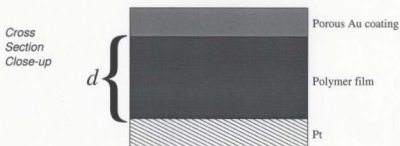
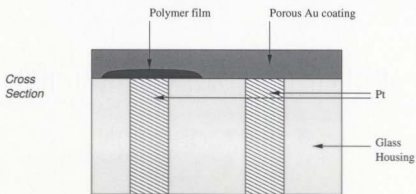


Figure 5.12: Schematic representation of a sandwich electrode assembly.

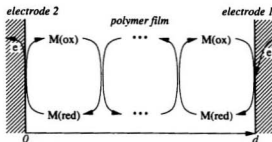


Figure 5.13: Electron transport in a sandwich electrode assembly.

with the parameters being the same as given in equation 5.4, and g which is a parameter that accounts for slight deviations from Nernstian behaviour; this well-known but little understood phenomenon [136, 142, 147, 148] is frequently observed for electroactive polymer films and is manifested as plots of $\log[i/(i_{lim} - i)]$ vs. E having slopes greater than the anticipated 59 mV and also as broadening of cyclic voltammetric waves. Ideally $g = 1$, and it can be safely disregarded for the dual electrode and RDV experiments.

When $E \gg E^o$, equation 5.9 simplifies to:

$$i_{lim} = nFAD_e C_M / d \quad (5.10)$$

Not surprisingly, equation 5.10 is equivalent to equation 5.4 without the mass transport component.

5.3.2 Experimental Details

Gold films were vapour deposited on dual electrode assemblies with an Edwards model 4 coating unit, in a vacuum below 10^{-3} Torr. The gold was vaporized on assemblies consisting of Pt wire of diameter 0.025 mm sealed in glass, one electrode having been coated with a thin film of polymer complex as described previously. Electrode potentials were controlled with a Pine Instruments RDE-4 bipotentiostat. While in

principle it should not matter which electrode is given the more positive potential, in all cases the outer gold film was maintained at a potential far below the formal potential of the polymer complex. In acidified solutions the gold electrode was held at *ca.* 0.3 V *vs.* SSCE in order to avoid the complications of H^+ reduction.

5.3.3 Results

The shape of the $i - E$ curve from a sandwich electrode is similar to that of a RDV (Figure 5.14), indicative of the Nernstian response of the system and the fundamental similarity to the rotating disc voltammogram. Like the RDV experiments, it was found that the sandwich electrodes are prone to current degradation and hystereses, particularly in cases where the metal redox potential is elevated. The use of basic media accelerates the degradation. Unlike the RDV mediated current, there is no complication by a mass transport term, and therefore only one sweep is necessary to elucidate D_e . Any degradation near the limiting current should be relatively unimportant. The dual electrode is therefore better suited for investigations in basic media.

A perennial problem with the sandwich electrodes is the formation of a bridge between the Pt and Au electrodes in the course of film deposition, resulting in an electrical short across the polymer film. A high failure rate is a common problem with these assemblies, and has been reported as high as 90% [145]. The electrical short could sometimes be broken by applying a potential of 1–2 volts between the electrodes. This “conditioning” [136] presumably burns out the link by allowing it to be rapidly heated by the large (>1 ampere) current passing through it. In the present systems, the frequency of failure could be reduced by using thicker films and by soaking the films for 15 minutes prior to use, permitting the polymer to swell.

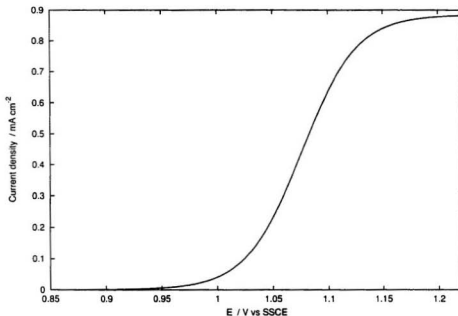


Figure 5.14: Typical $i - E$ response in a **Ru-PPyBBIM** sandwich electrode. Electrolyte solution: CH_3CN containing 0.1 mol dm^{-3} Et_4NClO_4 , acidified with HClO_4 .

While no specific provisions were made to control the thickness of the gold film quantifiably, it was found that too much gold led to an electrode with insufficient porosity; limiting currents were much smaller than expected owing to the restricted exchange of solvent and ions through this electrode.

The assessment of film thickness by cyclic voltammetry required removal of the gold film. Failure to do so gave unsatisfactory voltammograms. Attempts to perform this experiment before gold coating were unsuccessful. The exposure to solvent and electrolyte seemingly had a negative impact on the surface morphology of the polymer film, often leading to poor gold film formation and adhesion, even if the polymer had been carefully rinsed with solvent before the Au deposition process. The gold

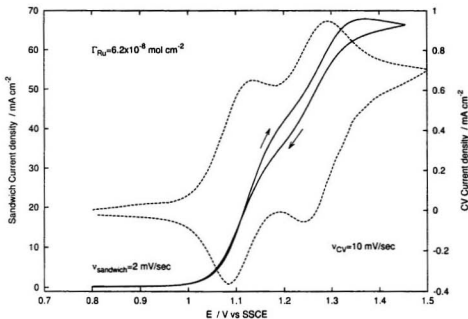


Figure 5.15: Sandwich electrode voltammetry and cyclic voltammetry (Au film removed) of a thin film of **Ru-PPzBBIM** in 2:1 (v/v) $\text{CH}_2\text{Cl}_2:\text{CH}_3\text{CN}$ containing $0.1 \text{ mol dm}^{-3} \text{Et}_4\text{NClO}_4$ and acidified with HClO_4

could however be easily removed after the dual electrode voltammetry by dipping the electrode assembly in a pool of mercury.

In section 5.2.5 it was seen that the cross-ring coupling in pyrazine polymer **Os-PPzBBIM** led to a pair of distinct mediation currents. This behaviour is also seen for sandwich electrodes of **Ru-PPzBBIM** and **Os-PPzBBIM**, examples of which are presented in Figures 5.15 and 5.16 respectively, overlaid with cyclic voltammograms. Currents were observable only in acidic electrolyte solutions; addition of Bu_4NOH to the electrolyte resulted in dissolution of the polymer film.

The distinct limiting current contribution of each metal presents an opportunity to explore the relationship between the redox wave's formal potential and the rate

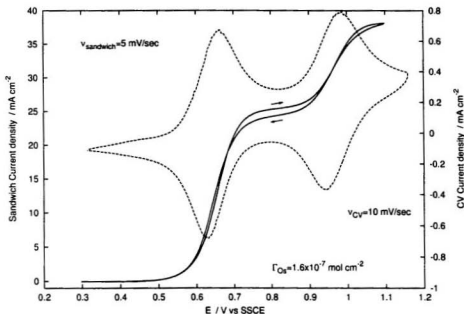


Figure 5.16: Sandwich electrode voltammetry and cyclic voltammetry (Au film removed) of a thin film of **Os-PPzBBIM** in 2:1 (v/v) $\text{CH}_2\text{Cl}_2\text{:CH}_3\text{CN}$ containing $0.1 \text{ mol dm}^{-3} \text{Et}_4\text{NClO}_4$ and acidified with HClO_4

of charge transport through the polymer film. The similar areas of the two redox waves in the cyclic voltammogram in figure 5.15 suggest that nearly all of the Ru atoms are situated in pairs across a pyrazine ring (see Figure 4.12 and accompanying text). While the proximity of the pair of waves complicates the shape of the sandwich currents, it appears that the limiting current (and hence D_e) corresponding to each wave is nearly the same.

The separation of the pair of waves in **Os-PPzBBIM** gives distinct limiting currents. Again, from cyclic voltammetry, nearly all of the metal centres can be considered to be contained in the dinuclear pyrazine environment; integration shows that $> 90\%$ of the pyrazine rings are doubly occupied. However, in this case the

limiting currents are not similar, the higher potential redox process gives a current roughly one-half of the lower potential wave.

Similar behaviour is exhibited by *in situ* conductivity measurements [149] of films of **Os-PPzBBIM** using the same assembly. Maintaining a fixed potential difference (10 mV) between the electrodes in the slow potential sweep gives a response approximating the first derivative of the dual electrode response. Conductivity σ may be calculated with equation 5.11, it being a function of current i , the fixed potential difference ΔE , film thickness d , and electrode area A . A plot of the conductivity profile obtained in this manner as a function of potential is shown in Figure 5.17. The slight decrease of the return sweep's magnitude is reproducible, and has been observed in the conductivity measurement of comparable materials on interdigitated electrodes [52, 74].

$$\sigma = \frac{id}{\Delta EA} \quad (5.11)$$

The relative conductivity corresponds well to the cyclic voltammetry, reaching local maxima at the half-wave potentials of the two redox processes, and dropping to the baseline midway between the waves. This situation is somewhat unusual in that redox polymers usually exhibit maximum conductivity at the potential where $C_{ox} = C_{red}$ [35]. In the present case peak conductivity occurs at 25% and at 75% oxidation, while the conductivity at the 50/50 state, near 0.8 V, is vanishingly small. This condition can be rationalized by taking into consideration the fact that in this state the repeat units along the polymer are essentially identical; each pyrazine is coordinated to one Os(II) and to one Os(III). This picture is analogous to the 0% and 100% oxidized case of a conventional redox polymer, where all the sites are equivalent and near zero conductivity is exhibited. In contrast, the conductivity maximum occurs when the staggering of sites in alternating redox states along the chain is greatest: 50% oxidized for conventional redox polymers, and at 25% and

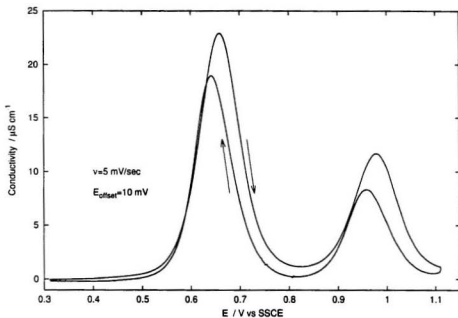


Figure 5.17: *In situ* conductivity in a film of **Os-PPzBBIM** as a function of potential, as measured by the dual electrode method in 2:1 (v/v) $\text{CH}_2\text{Cl}_2\text{:CH}_3\text{CN}$ containing $0.1 \text{ mol dm}^{-3} \text{Et}_4\text{NClO}_4$ and acidified with HClO_4

at 75% oxidation for the present system. The lack of conductivity near 0.8 V is a reflection of the unfavourable nature of the spontaneous generation of neighbouring redox sites in different net valence states:



This condition is analogous to the stability of a mixed valence dinuclear complex and can be treated similarly. The comproportionation constant K_{com} (see equations 1.2 and 1.3) gives a quantitative measure of the preference of the $[\text{Os(II)Os(III)}]\text{-poly-}[\text{Os(II)Os(III)}]$ form. From the separation of the two waves in the metallopolymer's

cyclic voltammetry, it was shown in section 4.2.4 that $K_{com} = 3.1 \times 10^5$ for this “internal” comproportionation.

Another interesting aspect of this particular system’s response is the difference in the limiting currents (hence D_e) in the simple sandwich experiment (Figure 5.16) and conductivities (Figure 5.17) for the first [Os(II)Os(II)]-poly-[Os(II)Os(III)] and the second [Os(II)Os(III)]-poly-[Os(III)Os(III)] processes. From the data in Figure 5.16, $D_e(1)$ turns out to be 1.8×10^{-8} cm²/sec, while $D_e(2) = 0.9 \times 10^{-8}$ cm²/sec. The conductivity profile, Figure 5.17, displays a similar trend with $\sigma(1) = 23$ μ S/cm being roughly twice as large as $\sigma(2) = 12$ μ S/cm. These features are reproducible over repeated scans, and are therefore not attributable to degradation of the polymer backbone.

These two properties indicate clearly that electron transport in the system is more rapid when Os(II) is the dominant state. The differences could be due to geometric influences, resulting in a better overlap of polymer and metal orbitals, or they could be a manifestation of a closer match between the relative orbital energies of the metal and the backbone. The response of the two waves in **Ru-PPzBBIM** lends support to the latter explanation. If orbital overlap were responsible, a large limiting current difference like **Os-PPzBBIM**’s might be expected. This was not the case. The proximity of the two **Ru-PPzBBIM** waves means the relative orbital energies of the backbone and the metals are closer, producing nearly equal responses, as was seen. This then provides some critical evidence for the validity of the superexchange model. A schematic energy level diagram for the Os-pyrazine polymer is presented in Figure 5.18 to illustrate this.

In the figure, Os pairs interact through the pyrazine in the smaller blocks and these subunits in turn interact through the polymer backbone — this is an adaptation of the superexchange model. Since the D_e and conductivity measurements both indicate

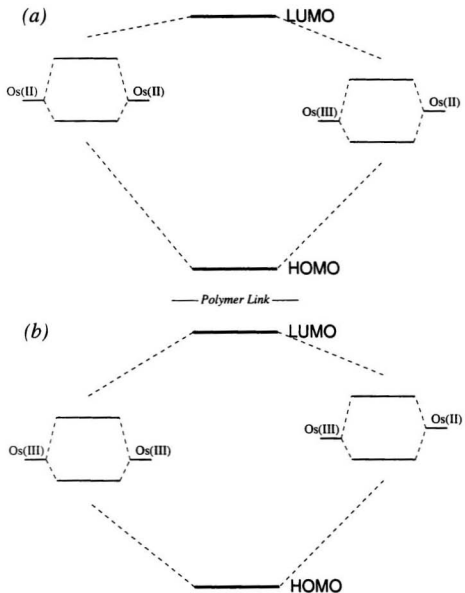


Figure 5.18: Proposed energy level schematic of **Os-PPzBBIM** in the (a) $[\text{Os(II)Os(II)}]\text{-poly-}[\text{Os(II)Os(III)}]$ and the (b) $[\text{Os(III)Os(III)}]\text{-poly-}[\text{Os(II)Os(III)}]$ states. Not drawn to scale

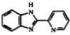
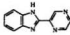
			
	32	62	
HOMO	-751.5	-770.1	kJ/mol
LUMO	213.3	173.8	kJ/mol

Table 5.2: HF/6-31G*//HF/3-21G energies of the HOMO and LUMO of the indicated compounds

greater communication when the higher energy Os(II) is the dominant redox state, the superexchange must occur via the π^* molecular orbital (electron-type superexchange mechanism). This is an interesting finding since Haga has proposed [61] on the basis of *ab initio* calculations that hole superexchange is the dominant mechanism in the dinuclear ruthenium complexes of model compound **34** and its thiazole analogue. This divergence is not surprising since the electronic energy of Os(III/II) is higher than that of Ru(III/II), and the additional electron deficient C=N in the pyrazine should lower the LUMO to some extent. For the pair of isoelectronic compounds indicated in table 5.2, the introduction of the second imine bond lowers the calculated LUMO energy by 39.5 kJ/mol while the HOMO drops by only 18.6 kJ/mol.

It is notable since it establishes that the benzimidazole backbone provides an efficient intermetal communication channel for both superexchange mechanisms. Moreover, the relationship between conductivity and metal centre electronic energy implies that careful selection of ancillary ligands can provide a means of custom tailoring the strength of the interactions. Such coordination-induced conductivity change has potential applications in molecular wire sensors [80]. The use of fairly labile systems of ancillary ligands would open up the intriguing possibility of a concentration controlled molecular potentiometer. Changing the electronic nature of the polymer backbone too

Polymer	$D_e/\text{cm}^2\cdot\text{s}^{-1}$	# of trials	Conditions
Ru-PPyBBIM	2.7×10^{-9}	(3)	MeCN, HClO_4
Ru-PPyBBIM	3.9×10^{-8}	(3)	MeCN, Bu_4NOH
Ru-PPzBBIM ^a	8.5×10^{-9}	(1)	2:1 CH_2Cl_2 :MeCN, HClO_4
	8.5×10^{-9}	(1)	
Os-PPzBBIM	1.3×10^{-8}	(2)	2:1 CH_2Cl_2 :MeCN, HClO_4
	7.0×10^{-9}	(2)	

^a Sum of both waves gives $D_e = 1.7\times 10^{-8} \text{ cm}^2\cdot\text{s}^{-1}$

Table 5.3: Summary of sandwich electrode results in electrolyte solutions comprising the indicated solvent system containing ca. 0.1 M Et_4NClO_4 and a few drops of either conc. HClO_4 or Bu_4NOH in MeOH.

should affect the metal interactions. Lowering the LUMO by adding electron withdrawing substituents to **Os-PPzBBIM**, at the imidazole N-H for example, could test the hypothesis of electron type superexchange in this system.

Sandwich electrode results are summarized in table 5.3.

5.4 Impedance Methods

5.4.1 Background

The third technique used to measure D_e is impedance spectroscopy. This powerful technique was first applied to a conducting polymer (polypyrrole) by Bard and coworkers [150] and has proven to be very versatile [24, 32]. One feature of impedance as it relates to the polymers of interest here is that it permits the measurement of the electronic resistance of the film, a quantity related to D_e . A comprehensive derivation of the theory as applicable to conducting polymers is given by Albery and Mount [151], and a few of the salient features will be summarized here.

The characteristic complex plane (Nyquist) impedance plot of the response of a conducting polymer is presented as an idealized diagram in Figure 5.19. Two distinct regions are evident: A low frequency vertical region and a high frequency 45° region whose origin stems from a diffusion process — electronic or ionic — within the

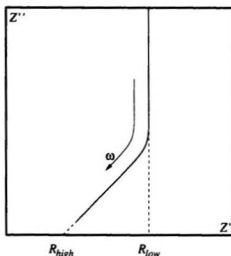


Figure 5.19: Ideal conducting polymer impedance response

film. The dual rail finite transmission line, Figure 5.20 has been proposed [152] as an equivalent circuit to model the physical behaviour of the polymer. The components of this hypothetical electrical circuit correspond to real physical phenomena. A row of capacitors bridging the pair of resistance rails accounts for the Faradaic capacitance (C_F) of the system, while the resistance rails are assigned to the electronic resistance (R_e) and the ionic resistance (R_i) of the coating. An additional resistor has been included to describe uncompensated solution resistance (R_s), an experimental artifact. A useful advantage of impedance spectroscopy is that R_e and R_i are separable, which for example permits its use in the investigation of the influence of the counterion in the rate of electron hopping [32].

At the high frequency limit, the impedance of C_F becomes negligible and the transmission line behaves like two resistances in parallel:

$$\frac{1}{Z} = \frac{1}{R_i} + \frac{1}{R_e} \quad (5.13)$$

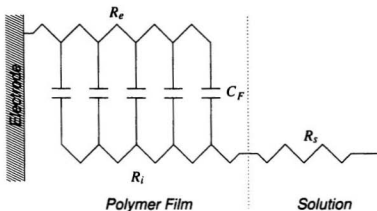


Figure 5.20: Finite transmission line in series with an uncompensated solution resistance

The extrapolation of the 45° region to the real axis in the Nyquist plot gives as the intercept:

$$R_{high} = R_s + \frac{1}{1/R_i + 1/R_e} \quad (5.14)$$

The low frequency response of the transmission line is described by equation 5.15.

$$Z = \frac{R_\Sigma}{3} - \frac{i}{\omega C_F} \quad (5.15)$$

where $R_\Sigma = R_i + R_e$. The real impedance is theoretically constant at all frequencies but in practice this portion of the plot is not quite vertical (see for example Figure 5.21). The real axis intercept of the low frequency data gives

$$R_{low} = R_s + R_\Sigma/3 \quad (5.16)$$

When $R_i \ll R_e$, R_e is approximated by the difference between the real impedance intercepts of these two regions:

$$R_e = 3(R_{low} - R_{high}) \quad (5.17)$$

The effective electron diffusion coefficient can be extracted from the impedance data through equation 5.18 [153]:

$$D_e = d^2 / R_e C_{low} \quad (5.18)$$

where d is the film thickness, as described in section 5.1, and C_{low} is the low frequency capacitance, which can be obtained as the inverse slope of a plot of imaginary impedance Z'' against reciprocal frequency (in rad s^{-1}) for the low frequency data.

5.4.2 Experimental Details

Polymer complex films were cast from solution onto Pt disc electrodes ($A = 0.0052$ – 0.0078 cm^2) as described previously. Coated electrodes were allowed to soak in the appropriate electrolyte solution which had been degassed with Ar, for ca. twenty minutes prior to the commencement of electrochemical experiments. A blanket of Ar or N_2 was used to exclude oxygen and atmospheric water. $E_{1/2}$ was determined by a single cyclic voltammetric sweep at moderate speeds, usually 100 mV/sec , before the impedance investigation, and Γ was determined by slow cyclic voltammetry afterwards. Impedance data was collected at room temperature using a Solartron 1250 frequency response analyzer and a Solartron 1286 potentiostat/galvanostat under the control of ZPlot software. The perturbation amplitude was 5 mV .

5.4.3 Results

Representative complex plane impedance plots of films of **Ru-PPyBBIM** are presented in Figure 5.21 for the cases where the electrolyte solutions had been treated with either acid or base. At the films' formal potentials, 1.2 V and 0.775 V respectively, the response clearly exhibits the 45° Warburg region in addition to the nearly vertical low frequency capacitive impedance. The failure to reach constant real impedance in this region is well known; possible reasons for this finite slope in

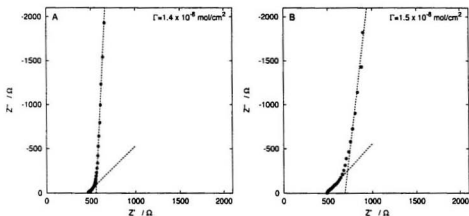


Figure 5.21: Complex plane impedance of a 0.0052 cm^2 Pt disc electrode coated with **Ru-PPyBBIM** in CH_3CN containing $0.1 \text{ mol dm}^{-3} \text{ Et}_4\text{NClO}_4$, containing (A) HClO_4 , and (B) Bu_4NOH

the low frequency range have been discussed by Rubinstein *et al.* [154] and Láng and Inzelt [155]. Capacitance is obtained from the plot of Z'' vs. $1/\omega$ as described in section 5.4.1 and shown as an example in Figure 5.22

It is important to establish that the Warburg-type region is due to electronic diffusion effects as opposed to ionic motion in the film; this same response is evident in systems where $R_e \ll R_i$, for example in electrodes for use in fuel cell development [156, 157]. However when the dominant resistance corresponds to ionic diffusion or migration, the projection of the 45° region onto the real impedance axis changes little with potential [152]. Figure 5.23 indicates that the process responsible for the dominant resistance in these systems is indeed potential dependent, and that R_e is smallest at the formal potential, as is expected for resistance stemming from D_e .

The smaller ionic resistance can be isolated from R_{high} if R_i is known. This parameter is measured as the real impedance intercept of an uncoated electrode positioned in the same location in the cell as the coated electrode. The difference between this

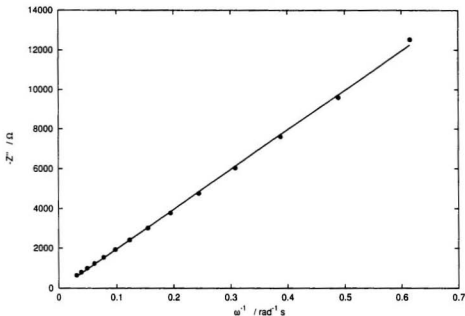


Figure 5.22: Representative Z'' vs. $1/\omega$ plot for the determination of C_F using the data from Figure 5.21A

intercept and the high frequency intercept of the coated electrode gives R_t as illustrated in Figure 5.24. For the present **Ru-PPyBBIM** example, rigorously solving for the two resistances by equations 5.14 and 5.15 gives $R_e = 1357 \Omega$ and $R_t = 18 \Omega$. The approximation of equation 5.17 gives $R_e = 1375 \Omega$. Clearly the approximation is valid, and is advantageous in that it does not require the added complication of measuring R_s . The relative error introduced by the approximation in this example is around 1%, which is comparable in most cases to the uncertainties introduced from the extrapolations. This finding is also important in that it proves that disregarding the contribution of ion transport to D_{CT} (see section 1.3) in these films is justified.

Impedance spectra in the mixed solvent system (2:1 CH_2Cl_2 :MeCN v/v acidified

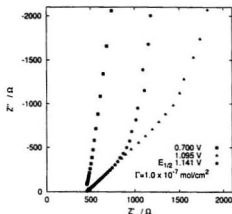


Figure 5.23: Impedance response as a function of potential in a **Ru-PPyBBIM** film on a 0.0052 cm^2 Pt disc electrode in CH_3CN containing $0.1 \text{ mol dm}^{-3} \text{ Et}_4\text{NClO}_4$ containing HClO_4

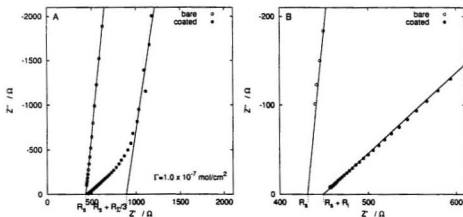


Figure 5.24: (A) Complex plane impedance for a bare Pt disc electrode and one coated with **Ru-PPyBBIM** in CH_3CN containing $0.1 \text{ mol dm}^{-3} \text{ Et}_4\text{NClO}_4$ acidified with HClO_4 . (B) Zoomed area from (A)

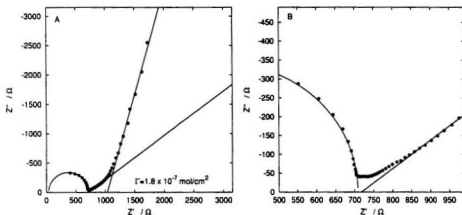


Figure 5.25: (A) Complex plane impedance spectrum of **Ru-PPyBBIM** in the mixed solvent system 2:1 CH_2Cl_2 :MeCN containing ca. 0.1 mol dm^{-3} TEAP and acidified with HClO_4 . (B) Zoomed area from (A)

with HClO_4) show the added complication of a high frequency partial semicircle. An example of this phenomenon is shown in Figure 5.25 for a **Ru-PPyBBIM** film. Similar responses were seen for **Os-PPzBBIM** and **Ru-PPzBBIM**.

This effect can be attributed to the small geometric capacitance C_g present in all cells. The equivalent circuit in Figure 5.26 shows how C_g shunts the transmission line at high frequencies. The extrapolated semicircle in Figure 5.25 does go to (nearly) zero.

C_g may be evaluated from the semicircle geometry. In these systems, it turns out that its value is consistently ca. $4 \times 10^{-7} \text{ F/cm}^2$, a capacitance much smaller than what would be expected for the double layer capacitance in a charge transfer kinetics problem. In some cases the mixing of the C_g shunt with the transmission line obscured the 45° region of the spectrum, making extrapolation impossible. However, the low frequency intercept of the semicircle can be used to determine R_s . This provides a sufficient approximation of R_{high} since R_i can be safely disregarded. Figure 5.25B

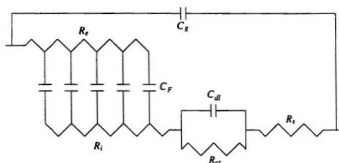


Figure 5.26: Equivalent circuit for C_g effects observed in mixed solvent electrolyte solutions

shows a 45° region which was not obscured, and how its real impedance intercept closely matches that of the low frequency side of the semicircle.

Impedance methods hold two distinct advantages over the other techniques used to measure D_e . Firstly, the experiments are technically far simpler; tedious gold vapour deposition and fragile, unreliable RDV films are avoided. Secondly, the duration of an impedance experiment holds an additional advantage in these systems where extended exposure to elevated potentials can lead to stability issues. A typical impedance full run may last a minute, compared to several minutes per sweep in a mediated RDV experiment. Indeed the long duration of the high potential exposure in standard mediated RDV experiments required the development of the limiting current prediction approach described earlier in section 5.2.4. The impedance spectrum is measured at $E_{1/2}$, exposing the film to moderate potentials only. Impedance spectroscopy is prone to film degradation nonetheless. Figure 5.27 shows the Nyquist plots of three successive impedance scans on the same film. The trend of the low frequency vertical region to greater resistance and elongation of the 45° region indicates increasing R_e , and hence decreasing D_e . This performance degradation, even under the relatively

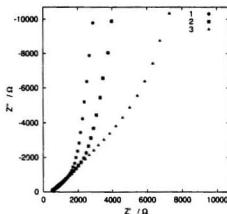


Figure 5.27: Degradation in three successive complex plane impedance spectra of a film of **Ru-PPyBBIM**, measured at $E_{1/2}$ in CH_3CN containing 0.1 mol dm^{-3} Et_4NClO_4 and acidified with HClO_4

mild conditions of an impedance experiment, underlines the fragile nature of the films' electroactivity and the difficulty in recording D_e reliably.

A complete table of impedance results is given in table 5.4. The two entries for **Ru-PPyBBIM** in the table indicate an important result. Here, impedance data for two samples of this polymer are shown, sample (a) having approximately 60% site occupancy by Ru, and sample (b) having nearly 85% occupancy on the basis of elemental analyses. In spite of this difference, D_e turns out to be very similar for the two, with sample (a) having a slightly lower rate of electron transport. If the contribution of the lower concentration of metal in the film were to be considered (see equation 5.2) these values would be closer still. The similarity of D_e in these two films indicates different average intermetal separation distances does not have a significant influence over D_e , at least at moderate loading. This is important since other charge transfer mechanisms (*e.g.*, outer sphere electron transfer) should exhibit a strong dependence on the average intermetal separation.

POLYMER	ACID		BASE	
	$D_e / \text{cm}^2 \cdot \text{s}^{-1}$	s	$D_e / \text{cm}^2 \cdot \text{s}^{-1}$	s
Ru-PPyBBIM ^a	4.9×10^{-9}	2.7×10^{-9}	1.0×10^{-8}	3.0×10^{-10}
Ru-PPyBBIM ^b	6.6×10^{-9}	3.2×10^{-9}		
Os-PPyBBIM	3.1×10^{-9}	1.8×10^{-9}	1.0×10^{-9} ^c	—
Ru-PPyBDIM	3.8×10^{-9}	0.3×10^{-9}		
Ru-PPzBBIM (1)	3.0×10^{-9}	0.9×10^{-9}		
Ru-PPzBBIM (2)	7.9×10^{-9}	8.6×10^{-9}		
Os-PPzBBIM (1)	8.5×10^{-9}	5.3×10^{-9}		
Os-PPzBBIM (2)	6.3×10^{-9}	4.6×10^{-9}		

^{a,b} Two different **Ru-PPyBBIM** samples

^c Single result

s = standard deviation

Table 5.4: Summary of impedance results. **PPyBBIM** and **PPyBDIM** complexes used an acetonitrile solution, while **PPzBBIM** complexes used 2:1 CH_2Cl_2 :MeCN mixed solvent. All solutions contained ca. 0.1 M Et_4NClO_4 , and those in columns ACID or BASE also contained ca. 50 mM HClO_4 or 5 mM Bu_4NOH respectively. The lower and higher potential waves of **Ru-PPzBBIM** **Os-PPzBBIM** are denoted by (1) and (2) respectively.

5.5 D_e Conclusions

A complete summary of electron diffusion coefficient data is compiled in table 5.5 along with literature values for similar polymer complexes in which the metal is not bound directly to a long range conjugation network. In cases where sufficient data is available, excellent correlation between the three experimental methods is seen. The present set of results validates impedance spectroscopy as a fast and reliable way to measure charge transport in polymer films. In 1992, a review stated that for ac impedance "more widespread use may be expected in the future because of the quality of the data obtained." [160] but this has not been the case.¹ Other techniques such as cyclic voltammetry, potential step methods, dual electrode voltammetry and rotating disc electrode voltammetry have continued to be popular, possibly due to their more

¹The use of impedance spectroscopy was criticized by the reviewers of our preliminary report [44]

Polymer	Conditions	Electron Diffusion Coefficient / cm ² ·s ⁻¹					
		Impedance		Sandwich		RDV	
		<i>D_e</i>	<i>s</i>	<i>D_e</i>	<i>s</i>	<i>D_e</i>	<i>s</i>
Ru-PPyBBIM	A,C	5.9×10 ⁻⁹	3.0×10 ⁻⁹	3.5×10 ⁻⁹	1.9×10 ⁻⁹	3.2×10 ⁻⁹	2.8×10 ⁻⁹
Ru-PPyBBIM	A,D	1.0×10 ⁻⁸	3.0×10 ⁻¹⁰	4.5×10 ⁻⁸	2.1×10 ⁻⁹		
Ru-PPyBDIM	A,C	3.8×10 ⁻⁹	0.3×10 ⁻⁹			1.3×10 ^{-9 a}	
Ru-PPzBBIM (1)	B,C	3.0×10 ⁻⁹	0.9×10 ⁻⁹	8.5×10 ^{-9 a}			
Ru-PPzBBIM (2)	B,C	7.9×10 ⁻⁹	8.6×10 ⁻⁹	8.5×10 ^{-9 a}			
Os-PPyBBIM	A,C	3.1×10 ⁻⁹	1.8×10 ⁻⁹	2.4×10 ^{-9 a}		6.3×10 ^{-10 a}	
Os-PPyBBIM	A,D	1.0×10 ^{-9 a}					
Os-PPzBBIM (1)	B,C	8.5×10 ⁻⁹	5.3×10 ⁻⁹	1.3×10 ⁻⁸	0.6×10 ⁻⁸	2.3×10 ^{-8 a}	
Os-PPzBBIM (2)	B,C	6.3×10 ⁻⁹	4.6×10 ⁻⁹	7.0×10 ⁻⁹	2.6×10 ⁻⁹		
Poly-[Ru(bpy) ₂ (pmp) ₂] ²⁺ [158]	E			1.2×10 ⁻⁹	0.5×10 ⁻⁹	2.6×10 ⁻¹⁰	4.5×10 ⁻¹⁰
Poly-[Ru(bpy) ₂ (vpy) ₂] ²⁺ [136]	A			7.2×10 ⁻¹⁰	0.4×10 ⁻¹⁰		
Poly-[Ru(vbpy) ₃] ²⁺ [159]	A			2.2×10 ⁻¹⁰			
Poly-[Os(bpy) ₂ (vpy) ₂] ²⁺ [136]	A			7.2×10 ⁻⁹	3.5×10 ⁻⁹		
Poly-[Os(bpy) ₂ (pyam) ₂] ²⁺ [145]	A			1.5×10 ⁻⁹	0.9×10 ⁻⁹		

A Acetonitrile containing ca. 0.1 M Et₄NClO₄

B 2:1 Dichloromethane:acetonitrile containing ca. 0.1 M Et₄NClO₄

C Acidic: contains ca. 50 mM HClO₄

D Basic: contains ca. 5 mM Bu₄NOH

E Acetonitrile containing ca. 0.1 M Bu₄NClO₄

s = standard deviation

^a Single result

Table 5.5: Summary of *D_e* and selected literature results

obvious connections to diffusion through the adaptation of classic electrochemical finite and semi-infinite diffusion models. Conductivity measurements have also been used to gauge metal interactions in polymers with conjugated backbones [52, 74, 80]. Impedance theory has shown the relationship between resistance and D_e , however conductivity is deficient in that it cannot separate R_e from R_i or other resistance influences. Nevertheless conductivity methods are ideally suited to sensor applications.

Important trends are evident in table 5.5.

1. Acid-base effects. In earlier chapters, the influence of supporting electrolyte solution pH on the polymers' and polymer complexes' electrochemistry was noted. The effects are also evident in D_e measurements. In films of **Ru-PPyBBIM** a tenfold increase in the rate of electron diffusion is evident when the solution is treated with base rather than acid. This is important since it clearly shows that metal-metal interactions along the length of the polymer can be modulated by the electron density on the backbone, as effected by the removal of the imidazole proton. This result echoes Haga's work with dinuclear benzimidazole complexes [62, 63] and extends it into the new context of an infinite framework.
2. Chain defects. Incomplete ring closure leading to polymer defects and branching were discussed in section 3.3, and it was shown that the rigid rod polymer **PPyBDIM** was particularly prone to this problem. It is not surprising that D_e for **Ru-PPyBDIM** is somewhat smaller since the parent polymer is more prone to structural anomalies. Evidently disruption of the conjugation by structural defects has an adverse effect on the overall efficiency of charge transport in the system. While tests on a highly defective polymer might have continued this trend, the increased loss of rigidity could lead to additional complications, such as the contribution of direct outer-sphere self-exchange between nearby

Ru atoms which would otherwise have been firmly held apart. Retardation of electron transport in the more defective polymer lends support to the view that long range conjugation is intimately connected to the charge transport mechanism in these systems.

3. HOMO-LUMO and metal orbital energy gaps: In section 5.3.3 it was postulated that the greater D_e associated with the first redox wave in **Os-PPzBBIM** is indicative of an electron-type superexchange mechanism owing to a more favourable energy match. Similar interactions could account for trends in other systems. While the proximity of the waves in **Ru-PPzBBIM** made measurements difficult, it appears that this polymer exhibits similar or slightly smaller D_e than **Ru-PPyBBIM**. This is consistent with the slight lowering of the HOMO energy (see table 5.2) in the pyrazine polymer, rendering the hole-type superexchange somewhat less favourable. Similarly, D_e in **Os-PPyBBIM** is lower than in **Ru-PPyBBIM** because the higher electronic energy of the metal makes hole superexchange more difficult. One would therefore expect **Os-PPzBBIM** to exhibit D_e lower than both **Ru-PPzBBIM** and **Os-PPyBBIM**; the opposite is true, which provides further evidence that the alternate pathway, electron-type superexchange, must be the dominant mechanism in **Os-PPzBBIM**.

The most significant result is the great enhancement of D_e in these systems compared to the similar non-conjugated materials listed in table 5.5. Improvements of between one and two orders of magnitude are evident. These results are encouraging, since very significant improvements in electron transport rates can be seen in systems which were not specifically designed to optimize the metal-polymer energy

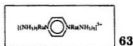
overlap. The recently reported phenomenon of enhanced conductivity in metallopoly-
mers where the redox potentials of the metal and the organic backbone partially over-
lap [52] can be taken as a trivial example of the relationship between orbital energies
and electroactivity postulated here. There is clear evidence that more deliberate con-
trol of the HOMO or LUMO energies of the polymer backbone, perhaps by means
of added substituents, should lead to electron transport even more rapid than that
exhibited by the prototype systems in this project.

CHAPTER 6

INTERVALENCE TRANSFER BANDS

6.1 Introduction

The essence of the self-exchange electron transfer (ET) reaction is the valence interchange of two constitutionally identical ions of differing oxidation states [56]. The details of intramolecular ET between two nearby metal atoms through a bridging ligand are of obvious consequence to the mechanism of charge transport in the polymer systems of interest here. Substitution-inert mixed valence complexes, such as the archetype Taube-Creutz ion **63** [132] have been instrumental in the elucidation of many important aspects of ET as described by the Marcus theory of outer-sphere ET [56, 161] and the Hush theory of mixed-valence complexes [162]. While the optical qualities of photoinduced electron transfer have no direct bearing upon the polymer systems' electrochemistry, they are still useful in that they help to describe the strength of the metal-metal interactions which in turn does influence the electrochemistry.



A brief overview of the origins and significance of intervalence transfer bands as they apply to conjugated polymer hybrids is presented here. More detailed accounts are found elsewhere [56, 162–164]

The Franck-Condon principle implies that in the course of ET, the atomic positions remain unchanged; the transfer of the electron can be regarded as quasi-instantaneous with respect to nuclear motion. In the special case of a symmetric mixed valence compound containing metal centre M and its one-electron oxidation product M^+ and bridged by ligand L, $M-L-M^+$, *e.g.*, **63**, the interconversion of the two energetically degenerate forms depicted in equation 6.1 with no net free energy change is subject to a thermal activation barrier ΔG_{th}^* .

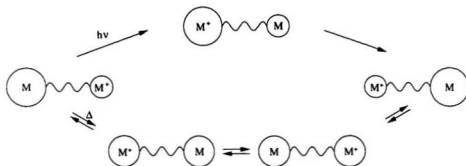


Figure 6.1: Thermal and optical ET processes in a symmetric mixed valence complex



In general, the metal-ligand bond lengths and force constants, and metal-solvent electrostatic interactions will be different around M and M^+ . The interchange of charge therefore necessitates the reorganization of the inner-shell and outer-shell environments. The energy of this reorganization is related to the ET activation barrier. This is the essence of the Marcus model. The consequences of the net nuclear rearrangement are depicted in Figure 6.1, where the circles represent the corresponding geometry of the coordination sphere and solvation around the metal centre. If spontaneous ET were to occur between M and M^+ in their equilibrium states, the product would be formed in a vibrationally excited state, with M having the M^+ configuration and vice-versa. This violates conservation of energy, and is depicted by the thermally forbidden upper reaction pathway in Figure 6.1. For ET to occur, the ligands and solvent must rearrange to a compatible configuration before the ET step. The formation of this activated complex in which ET takes place constitutes the thermal barrier, and is depicted by the lower pathway in Figure 6.1.

ET without prior rearrangement can be induced along the upper pathway by the absorption of light sufficiently energetic to form the excited state; it is this light absorption that gives rise to the intervalence transfer (IT) band. The energy relationships are demonstrated in Figure 6.2 as potential energy curves where one parabola describes each of $M - L - M^+$ and $M^+ - L - M$. The curves split at the intersection by $2H_{AB}$, where H_{AB} is a resonance energy between the states, *i.e.*, the electronic coupling between the two redox centres. In thermal ET, the system moves from left to right, passing over the barrier E_{th} . Optical ET occurs when sufficiently energetic light $h\nu = E_{op}$ is absorbed, effecting vertical passage from the lower to the upper curve. When H_{AB} is small and $E_{th} = \Delta G_{th}^*$, it turns out that optical and thermal ET are proportional:

$$E_{op} = h\nu = 4\Delta G_{th}^* \quad (6.2)$$

The nature of the IT band is related to the strength of the metal-metal interactions by the Hush theory. H_{AB} (in cm^{-1}) may be evaluated with equation 6.3 from the charge transfer band's position (ν_{max}), half-height width¹ ($\Delta\nu_{1/2}$), and intensity (ϵ_{max}) in cm^{-1} , and the intermetallic separation r in Å:

$$H_{AB} = 2.05 \times 10^{-2} \left[\frac{\epsilon_{max} \Delta\nu_{1/2}}{\nu_{max}} \right]^{1/2} \left[\frac{\nu_{max}}{r} \right] \quad (6.3)$$

A system of classifying mixed valence compounds on the basis of the interactions between the metal centres has been devised by Robin and Day [165]. In a class I mixed valence complex the interaction is so weak (for reasons such as large physical separation or very different environments) that it can be considered non-existent and only the properties of the discrete ions is observed. $H_{AB} = 0$ and the two potential energy profiles (see Figure 6.2) intersect. In class III the extreme opposite is found, where the coupling is so strong that the characteristics of isolated M and M^+ are

¹ where $\epsilon/\epsilon_{max} = 1/2$

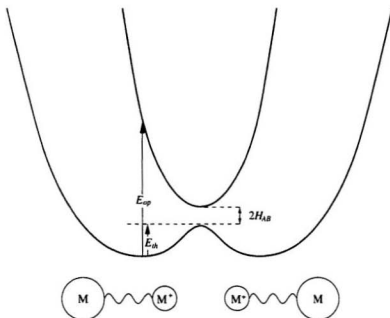


Figure 6.2: Electron transfer in symmetrical mixed-valence systems

absent, replaced by the new properties of a completely delocalized $(M-M)^+$ unit (*e.g.*, **63**). The energy profiles coalesce; Hush theory is not applicable. Class II materials exhibit characteristics of weak coupling, with slightly perturbed M and M^+ character. Typically $\Delta E^0 < 200$ mV. It is for this class that the Hush model is useful. Increases in H_{AB} result in a lowering of E_{th} to the point where there is no thermal barrier and only one minimum exists: a class III compound. Borderline cases may be difficult to assign, although a number of criteria can be invoked to support an assignment. For the present benzimidazole systems, all mixed valence complexes for which an IT band was measured certainly belong to class II.

It should be emphasized at this point that the timescale of the ligand rearrangements associated with ET is much shorter than the timescale of the electrochemistry

experiments. These rearrangements do not interfere with the highly electrochemically reversible nature of $\text{Ru}(\text{bpy})_3^{3+/2+}$ type reactions. (The heterogeneous ET rate constant of $\text{Ru}(\text{bpy})_3^{3+/2+}$ in DMF at Pt has been reported as 0.24 cm s^{-1} [166, 167].)

6.2 Experimental

The apparatus used to measure the IT spectra is shown in Figure 6.3.

A slide of conducting indium-tin oxide (ITO) coated glass (Donnelly Corp.) was cut to appropriate dimensions and carefully cleaned with methanol and dried. A relatively thick film of the polymer complex was cast onto the slide at the location where the spectrometer beam would pass through it. The slide was then positioned inside a standard 1 cm quartz UV-vis spectroscopy cuvette, polymer side towards the cuvette wall. A *ca.* 0.11 mm plastic spacer² maintained a slight gap between the cuvette wall and the slide. This gap permitted the polymer film to be bathed by electrolyte solution which could creep up the wall from a pool in the bottom of the cuvette, the level of which was kept below the spectrometer beam. It had been found previously that the electrolyte solution, CH_3CN containing $0.1 \text{ mol dm}^{-3} \text{ Et}_4\text{NClO}_4$, has absorptions in the NIR in the region where the IT bands would be expected. Absorption through the full length of the cell (1 cm) resulted in unmanageable spectrometer dark noise. The short path length of the gap (0.11 mm) made the solvent absorptions insignificant.

A Pt wire counter electrode and a Ag/AgCl reference electrode (*vide infra*) were added to the cuvette and positioned so as not to interfere with the light beam. The three electrodes were secured in place with alligator clips and a small volume of electrolyte solution (CH_3CN containing $0.1 \text{ mol dm}^{-3} \text{ Et}_4\text{NClO}_4$ and *ca.* 50 mmol dm^{-3}

²In order to form an appropriate gap, several approaches were explored. This ranged from using a pair of mechanical pencil leads to an elaborate cell insert made from machined plastic. The successful plastic spacers employed here were fashioned with a razor blade from Aldrich product shipping bags.

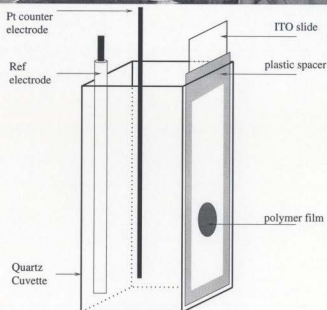
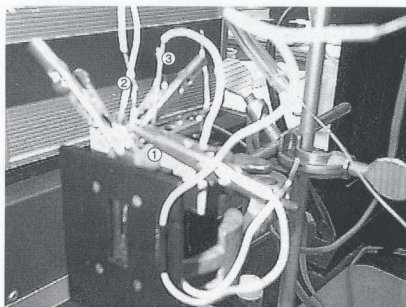


Figure 6.3: Experimental apparatus for measuring IT bands in **Ru-PPyBBIM** films. In the upper figure, an operational cell is pictured in a spectrometer cuvette holder (1) ITO electrode (2) reference electrode (3) counter electrode

HClO₄) was added. $E_{1/2}$ was measured as the average of E_{pa} and E_{pc} as determined by slow cyclic voltammetry, then the cuvette assembly was transferred to the sample beam of a Cary 5E UV-vis-NIR spectrometer. A similar assembly, without polymer, was positioned in the reference beam. Wires leading between the cell and the potentiostat were carefully secured so as to avoid any motion of the cell; owing to the irregular thickness of the polymer deposit, any disruption of the cell would change its absorption characteristics. The spectrometer compartment lid switch was defeated to allow the wires to pass through an opening; added precautions were taken to prevent stray light from entering the sample compartment.

Spectra were acquired over the 400–2500 nm range with 1 nm resolution. Baseline correction was not applied. The polymer film was held in its reduced state at $E \ll E_{1/2}$, typically 0.8 V, until consecutive spectra showed stability over a fifteen minute interval. Spectra were acquired at $E_{1/2}$ and at $E \gg E_{1/2}$, allowing a stabilization period of at least fifteen minutes after every potential change. Replicate spectra were taken to ensure stability.

The constrained space of this assembly required a very thin reference electrode. These were constructed from short lengths (ca. 4 cm) of 0.050" O.D. polyethylene tubing. One end of the tube was dipped in a solution of Nafion in alcohol and allowed to dry overnight, leaving a small plug. The tube was carefully filled with 1 M aqueous KCl using a microsyringe, and the Nafion plug was soaked in a pool of the filling solution overnight. A thin Ag wire which had been previously treated by electrochemical oxidation in a chloride solution was added. This electrode was shown to provide a continuously stable reference potential against ferrocene while immersed for periods in excess of 24 hours.

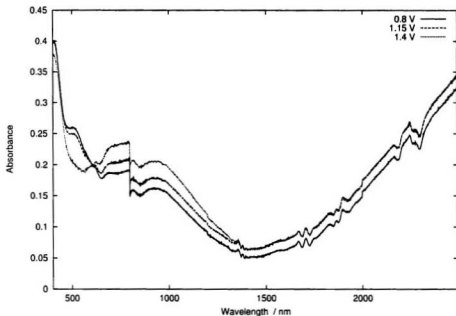


Figure 6.4: Raw UV-vis-NIR spectra of **Ru-PPyBBIM** on an ITO electrode

6.3 Results

Typical raw spectra are presented in Figure 6.4. The optical inhomogeneity of the assembly has resulted in a spectrum with an irregular noisy baseline. Fortunately it has been generally found that the M(II) state is transparent in the near infrared for Ru and Os complexes with benzimidazoles [61–63]. Consequently the spectrum of the fully reduced form can be utilized as a background. Subtraction of this background spectrum from the half oxidized ($E = E_{1/2}$) and from the fully oxidized ($E \gg E_{1/2}$) spectra gives new corrected spectra as shown in Figure 6.5. It is from these *difference* spectra that the intervalence charge transfer may be observed. The direct subtraction of half of the fully oxidized spectrum from the half oxidized spectrum shows a distinct

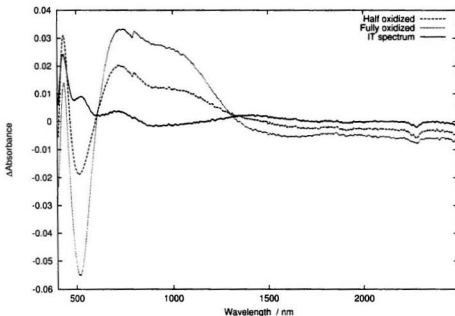


Figure 6.5: Difference spectra of half- and fully oxidized forms, and IT spectrum from a film of **Ru-PPyBBIM**

band centred around ca. 1400 nm, also shown in Figure 6.5. This band can be assigned to an IT transition since it only appears in the mixed valence (half oxidized) state.

Figure 6.6 shows the IT band expressed in cm^{-1} and its fit with a gaussian curve. The absorption maximum wavenumber, ν_{max} , and the half-intensity bandwidth, $\Delta\nu_{1/2}$, are easily determined. The intensity of the band, ϵ_{max} , is nearly impossible to determine directly since the effective pathlength (*i.e.*, film thickness) cannot be measured easily. It was pointed out in section 4.2.3.2 that the Ru(II) $d \rightarrow \text{polymer } \pi^*$ MLCT band near 500 nm becomes bleached as the polymer is oxidized (see Figure 4.3 on page 104). This loss of absorbance is also evident in Figure 6.5. This phenomenon

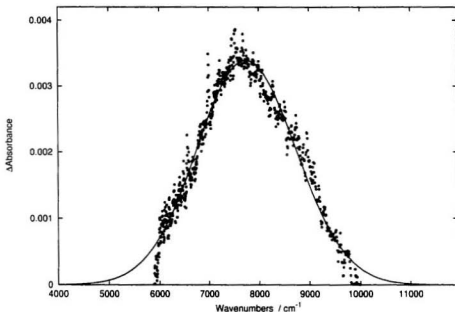


Figure 6.6: IT band and gaussian curve fit

is important as it can be exploited to find the IT band ϵ_{max} . The extinction coefficient of the MLCT band had been measured in solution previously, isolated from the adjoining strong $\pi \rightarrow \pi^*$ absorption by gaussian curve fitting. $\epsilon_{max}(\text{MLCT})$ can be taken to be equal in magnitude to the bleached band in the fully oxidized difference spectrum in Figure 6.5. The bleached MLCT band relates absorbance and ϵ , providing a gauge against which the absorbance of the IT band may be compared.

The estimated distance between metal sites r in model compound **42** has been reported [62] to be 12–15 Å on the basis of molecular models. For the polymers, it was assumed that $r = 15$ Å. Equation 6.3 can be employed to evaluate the degree of electronic coupling in the polymer complexes.

Complex	ϵ_{max} (L·mol ⁻¹ cm ⁻¹)	ν_{max} (cm ⁻¹)	$\Delta\nu_{1/2}$ (cm ⁻¹)	H_{AB} (cm ⁻¹)
Ru-PPyBBIM film 1	62	7742	2320	46
Ru-PPyBBIM film 2	125	7294	2291	62
Os-PPyBBIM	41	6645	1095	24
Ru model [62]	< 100	7300	3100	60–80
Os model [62]	< 20	9100	3020	30–40

Table 6.1: Electronic coupling H_{AB} calculated from IT data for **Ru-PPyBBIM** and **Os-PPyBBIM** and model complexes

Table 6.1 summarizes experimental IT results for the polymers **Ru-PPyBBIM** and **Os-PPyBBIM** along with literature data for the corresponding dinuclear complexes of model compound **33**. For symmetric mixed valence species, theory predicts a relationship between ν_{max} and $\Delta\nu_{1/2}$ [163]:

$$\Delta\nu_{1/2} = [2310 \nu_{max}]^{1/2} \quad (6.4)$$

in units of cm⁻¹. Neither the polymer nor the literature results follow the prediction particularly well, with errors between 25% and 45% and somewhat more for **Os-PPyBBIM** (this could be in part a reflection of the difficulty in measuring the band for this polymer). Reasons for this are unclear but they might be a manifestation of non-symmetry in the systems as proposed in the original theory [162, 163]. Consequently, values calculated for the degree of electronic coupling between neighbouring metal sites H_{AB} may be somewhat unreliable, but since the discrepancy is similar between the polymers and the model compounds, comparisons between the two should still be valid. H_{AB} in the polymers is in good agreement with that found in the dinuclear complexes, indicating that the interactions between these sites are comparable in both systems. This is important because it demonstrates (i) that synthetically less sophisticated model compounds can be useful to test the design of future polymer systems with more advanced electron transport properties, and (ii)

that binuclear complexes already known to have strong coupling can be expected to produce good performance when extended into a polymeric system. This point justifies the original choice of benzimidazole-based structures for this project.

While the optical property of intervalence transfer bands is descriptive of chromophore interactions in the charge transfer state, it should parallel the electrochemistry which is also in essence controlled by the interaction of metal and ligand orbitals. To the best of our knowledge this is the first time that optical intervalence transfer bands have been detected in a metallopolymer. The presence of the IT band helps to substantiate claims that the metal atoms in the metallopolymers of interest here are indeed communicating through the backbone in a manner similar to the well-established inner-sphere electron transfer through bridging ligands in mixed valence complexes [56, 168, 169].

CHAPTER 7

CONCLUSIONS

The results provide compelling evidence that electron transport between redox sites is significantly enhanced when the metal centres are coordinated directly into the π backbone of a conjugated polymer. Conservative calculations put the rates of electron diffusion in the conjugated systems between ten and one-hundred times as fast than in similar polymer systems where saturated segments isolate the metal atoms. The observations that (i) electron transport rates can be manipulated by changing the electron density of the polymer backbone (*i.e.*, by protonation/deprotonation) and (ii) D_e decreases when the polymer backbone is degraded by extended exposure to elevated potentials both indicate that the polymer support does indeed play an intimate role in the long-range transport of charge.

Electron diffusion cannot be ascribed to the π chain alone since the uncomplexed polymers are electrochemically inactive at potentials corresponding to the M(III/II) redox processes in both acidic and basic media. Rather, it is the interaction of metal centres through the backbone that is believed to be responsible. Further evidence of this interaction comes from the intervalence charge transfer bands found in the near infrared spectrum of the polymer complexes in the half-oxidized state. This optically measured communication is comparable to the same well-documented phenomenon found in similar binuclear complexes.

This work marks the first time an attempt has been made to use the conjugated-redox hybrid strategy to build conducting polymers with the specific goal of improving charge transport. The behaviour of these systems appears to involve the orbital energy relationships between the polymer support and the redox-active metal centre. Clearly, a parallel may be drawn between these new conjugated polymer complexes and better known conjugated binuclear complexes. The mode of communication in the polymeric systems can therefore be rationalized as a superexchange mechanism stemming from the orbital interactions of the components involved.

The hybrid approach is validated by the encouraging results obtained from prototype systems where no provisions had been made to optimize the rates of transport. Clearly, a directed effort towards matching the orbital energies of the metal and the polymer support (and thereby improving superexchange) is an important direction for future research. These fascinating materials are excellent candidates for future use in applications where rapid electron transport will be important, such as in efficient solar energy harvesting systems, high performance electrocatalysts, and molecular electronics.

References

- [1] Arnold, Jr., F. E.; Arnold, F. E. *Adv. Poly. Sci.* **1994**, 117, 257.
- [2] Vogel, H.; Marvel, C. S. *J. Poly. Sci.* **1961**, L, 511.
- [3] Techagumpuch, A.; Nalwa, H. S.; Miyata, S. Promising Applications of Conducting Polymers. In *Electroresponsive Molecular and Polymeric Systems*, Vol. 2: Marcel Dekker: New York, 1988.
- [4] Neuse, E. W. *Adv. Poly. Sci.* **1982**, 47, 1.
- [5] Yu, L.; Chen, M.; Dalton, L. R. *Chem. Mater.* **1990**, 2, 649.
- [6] Miller, J. S. *Adv. Mater.* **1993**, 5, 671.
- [7] Skotheim, T.. Ed.; *Handbook of Conducting Polymers*; volume 1. 2 Marcel Dekker: New York, 1986.
- [8] Osaheni, J. A.; Jenekhe, S. A. *Chem. Mater.* **1992**, 4, 1282.
- [9] Roberts, M. F.; Jenekhe, S. A. *Chem. Mater.* **1994**, 6, 135.
- [10] Dotrong, M.; Meheta, R.; Balchin, G. A.; Tomlinson, R. C.; Sinksy, M.; Lee, C. Y.-C.; Evers, R. C. *J. Poly. Sci. Part A* **1993**, 31, 723.
- [11] Osaheni, J. A.; Jenekhe, S. A. *Macromol.* **1995**, 28, 1172.
- [12] Wolfe, J. F.; Sybert, P. D.; Sybert, J. R. U.S. Patents 4,533,692, 4,533,693, 4,533,724,.
- [13] Wolfe, J. F. In *Encyclopedia of Polymer Science and Engineering*, Vol. 11; Wiley: New York, 1986.
- [14] Wolfe, J. F.; Arnold, F. E. *Macromol.* **1981**, 14, 909.
- [15] Wolfe, J. F.; Loo, B. H.; Arnold, F. E. *Macromol.* **1981**, 14, 915.
- [16] Frommer, J. E.; Chance, R. R. In *Encyclopedia of Polymer Science and Engineering*, Vol. 5; Wiley: New York, 1986.
- [17] Ito, T.; Shirakawa, H.; Ikeda, S. *J. Polym. Sci. Chem. Ed.* **1974**, 12, 11.
- [18] Chiang, C. K.; Park, Y. W.; Heeger, A. J.; Shirakawa, H.; Louis, E. J.; MacDiarmid, A. G. *Phys. Rev. Lett.* **1977**, 39, 1098.

- [19] Roncali, J. *Chem. Rev.* **1992**, 92, 711.
- [20] Wilbourn, K.; Murray, R. W. *J. Phys. Chem.* **1988**, 92, 3642.
- [21] Heinze, J. Electronically Conducting Polymers. In *Topics in Current Chemistry*, Vol. 152; Springer-Verlag: Berlin, 1990.
- [22] Chung, T. C.; Kaufman, J. H.; Heeger, A. J.; Wudl, F. *Phys. Rev. B* **1984**, 30, 702.
- [23] Brédas, J.; Chance, R.; Silbey, R. *Phys. Rev. B* **1982**, 26, 5843.
- [24] Pickup, P. G. *J. Chem. Soc. Faraday Trans.* **1990**, 86, 3631.
- [25] Murray, R. W. *Electroanal. Chem.* **1984**, 13, 191.
- [26] Kaneko, M.; Wöhrlé, D. *Adv. Polym. Sci.* **1988**, 84, 141.
- [27] Abruña, H. D. *Coord. Chem. Rev.* **1988**, 86, 135.
- [28] Arana, C.; Keshavarz, M.; Potts, K. T.; Abruña, H. D. *Inorg. Chim. Acta* **1994**, 225, 285.
- [29] Guadalupe, A. R.; Usifer, D. A.; Potts, K. T.; Hurrell, H. C.; Mogstad, A.-E.; Abruña, H. D. *J. Am. Chem. Soc.* **1988**, 110, 3462.
- [30] Hurrell, H. C.; Mogstad, A.-L.; Usifer, D. A.; Potts, K. T.; Abruña, H. D. *Inorg. Chem.* **1989**, 28, 1080.
- [31] Youssoufi, H. K.; Hmyene, M.; Yassar, A.; Garnier, F. *J. Electroanal. Chem.* **1996**, 406, 187.
- [32] Ren, X.; Pickup, P. G. *J. Electroanal. Chem.* **1994**, 365, 289.
- [33] Kaufman, F. B.; Engler, M. B. *J. Am. Chem. Soc.* **1979**, 101, 547.
- [34] Kaufman, F. B.; Schroeder, A. M.; Engler, E. M.; Kramer, S. R.; Chambers, J. Q. *J. Am. Chem. Soc.* **1980**, 102, 483.
- [35] Lyons, M. E. G. Charge Percolation in Electroactive Polymers. In *Electroactive Polymer Electrochemistry*; Plenum Press: New York, 1994.
- [36] Majda, M. Dynamics of Electron Transport in Polymeric Assemblies of Redox Centers. In *Molecular Design of Electrode Surfaces*, Vol. 22; Murray, R. W., Ed.; Wiley: New York, 1992.
- [37] Andrieux, C. P.; Saveant, J. M. *J. Electroanal. Chem.* **1980**, 111, 377.
- [38] Laviron, E. *J. Electroanal. Chem.* **1980**, 112, 1.
- [39] Fritsch-Faules, I.; Faulkner, L. R. *J. Electroanal. Chem.* **1989**, 263, 237.
- [40] Faulkner, L. R. *Electrochimica Acta* **1989**, 34, 1699.
- [41] Duffitt, G. L.; Pickup, P. G. *J. Chem. Soc. Faraday Trans.* **1992**, 88, 1417.

- [42] Deronzier, A.; Moutet, J.-C. *Coord. Chem. Rev.* **1996**, *147*, 339.
- [43] Ochmanska, J.; Pickup, P. G. *J. Electroanal. Chem.* **1989**, *271*, 83.
- [44] Cameron, C. G.; Pickup, P. G. *J. Chem. Soc. Chem. Commun.* **1997**, 303.
- [45] Cameron, C. G.; Pickup, P. G. *J. Am. Chem. Soc.* **1999**, *121*, 7710.
- [46] Cameron, C. G.; Pickup, P. G. *J. Am. Chem. Soc.* **1999**, *121*, 11773.
- [47] Maclean, B. J.; Pickup, P. G. *J. Chem. Soc. Chem. Commun.* **1999**, 2471.
- [48] Pickup, P. G. *J. Mater. Chem.* **1999**, *9*, 1641.
- [49] Kingsborough, R.; Swager, T. *Prog. Inorg. Chem.* **1999**, *48*, 123.
- [50] Rulkens, R.; Lough, A. J.; Manners, I.; Lovelace, S. R.; Grant, C.; Geiger, W. E. *J. Am. Chem. Soc.* **1996**, *118*, 12683.
- [51] Foucher, D. A.; Honeyman, C. H.; Nelson, J. M.; Tang, B. Z.; Manners, I. *Angew. Chem. Intl. Ed. Eng.* **1993**, *32*, 1709.
- [52] Kingsborough, R. P.; Swager, T. M. *Adv. Mater.* **1998**, *10*, 1100.
- [53] Reddinger, J. L.; Reynolds, J. R. *Macromol.* **1997**, *30*, 673.
- [54] Reddinger, J. L.; Reynolds, J. R. *Synth. Met.* **1997**, *84*, 225.
- [55] Rasmussen, S. C.; Thompson, D. W.; Singh, V.; Petersen, J. D. *Inorg. Chem.* **1996**, *35*, 3449.
- [56] Astruc, D. *Electron Transfer and Radical Processes in Transition-Metal Chemistry*; VCH: New York, 1995.
- [57] Richardson, D. E.; Taube, H. *Inorg. Chem.* **1981**, *20*, 1278.
- [58] Prassides, K., Ed.; *Mixed Valency Systems: Applications in Chemistry, Physics, and Biology*; Dordrecht: , 1991.
- [59] Kaim, W.; Kasack, V. *Inorg. Chem.* **1990**, *29*, 4696.
- [60] Haga, M.-A.; Ali, M. M.; Koeski, S.; Fujimoto, K.; Yoshimura, A.; Nozaki, K.; Ohno, T.; Nakajima, K.; Stufkens, D. J. *Inorg. Chem.* **1996**, *35*, 3335.
- [61] Haga, M.-A.; Ali, M. M.; Koseki, S.; Yoshimura, A.; Nozaki, K.; Ohno, T. *Inorg. Chim. Acta* **1994**, *226*, 17.
- [62] Haga, M.-A.; Ano, T.-A.; Kano, K.; Yamabe, S. *Inorg. Chem.* **1991**, *30*, 3843.
- [63] Ohno, T.; Nozaki, K.; Haga, M.-A. *Inorg. Chem.* **1992**, *31*, 4256.
- [64] Haga, M.-A.; Matsumura-Inoue, T.; Yamabe, S. *Inorg. Chem.* **1987**, *26*, 4148.

- [65] Wolf, M. O.; Wrighton, M. S. *Chem. Mater.* **1994**, *6*, 1526.
- [66] Tolman, C. A. *Chem. Rev.* **1977**, *77*, 313.
- [67] Tanaka, S.; Kaeriyama, K.; Hiraide, T. *Makromol. Chem., Rapid Commun.* **1988**, *9*, 743.
- [68] Bolognesi, A.; Catellani, M.; Destri, S.; Porzio, W. *Synth. Met.* **1987**, *18*, 129.
- [69] Catellani, M.; Destri, S.; Porzio, W.; Thémans, B.; Brédas, J. L. *Synth. Met.* **1988**, *26*, 259.
- [70] Lorkovic, I.; Wrighton, M. S.; Davis, W. M. *J. Am. Chem. Soc.* **1994**, *114*, 6220.
- [71] Zhu, S. S.; Swager, T. M. *Adv. Mater.* **1996**, *8*, 497.
- [72] Zhu, S. S.; Kingsborough, R. P.; Swager, T. M. *J. Mater. Chem.* **1999**, *9*, 2123.
- [73] Zhu, S. S.; Carroll, P. J.; Swager, T. M. *J. Am. Chem. Soc.* **1996**, *118*, 8713.
- [74] Zhu, S. S.; Swager, T. M. *J. Am. Chem. Soc.* **1997**, *119*, 12568.
- [75] Yamamoto, T.; Maruyama, T.; Zhou, Z.; Ito, T.; Fakuda, T.; Yoneda, T.; Begum, F.; Ikeda, T.; Sasaki, S.; Takezoe, H.; Fukuda, A.; Kubota, K. *J. Am. Chem. Soc.* **1994**, *116*, 4832.
- [76] Zotti, G.; Schiavon, G.; Zecchin, S. *Synth. Met.* **1995**, *72*, 275.
- [77] Chidsey, C. E. D.; Murray, R. W. *J. Phys. Chem.* **1986**, *90*, 1479.
- [78] Kern, J.-M.; Sauvage, J.-P.; Bidan, G.; Billon, M.; Divisa-Blohorn, B. *Adv. Mater.* **1996**, *8*, 580.
- [79] Vidal, P. L.; Billon, M.; Divisa-Blohorn, B.; Bidan, G.; Kern, J. M.; Sauvage, J. P. *J. Chem. Soc. Chem. Commun.* **1998**, 629.
- [80] Swager, T. M. *Acc. Chem. Res.* **1998**, *31*, 201.
- [81] Ley, K. D.; Whittle, C. E.; Bartberger, M. D.; Schanze, K. S. *J. Am. Chem. Soc.* **1997**, *119*, 3423.
- [82] Ley, K. D.; Schanze, K. S. *Coord. Chem. Rev.* **1998**, *171*, 287.
- [83] Peng, Z.; Yu, L. *J. Am. Chem. Soc.* **1996**, *118*, 3777.
- [84] Balzani, V.; Scandola, F. *Supramolecular Photochemistry*; Ellis Horwood: New York, 1991.
- [85] Juris, A.; Balzani, V.; Barigelletti, F.; Campagna, S.; Belser, P.; von Zelewsky, A. *Coord. Chem. Rev.* **1988**, *84*, 85.
- [86] Wang, Q.; Wang, L.; Yu, L. *J. Am. Chem. Soc.* **1998**, *120*, 12860.

- [87] Yamamoto, T.; Toned, Y.; Maruyama, T. *J. Chem. Soc. Chem. Commun.* **1992**, 1652.
- [88] Maruyama, T.; Yamamoto, T. *Inorg. Chim. Acta* **1995**, 238, 9.
- [89] Maruyama, T.; Yamamoto, T. *J. Phys. Chem. B* **1997**, 101, 3806.
- [90] Wright, M. E. *Macromol.* **1989**, 22, 3256.
- [91] Nishihara, H.; Funaki, H.; Shimura, T.; Aramaki, K. *Synth. Met.* **1993**, 55-57, 942.
- [92] Untitled software written by P. G. Pickup.
- [93] Sullivan, B. P.; Salmon, D. J.; Meyer, T. J. *Inorg. Chem.* **1978**, 17, 3334.
- [94] Lay, P. A.; Sargeson, A. M.; Taube, H. *Inorg. Synth.* **1986**, 24, 291.
- [95] Sullivan, B. P.; Calvert, J. M.; Meyer, T. J. *Inorg. Chem.* **1980**, 19, 1404.
- [96] Gronowitz, S., Ed.; *Thiophene and Its Derivatives*; volume 44-2 of *Heterocyclic Compounds* Wiley: New York, 1985.
- [97] Sharanina, L. G.; Baranov, S. N. *Chem. Heterocycl. Compd. (English translation)* **1974**, 10, 171.
- [98] Lancelot, J. C.; Maume, D.; Robba, M. J. *Heterocycl. Chem.* **1980**, 17, 625.
- [99] Aldrich Catalogue, 1994-1995 edn.
- [100] Ray, M.; Mukherjee, R.; Richardson, J. F.; Mashuta, M. S.; Buchanan, R. M. *J. Chem. Soc. Dalton Trans.* **1994**, 965.
- [101] Tourillon, G. Polythiophene and its Derivatives. In *Handbook of Conducting Polymers*, Vol. 1; Skotheim, T. A., Ed.; Marcel Dekker: New York, 1986.
- [102] Tour, J. M. *Chem. Rev.* **1996**, 96, 537.
- [103] Higgins, S. J. *Chem. Soc. Rev.* **1997**, 26, 247.
- [104] Davis, H. A. "The Synthesis of Precursors to Conjugated Polymers". Master's thesis, Memorial University of Newfoundland, 1998.
- [105] Huang, H. "Studies on the Electrochemistry and Applications of Conducting Polymers", Master's thesis, Memorial University of Newfoundland, 1998.
- [106] Berlin, A.; Brenna, E.; Pagani, G. A.; Sanniccolo, F.; Zotti, G.; Schiavon, G. *Synth. Met.* **1992**, 51, 287.
- [107] Brooks, N. W.; Rose, R. A.; Ward, I.; Clements, J. *Polymer* **1993**, 34, 4038.
- [108] Varma, I. K.; Veena, J. *J. Polym. Sci., Polym. Chem. Ed.* **1976**, 14, 973.
- [109] Socrates, G. *Infrared Characteristic Group Frequencies*; John Wiley: Chichester, 1980.

- [110] Gupta, R. R. *Physical Methods in Heterocyclic Chemistry*; General Heterocyclic Chemistry Series John Wiley: New York, 1984.
- [111] Jenekhe, S. A.; Johnson, P. O.; Agrawal, A. K. *Polym. Mater.: Sci. Eng.* **1989**, 60, 404.
- [112] Yang, C.-J.; Jenekhe, S. A. *Macromol.* **1995**, 28, 1180.
- [113] Lambert, J. B.; Shurvell, H. F.; Lightner, D.; Cooks, R. G. *Introduction to Organic Spectroscopy*; Macmillan: New York, 1987.
- [114] Tsai, E. W.; Basak, S.; Ruiz, J. P.; Reynolds, J. R.; Rajeshwar, K. *J. Electrochem. Soc.* **1989**, 136, 3683.
- [115] Sygula, A. *J. Chem. Res., Synop.* **1989**, 2, 56.
- [116] Schlegel, H. B.; Grund, P.; Fluder, E. M. *J. Am. Chem. Soc.* **1982**, 104, 5347.
- [117] Cameron, C. G.; Poirier, R. A. Unpublished data.
- [118] Frisch, M. J. *et al.* Gaussian 94, Revision B.3, Gaussian Inc., Pittsburgh PA, 1995.
- [119] Hehre, W. J.; Radom, L.; v. R. Schleyer, P.; Pople, J. A. *Ab Initio Molecular Orbital Theory*; John Wiley & Sons: New York, 1985.
- [120] Jenkins, I. H.; Salzner, U.; Pickup, P. G. *Chem. Mater.* **1996**, 8, 2444.
- [121] Dietz, K. H.; Beck, F. *J. Appl. Electrochem.* **1985**, 15, 159.
- [122] Novak, P.; Rasch, P.; Vielstich, W. *J. Electrochem. Soc.* **1991**, 138, 3300.
- [123] Seddon, E. A.; Seddon, K. R. *The Chemistry of Ruthenium*; Elsevier: Amsterdam, 1984.
- [124] Jestin, I.; Frere, P.; Mercier, N.; Levillain, E.; Stievenard, D.; Roncali, J. *J. Am. Chem. Soc.* **1998**, 120, 8150.
- [125] Fergusson, J. E.; Harris, G. M. *J. Chem. Soc (A)* **1966**, 1293.
- [126] McDevitt, M. R.; Ru, Y.; Addison, A. W. *Trans. Met. Chem.* **1993**, 18, 197.
- [127] Hage, R.; Lempers, H. E. B.; Haasnoot, J. G.; Reedijk, J.; Weldon, F. M.; Vos, J. G. *Inorg. Chem.* **1997**, 36, 3140.
- [128] Bard, A. J.; Faulkner, L. K. *Electrochemical Methods: Fundamentals and Applications*; Wiley: New York, 1980.
- [129] Carter, F. L. *Molecular Electronic Devices*; Marcel Dekker: New York, 1982.
- [130] Mabrouk, P. A.; Wrighton, M. S. *Inorg. Chem.* **1986**, 25, 526.
- [131] Callahan, R. W.; Keene, F. R.; Meyer, T. J.; Salmon, D. J. *J. Am. Chem. Soc.* **1977**, 99, 1064.

- [132] Creutz, C.; Taube, H. *J. Am. Chem. Soc.* **1969**, *91*, 3988.
- [133] Zotti, G.; Zecchin, S.; Schiavon, G.; Berlin, A.; Pagani, G.; Canavesi, A.; Casalbore-Miceli, G. *Synth. Met.* **1996**, *78*, 51.
- [134] Yoshida, Y.; Hashimoto, H.; Yoneda, S. *J. Chem. Soc. Chem. Commun.* **1971**, 1344.
- [135] Rillema, D. P.; Jones, D. S.; Levy, H. A. *J. Chem. Soc., Chem. Commun.* **1979**, 849.
- [136] Pickup, P. G.; Kutner, W.; Leidner, C. R.; Murray, R. W. *J. Am. Chem. Soc.* **1984**, *106*, 1991.
- [137] Kepley, L. J.; Bard, A. J. *J. Electrochem. Soc.* **1995**, *142*, 4129.
- [138] Schroeder, A. H.; Kaufman, F. B. *J. Electroanal. Chem.* **1980**, *113*, 209.
- [139] Lewis, T. J.; White, H. S.; Wrighton, M. S. *J. Am. Chem. Soc.* **1984**, *106*, 6947.
- [140] Shigehara, K.; Oyama, N.; Anson, F. C. *J. Am. Chem. Soc.* **1981**, *103*, 2552.
- [141] Anson, F. C.; Ohsaka, T.; Savéant, J. M. *J. Phys. Chem.* **1983**, *87*, 640.
- [142] Ikeda, T.; Leidner, C.; Murray, R. W. *J. Electroanal. Chem.* **1982**, *138*, 343.
- [143] Schilt, A. *Inorg. Synth.* **1970**, *12*, 247.
- [144] Ikeda, T.; Schmehl, R.; Denisevich, P.; Murray, R. W. *J. Am. Chem. Soc.* **1982**, *104*, 2683.
- [145] Pickup, P.; Murray, R. W. *J. Am. Chem. Soc.* **1984**, *105*, 4510.
- [146] Anderson, L. B.; Reilly, C. N. *J. Electroanal. Chem.* **1965**, *10*, 295.
- [147] Pearce, P. J.; Bard, A. J. *J. Electroanal. Chem.* **1980**, *114*, 89.
- [148] Brown, A. P.; Anson, F. C. *Anal. Chem.* **1977**, *49*, 1589.
- [149] Chidsey, C. E. D.; Murray, R. W. *J. Phys. Chem.* **1986**, *90*, 1479.
- [150] Bull, R. A.; Fan, F.-R. F.; Bard, A. J. *J. Electrochem. Soc.* **1982**, *129*, 1009.
- [151] Albery, W. J.; Mount, A. R. Transmission Lines for Conducting Polymers. In *Electroactive Polymer Electrochemistry, Part 1*; Plenum Press: New York, 1994.
- [152] Albery, W. J.; Elliot, C. M.; Mount, A. R. *J. Electroanal. Chem.* **1990**, *288*, 15.
- [153] Mathias, M. F.; Haas, O. *J. Phys. Chem.* **1992**, *96*, 3174.
- [154] Rubinstein, I.; Rishpon, J.; Gottesfeld, S. *J. Electrochem. Soc.* **1986**, *133*, 729.

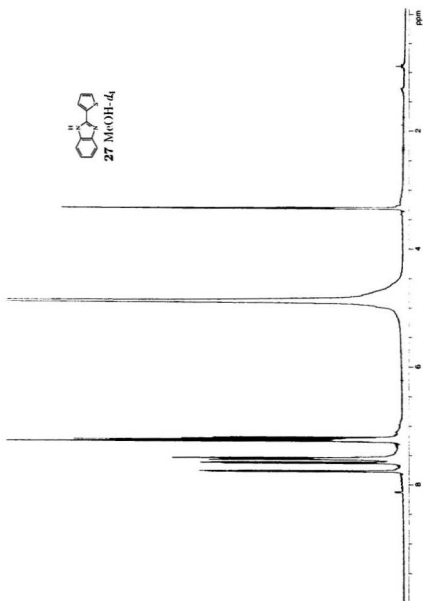
- [155] Láng, G.; Inzelt, G. *Electrochem. Acta* **1991**, *36*, 847.
- [156] Lefebvre, M. C.; Martin, R. B.; Pickup, P. G. *Electrochem. Solid State Lett.* **1999**, *2*, 6.
- [157] Qi, Z.; Lefebvre, M. C.; Pickup, P. G. *J. Electroanal. Chem.* **1998**, *459*, 9.
- [158] Ochmanska, J.; Pickup, P. G. *J. Electroanal. Chem.* **1991**, *297*, 197.
- [159] Denisevich, P.; Abruña, H. D.; Leidner, C. R.; Meyer, T. J.; Murray, R. W. *Inorg. Chem.* **1982**, *21*, 2153.
- [160] Oyama, N.; Ohsaka, T. Voltammetric Diagnosis of Charge Transport on Polymer Coated Electrodes. In *Molecular Design of Electrode Surfaces*. Vol. 22; Murray, R. W., Ed.; Wiley: New York, 1992.
- [161] Marcus, R. A.; Sutin, N. *Biochim. Biophys. Acta* **1985**, *811*, 265.
- [162] Hush, N. S. *Prog. Inorg. Chem.* **1967**, *8*, 391.
- [163] Creutz, C. *Prog. Inorg. Chem.* **1983**, *30*, 1.
- [164] Taube, H. *Angew. Chem. Intl. Ed. Eng.* **1984**, *23*, 329 (Nobel Lecture).
- [165] Robin, M. B.; Day, P. *Adv. Inorg. Chem. Radiochem.* **1967**, *10*, 247.
- [166] Saji, T. J.; Aiyagui, S. *J. Electroanal. Chem.* **1975**, *63*, 31.
- [167] Saji, T. J.; Aiyagui, S. *J. Electroanal. Chem.* **1975**, *63*, 401.
- [168] Meyer, T. J.; Taube, H. In *Comprehensive Coordination Chemistry*, Vol. 1; Wilkinson, G.; Guilard, R.; McLafferty, J. A., Eds.; Pergamon Press: Oxford, 1987.
- [169] Sutin, N. *Acc. Chem. Res.* **1982**, *15*, 275.

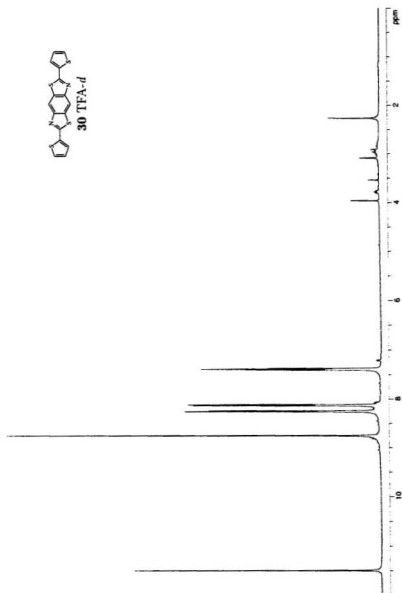
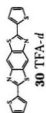
APPENDIX A

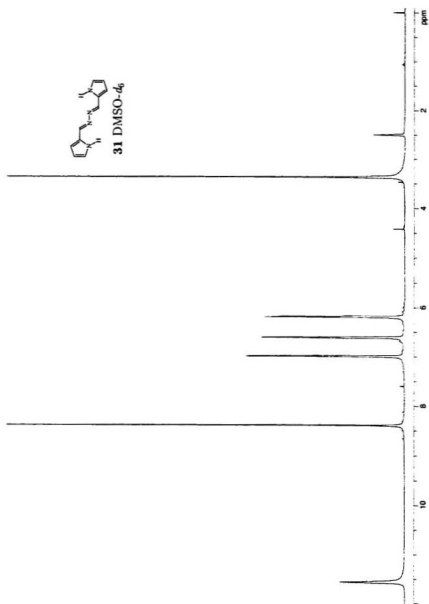
SPECTRA

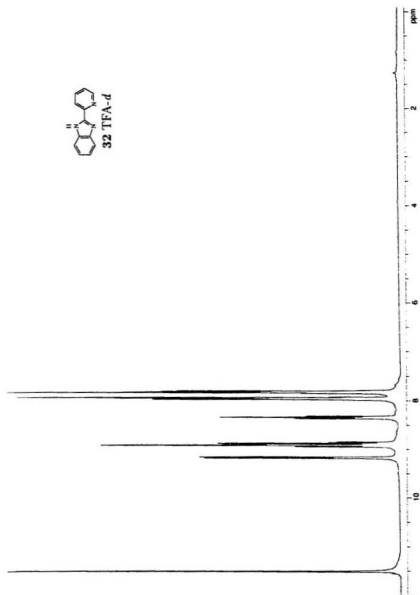
A.1 ^1H NMR Spectra

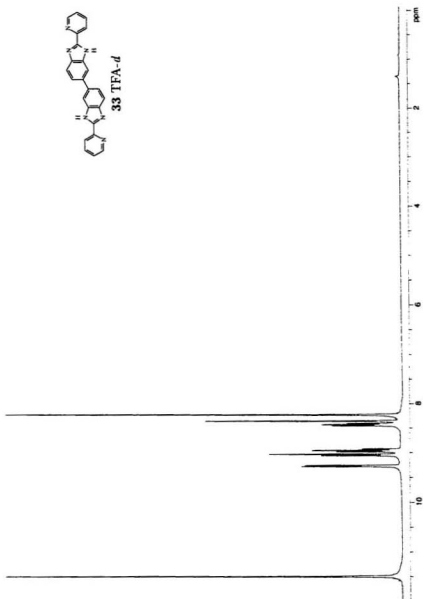
A.1.1 Models and Monomers

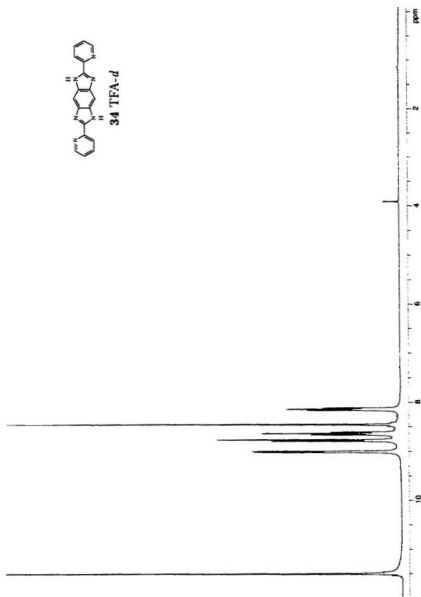


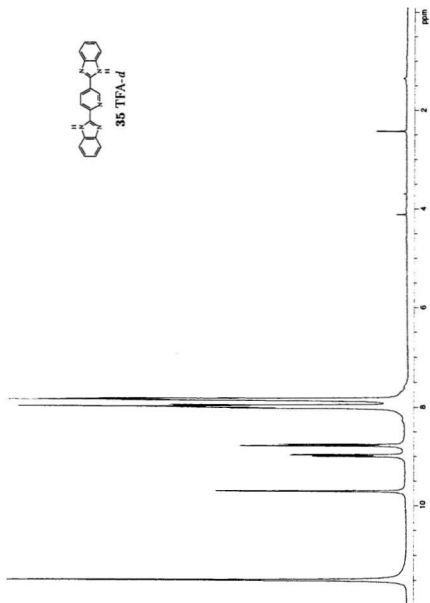


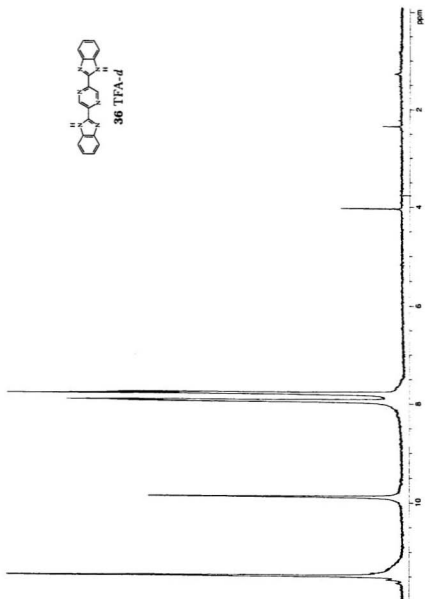


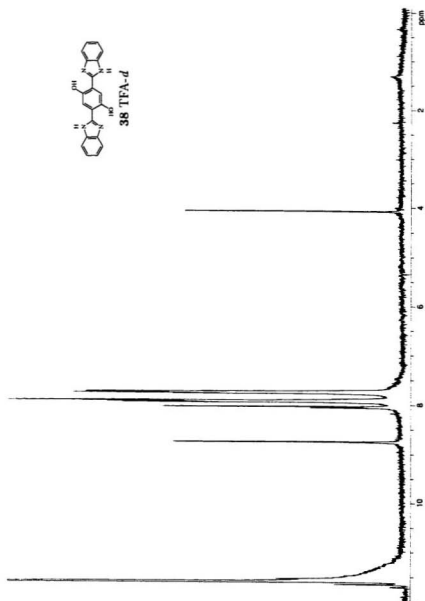


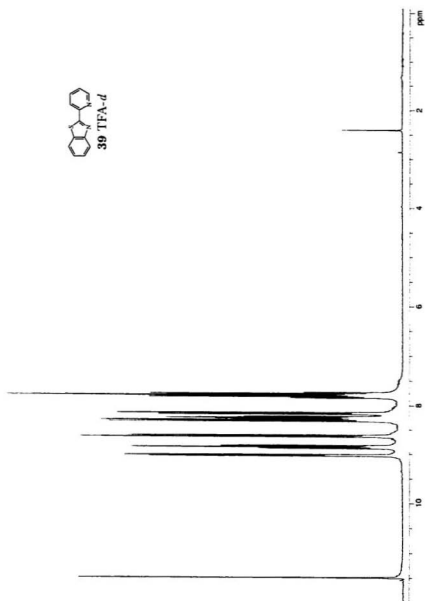


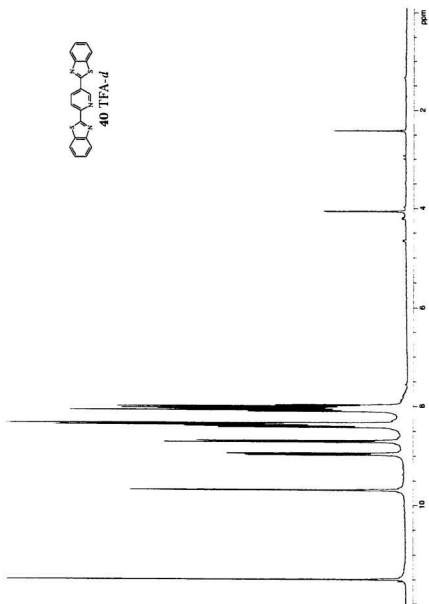


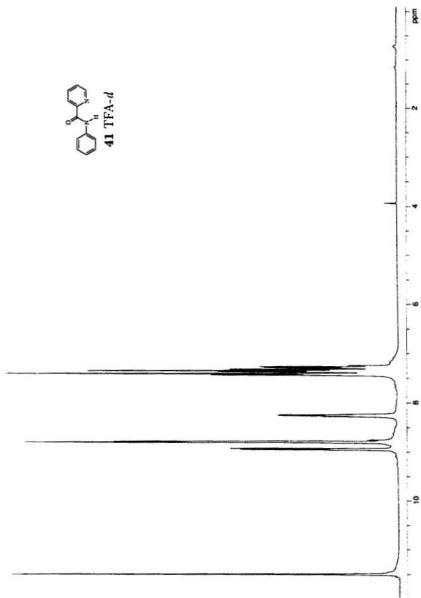




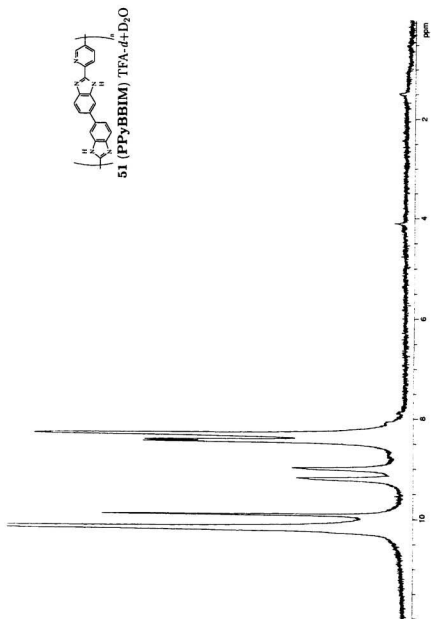


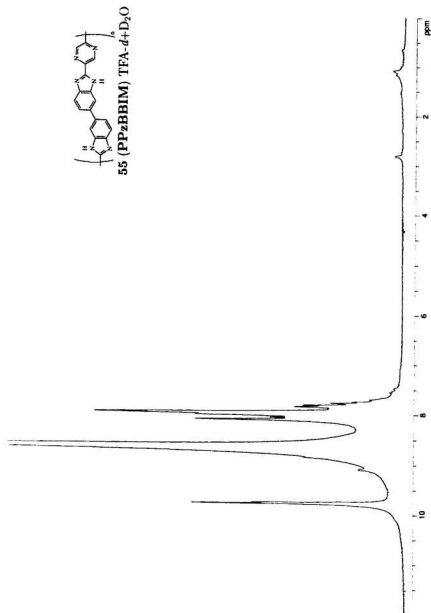






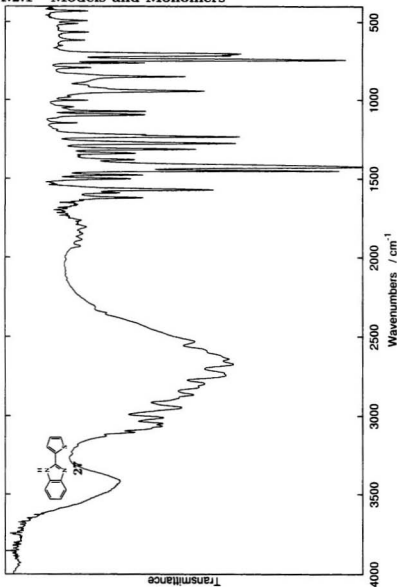
A.1.1.2 Polymers

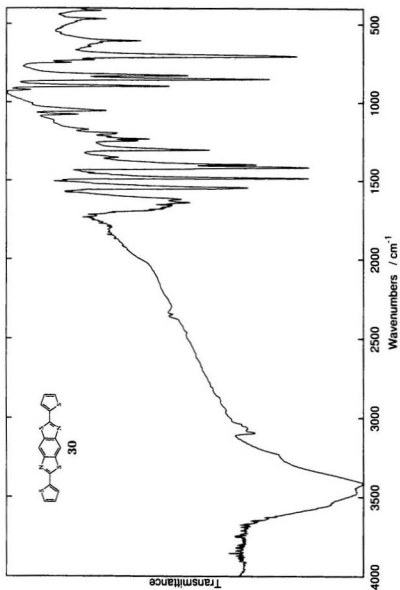


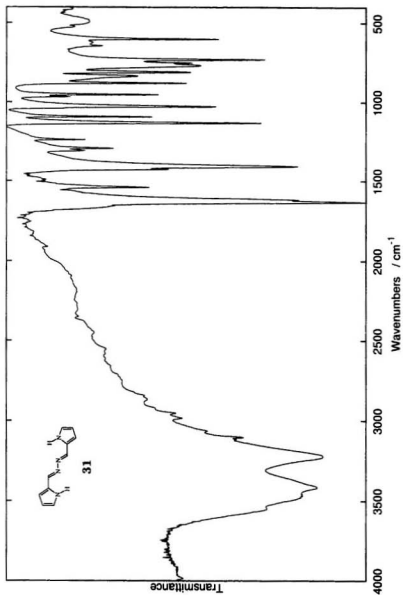


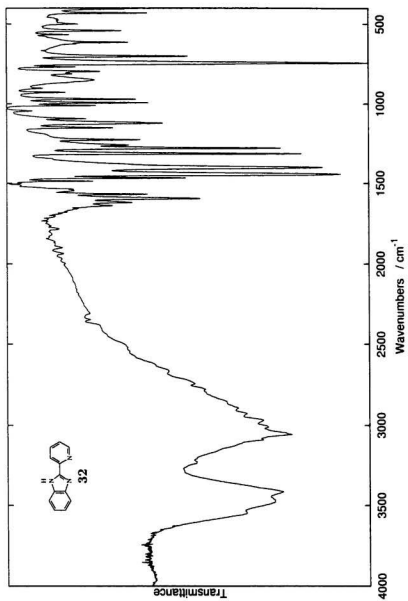
A.2 Infrared Spectra

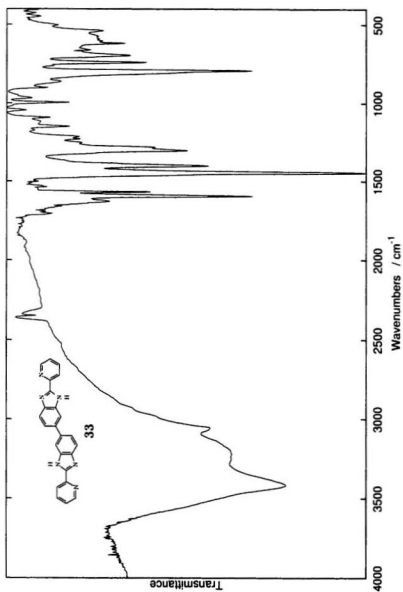
A.2.1 Models and Monomers

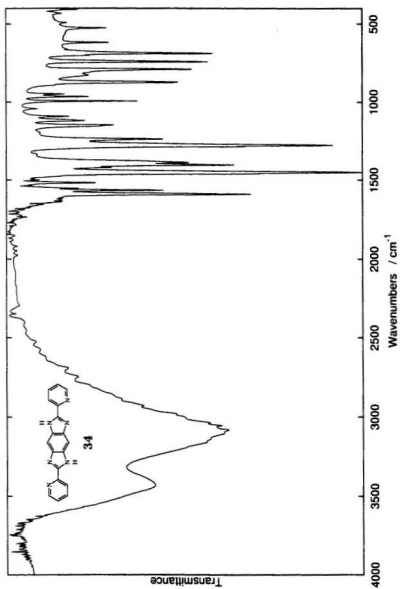


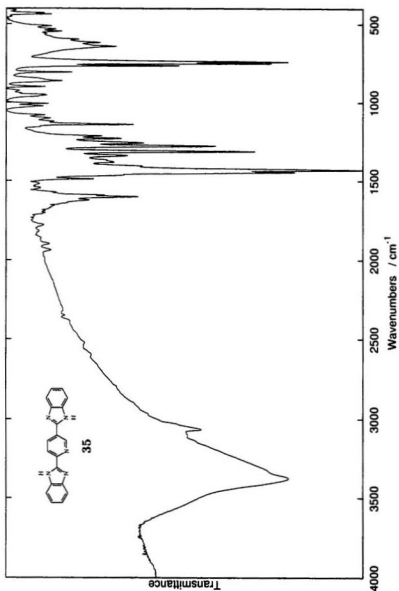


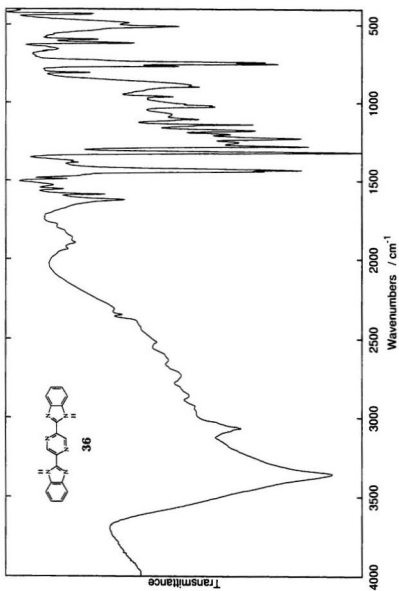


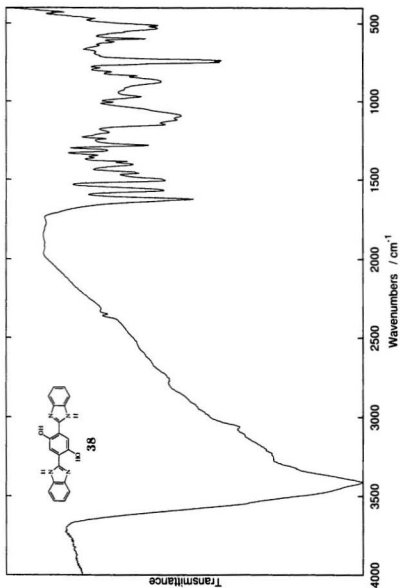


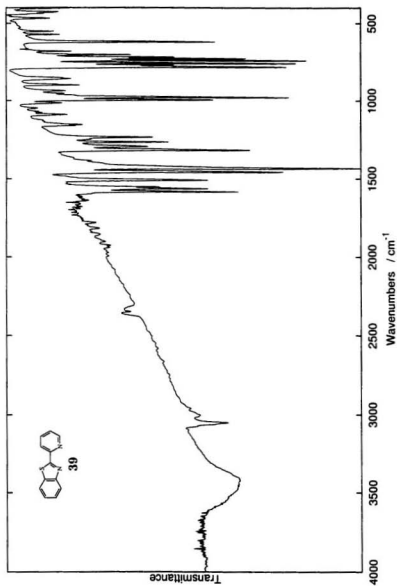


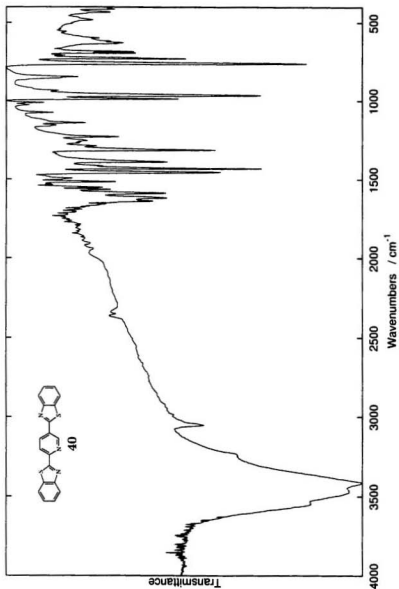


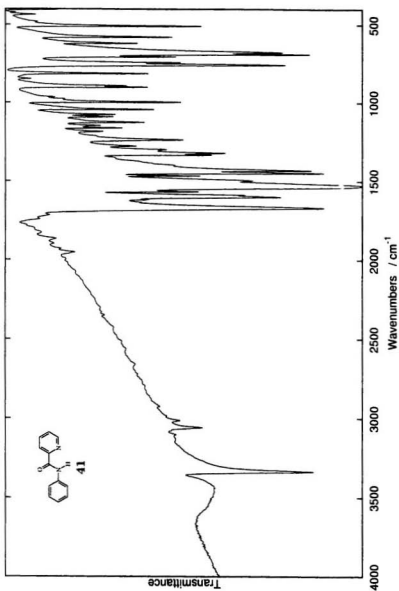












A.2.2 Polymers

